Disorder in Ca^{2+} Release Unit Locations Confers Robustness but Cuts Flexibility of Heart Pacemaking

Anna V. Maltsev[1]*, Michael D. Stern[2], Victor A. Maltsev[2]**,

[1]*School of Mathematics, Queen Mary University of London, London, United Kingdom*

[2]*Laboratory of Cardiovascular Science, Intramural Research Program, National Institute on Aging, NIH, 251 Bayview Blvd, Baltimore, Maryland 21224*

Running title: Ca^{2+} release propagation controls heart pacemaking

***Corresponding author:**

Anna V. Maltsev

Email: a.maltsev@qmul.ac.uk

Telephone: +44 (0)20 7882 2969

****Secondary Corresponding Author:**

Victor A. Maltsev

Email: maltsevvi@mail.nih.gov

Telephone: 1-410-454-8459

Abstract

Excitation-contraction coupling kinetics are dictated by the action potential rate of sinoatrial-nodal cells. These cells generate local Ca releases (LCRs) that activate Na/Ca exchanger current, which accelerates diastolic depolarization and determines the pace. LCRs are generated by clusters of ryanodine receptors, Ca release units (CRUs), residing in the sarcoplasmic reticulum. While CRU distribution exhibits substantial heterogeneity, its functional importance remains unknown. Using numerical modeling, here we showed that with a square lattice distribution of CRUs, Ca-induced-Ca-release propagation during diastolic depolarization is insufficient for pacemaking within a broad range of realistic I_{CaL} densities. Allowing each CRU to deviate randomly from its lattice position allows sparks to propagate, as observed experimentally. As disorder increases, the CRU distribution exhibits larger empty spaces and simultaneously CRU clusters, as in Poisson clumping. Propagating within the clusters, Ca release becomes synchronized, increasing action potential rate and reviving pacemaker function of dormant/non-firing cells. However, cells with fully disordered CRU positions could not reach low firing rates and their β-adrenergic-receptor stimulation effect was substantially decreased. Inclusion of $Ca_v1.3$, a low-voltage activation L-type Ca channel isoform into I_{CaL} strongly increases recruitment of CRUs to fire during diastolic depolarization, increasing robustness of pacemaking and complementing effects of CRU distribution. Thus, order/disorder in CRU locations along with $Ca_v1.3$ expression regulates pacemaker function via synchronization of CRU firing. Excessive CRU disorder and/or overexpression of $Ca_v1.3$ boost pacemaker function in the basal state, but limit the rate range, which may contribute to heart rate range decline with age and in disease.

Summary

The present numerical modeling study shows that disorder in locations of Ca release units in cardiac pacemaker cells has substantial functional impact by creating release clusters, similar to Poisson clumping, and opportunity of Ca release to propagate within the clusters.

Keywords: Ryanodine Receptor, Calcium, Sarcoplasmic Reticulum, Sinoatrial Node.

Introduction

Each excitation-contraction coupling cycle in the heart begins with the generation of rhythmic excitation in the sinoatrial node (SAN). To satisfy a given blood supply demand, cardiac muscle performance, defined by its state of contractile apparatus, Ca cycling proteins, and cell excitability must be in balance with the rate and rhythm of the excitation impulses generated by the SAN. Thus, the cardiac pacemaker function is a vital part of the excitation-contraction coupling that "sets the stage" for timely interactions for all further downstream mechanisms.

In turn, the generation of normal rhythmic cardiac impulses is executed via timely interactions within and among SAN pacemaker cells that involve coupled signaling of both cell membrane ion channels and Ca cycling, dubbed a coupled-clock system (Maltsev and Lakatta, 2009; Lakatta et al., 2010). A key element of the system is the sarcoplasmic reticulum (SR) that rhythmically generates diastolic local Ca releases (LCRs) via Ca release channels, ryanodine receptors (RyRs). The LCRs contribute to SAN cell pacemaker function via activation of Na/Ca exchanger (NCX) current (I_{NCX}) that accelerates the diastolic depolarization (Huser et al., 2000; Bogdanov et al., 2001; Lakatta et al., 2010). Initially the role of Ca release in cardiac pacemaker

function has been numerically studied in so-called “common pool” models (Kurata et al., 2002; Himeno et al., 2008; Maltsev and Lakatta, 2009; Imtiaz et al., 2010; Severi et al., 2012), in which spatial Ca dynamics was neglected and cell Ca release was approximated by a single variable (i.e. providing non-spatial, whole-cell description).

While such traditional simplified approach has yielded substantial progress in our understanding of Ca release role in pacemaker function (including modern theories of coupled-clock function (Maltsev and Lakatta, 2009) and ignition (Lyashkov et al., 2018)), it has fundamental limitations, and further progress requires a new type of modeling that would take into account spatial interactions (Maltsev et al., 2014). A general issue is that we still do not have a clear quantitative understanding of how the Ca clock and the coupled clock system emerge from the scale of molecules (such as RyRs) towards the whole cell function (Weiss and Qu, 2020). Thus, how spatially distributed and whole-cell signaling events that coordinate cell function emerge from stochastic openings of individual release channels remains an unresolved fundamental problem despite extensive investigation.

A concrete issue with common pool models is that they operate with Ca signals in sub-μM range, that is at least two orders of magnitude lower than in the local vicinity of the RyR release clusters, i.e. inside Ca sparks and diastolic LCRs (up to tens and even hundreds of μM (Stern et al., 2013; Stern et al., 2014)). The molecules involved in pacemaker function (ion channels, exchangers, pumps, and Ca-sensitive enzymes), however, operate via the high local Ca concentrations rather than a whole-cell average. Common pool models thus are analogous to a mean-field theory approach in physics, which usually does recover faithfully qualitative information about system behavior, but fails to zone in on the critical parameter values.

While the membrane clock operates as a limit cycle oscillator (Kurata et al., 2012), the Ca-clock seems to operate by completely different mechanisms based on phase transitions (Maltsev et al., 2011) or criticality (Nivala et al., 2012; Weiss and Qu, 2020). RyRs are organized and operate in clusters of 10-150 channels (Greiser et al., 2020), known as Ca release units (CRUs) in all cardiac cells, including SAN cells (Maltsev et al., 2011; Stern et al., 2014). Ca release in ventricular myocytes occurs mainly via Ca sparks (defined as a single CRU Ca release) tightly controlled by L-type Ca channel (LCC) openings (local control theory (Stern et al., 1997)) , whereas LCRs in SAN cells consist of multiple sparks that emerge spontaneously via self-organization by means of positive feedback provided by Ca-induced Ca release (CICR). The synchronized CRU activation leads to oscillatory, phase-like transitions in SAN cells (Maltsev et al., 2011) that generate a net diastolic LCR signal that ultimately interacts with NCX and LCCs (Maltsev et al., 2013; Lyashkov et al., 2018) to ignite pacemaker action potentials (APs), which comprises the ignition theory of APs (Lyashkov et al., 2018). The probability that a Ca spark can "jump" in this way to activate its neighbor and form a propagating multi-spark LCR instead of remaining an isolated event depends on various parameters, including the amplitude of the spark (sometimes called I_{spark} (Zhou et al., 2009; Maltsev et al., 2011)) and its nearest neighbor distance (Stern et al., 2014). The difficult and fascinating phenomenon that occurs in this system is that the area affected by propagation of an LCR (similar to connected component in percolation theory) is discontinuous in the probability of the Ca spark "jump." This discontinuity is a phase-like transition first demonstrated in (Maltsev et al., 2011), and the exact parameter values at which it occurs is known as criticality. Thus, to understand the intrinsic mechanisms of SAN cell operation, it is important to quantitatively predict critical parameter values at which the system changes its operational paradigm from sparks to LCRs.

Initially, the LCRs were numerically studied with CRUs located in a perfect rectangular lattice (Maltsev et al., 2011; Maltsev et al., 2013). These studies showed that the ability of an LCR to propagate regulates the size and the impact of the LCRs on the diastolic depolarization. However, RyR immunofluorescence exhibited notable disorder in the CRU distribution (Stern et al., 2014; Maltsev et al., 2016) and a more recent numerical model (Stern et al., 2014) was developed with two fixed sizes of CRUs. The larger CRUs were located in a rectangular lattice that lacked release propagation until smaller clusters were introduced in the CRU network providing bridges for release propagation among the larger CRUs. While this CRU geometry is closer to realistic distribution and provided functionality to the SAN cell model, the total number of CRUs was not controlled, and thus whether or not disorder in the CRU distribution per se is capable of impacting SAN cell function has not been examined and represents the specific aim of the present study.

Here we approach the problem via numerical model simulations of SAN cell function with the same number of identical CRUs, but different spatial CRU distributions. Specifically, we test how various degree of disorder (or noise) in CRU positions would influence SAN cell operation. We found that the least robust SAN cell function is achieved when CRU positions are distributed in the perfect rectangular lattice. As disorder in the CRU positions increases, nearest neighbor distances decrease, creating “shortcuts” for Ca release propagation resulting in AP firing rate increase and robust pacemaker function. The most robust function was achieved when CRUs were distributed independently uniformly randomly.

However, the robust function comes at the cost of the chronotropic reserve of the CRU-based mechanism: disorder-facilitated broad propagation of Ca release in the basal state recruits a major fraction of CRUs, leaving only a minor fraction of CRUs unrecruited. And vice versa, in

the case of square lattice CRU distribution with longer nearest-neighbor distances, a larger fraction of CRUs remains ready to fire and not recruited in the basal state (creating "the reserve"). This reserve becomes available to accelerate AP firing during β-adrenergic receptor (βAR) stimulation. Thus, order/disorder in spatial CRU distribution provides a novel subcellular mechanism of cardiac pacemaker regulation that a SAN cell may utilize to achieve a perfect balance between robustness and flexibility commensurate with its specific location and function within SAN tissue.

In addition to self-organization of CRU firing via propagating CICR, CRUs can be recruited to fire via direct activation of LCC. Studies in transgenic mice have demonstrated specific importance of the $Ca_v1.3$ LCC isoform for cardiac pacemaker function (Mesirca et al., 2015). While both $Ca_v1.2$ and $Ca_v1.3$ isoforms are colocalized with RyR clusters (i.e. CRUs) (Christel et al., 2012), $Ca_v1.3$ has a lower (more hyperpolarized) voltage activation threshold, thereby providing a larger contribution to diastolic depolarization by generating an inward current and by regulating RyR-dependent Ca release during SA node pacemaker activity (Torrente et al., 2016). Thus, the present study also tested possible importance of $Ca_v1.3$ for rabbit SAN function with respect to its interplay with CRU distribution.

Methods

Common pool models, such as of Kurata et al. (Kurata et al., 2002) or Maltsev-Lakatta (Maltsev and Lakatta, 2009), are on the cellular scale, lumping the contributions of all CRUs into one variable describing Ca release and one pool of junctional SR (JSR) with fixed total volume. On the other hand, a 3D model of SAN cell developed by Stern et al. (Stern et al., 2014) featuring interactions of individual RyRs provides too many fine details of intra-CRU Ca dynamics at a

much higher computational cost and which are not so important for understanding Ca dynamics at the level of CRU to CRU.

Thus, an adequate model for our study should deal with Ca release at the sub-micron level (as CRUs detected by confocal microscopy). We have previously developed such a model (sub-micron, CRU-resolved model) featuring a two-dimensional array of stochastic, diffusively coupled CRUs located under cell membrane (Maltsev et al., 2011), and then added the full electrophysiological membrane clock (Maltsev et al., 2013). While approximation of Ca release at the sub-micron level suits our study, here we performed a further major model update, including a model of Ca clocking and an upgrade to 3D (Fig. 1). The full details of the updated model are given in the Appendix, but here is a summary of important changes:

1) A major weakness of our old model was that it modeled the CRU as having a built-in "refractory period," when the CRU could not activate. Thus, it was not a mechanistic "coupled-clock" model because the refractory period of CRU firing Ca release (being the essence of the clock) was in fact an independent model parameter obtained as a direct read-off value from experimental data (Maltsev et al., 2011). After the refractory period, the CRU was placed into a "ready" state, meaning that it is allowed to open with a given dyadic cleft-Ca dependent probability per unit time. Here we modified the model to predict the timing of spark activation based on JSR Ca concentration using the present knowledge in this research area. A typical spark generated by our new model is shown in Fig. A1. CRUs are placed in the "ready" state when the JSR Ca reaches a certain threshold level of Ca as it refills during diastole via SERCA pumping and intra-SR diffusion. The threshold existence and precise value are suggested by experimental studies (Vinogradova et al., 2010), numerical model simulations via common pool models

184 (Maltsev and Lakatta, 2009; Imtiaz et al., 2010), RyR-based models (Stern et al., 2014), and by a
185 recent theoretical study based on Ising formalism (Veron et al., 2021).
186
187 2) In the previous model, CRU Ca release flux was fixed to certain I_{spark} value (another
188 independent model variable). In the new model it is proportional to difference in [Ca] inside and
189 outside the JSR.
190
191 3) In our prior model, the stochastic CRU firing generated a spark of a fixed duration that was
192 another independent model variable tuned to experimental data. In our new model Ca release of a
193 CRU is terminated when I_{spark} reaches a small value that is comparable with the release
194 amplitude of a single RyR at a given SR Ca level, in accord with the spark death mechanism via
195 disruption of inter-RyR CICR. This is in line with modern concepts of spark termination such as
196 induction decay (Laver et al., 2013), spark "death" (Stern et al., 2013) and Ising formalism
197 (Maltsev et al., 2017a). The basic idea of all three conceptions is that a Ca spark is generated and
198 kept alive by positive feedback of inter-RyR CICR, until the SR becomes sufficiently depleted
199 for RyR currents to wane and for inter-RyR CICR to be disrupted, culminating in Ca spark
200 termination.
201
202 4) The new model features a more realistic Ca distribution within the cell (Fig. 1). Our previous
203 model was a 2D model: CRUs resided in a square lattice under the cell surface with common
204 pools of SR and cytosol; local (spatially resolved) Ca concentrations were predicted by the
205 model only under cell membrane in 2D. The new model includes 3 layers of intracellular voxels.
206 Thus, it becomes a 3D model, making cytoplasmic Ca dynamics more realistic and precise. Its

structure is similar to that of Stern et al. model (Stern et al., 2014), but the number of voxel layers from cell surface to cell center is limited to three (for more computational efficiency): fine submembrane voxels, intermediate "ring" voxels, and larger cell core voxel. Importantly, the voxel layers are introduced only for computational efficiency and they do not have any physical barriers or gradients. The submembrane voxels (i.e. submembrane space) are not artificially separated from the rest of the cell. All intracellular voxels, including those of submembrane space, have the same characteristics of Ca diffusion and buffering.

5) We introduced JSR connected to free SR (FSR) via a diffusional resistance that determines the kinetics of JSR refilling with Ca. This is a key part of the Ca clock mechanism (Maltsev and Lakatta, 2009; Imtiaz et al., 2010; Vinogradova et al., 2010).

6) Ca in JSR is buffered by calsequestrin.

7) The CRUs in the prior model positioned as a square lattice. Here we added the capability to introduce various degree of disorder around the ideal square lattice positions of the CRUs so that the resulting distribution of nearest-neighbor distances would be spread and thus more closely reproduce the CRU network geometry reported in confocal microscopy studies (Stern et al., 2014).

8) I_{CaL} formulation was improved by including a contribution of $Ca_v1.3$ isoform to I_{CaL} in addition to the cardiac-specific isoform $Ca_v1.2$. Both $Ca_v1.2$ and $Ca_v1.3$ isoforms are localized in CRUs (Christel et al., 2012), but have different voltage activation thresholds (see Appendix).

Our simulations were initially performed with I_{CaL} comprised of cardiac-specific isoform $Ca_v1.2$. Then we investigated effects of inclusion of $Ca_v1.3$ isoform into I_{CaL} (two last sections of the Results).

Results

The basal AP firing rate increases as CRU distribution becomes disordered

First, we tested how SAN cell function changes if the same number of identical CRUs is distributed differently under cell membrane. We generated and tested cell models with 5 different types of spatial distributions of CRUs with gradually increasing disorder in the CRU positions. Left panels in Figure 2 show the cell cylinder surfaces "unwrapping" to squares with different simulated CRU distributions:

1) CRUs placed exactly at the nodes of a square lattice of 1.44 μm size.
2) CRUs slightly deviating from the “square lattice” positions, following Gaussian distribution with standard deviation, SD= 0.25 μm.
3) CRUs moderately deviating from “square lattice” positions, following Gaussian distribution with SD= 0.5 μm.
4) CRUs strongly deviating from the “square lattice” positions, following Gaussian distribution with SD=0.75 μm.
5) Uniformly independently random CRU positions excluding overlap.

As disorder in CRU position increased, the standard deviation of CRU nearest neighbor distance distribution increased, but the mean values decreased from 1.44 μm to 0.777 μm, respectively (Fig. 2, right panels). For a comparison, confocal microscopy measurements performed previously in 6 rabbit SAN cells reported average nearest distances between CRUs in each cell ranging from 0.71 to 0.89 μm (Stern et al., 2014), i.e. close to our simulated values. In all these CRU settings our numerical model simulations (with 100% $Ca_v1.2$ in I_{CaL}) generated rhythmic spontaneous AP firing. However, the rate of the spontaneous firing substantially increased as disorder degree increased and average AP cycle length (CL) shortened (Fig. 3, for specific values see Table 1, "Basal state" row). The effect of randomness was substantial: in the extreme case of uniformly random distribution the diastolic depolarization duration was shortened about in half (Fig. 4 A, red vs. black traces), and the CL reduced by >30%, accordingly. This effect is comparable or even exceeds the effect of βAR stimulation on CL reported in rabbit SAN cells (Vinogradova et al., 2002). The average CL exhibits a linear dependence vs. average nearest neighbor distance (R^2=0.96, inset to Fig. 3 A), indicating importance of CRU interactions with their nearest neighbors (i.e. CICR) in this phenomenon.

Disorder in CRU positions accelerates CRU recruitment and Ca release synchronization in diastole

Because our hypothesis was that spatial CRU distribution affects CICR among the CRUs, we examined the dynamics of CRU recruitment in our five RyR settings by monitoring N_{CRU}, i.e. the number of CRU firing at each moment of time during diastole. To compare dynamics of CRU recruitment during diastolic depolarization, we overlapped the traces of representative cycles for each CRU setting and synchronized them at the maximum diastolic potential (MDP) (Fig. 4 A,

B). We found that for all CRU settings, a major fraction of CRU pool became recruited to fire during diastolic depolarization, i.e. before the AP upstroke. However, uniform random CRU distribution resulted in a more synchronized and much faster recruitment of CRU firing compared to square lattice setting, with increasing degree of disorder yielding an increase of recruitment pace.

Electrophysiological consequences of accelerated CRU recruitment: role of I_{NCX} and I_{CaL}

As a result of faster CRU recruitment, the I_{NCX} and I_{CaL} were activated earlier in the cycle, accelerating diastolic depolarization and thereby shortening the CL (Fig. 4 C, D). In all scenarios I_{CaL} was activated concurrently with I_{NCX} or after a short delay (Fig. 5), indicating that the system operates via the coupled-clock paradigm (Maltsev and Lakatta, 2009) and in accord with ignition theory (Lyashkov et al., 2018). The short delay increased with the increasing disorder in CRU positions, indicating that enhanced CRU recruitment activates I_{NCX} at low voltages, below I_{CaL} activation (<-50 mV). To illustrate the diastolic CRU recruitment, we made representative screenshots of CRU firing for each CRU setting overlapped with instant local Ca distribution under the cell membrane at the membrane potential (V_m) of -45 mV that is close to the AP ignition onset and I_{CaL} activation threshold (Fig. 6). Mainly individual sparks were observed in the square lattice setting. In contrast, the uniform random setting showed propagating LCRs. The intermediate setting with various degrees of disorder exhibited intermediate recruitment. Different CRU firing patterns can also be seen in the respective movies of local Ca dynamics in subspace (Movies 1-5).

Disorder in CRU positions increases robustness of basal automaticity

SAN cells are very heterogeneous in their biophysical properties and their key ion current densities vary substantially, e.g. up to an order of magnitude for I_{CaL} (Honjo et al., 1996; Monfredi et al., 2017) (Fig.7, red circles). On the other hand, our simulations showed that the rate of spontaneous AP firing can be substantially reduced because of differences in spatial CRU distribution (Fig. 3). We then hypothesized that it is possible to find a range for realistic I_{CaL} densities at which spontaneous AP firing is impossible for the square lattice CRU distribution, but possible for uniformly random model. To match realistic I_{CaL} density values (in pA/pF) and our model parameter g_{CaL} (in nS/pF) determining maximum I_{CaL} conductance, we performed voltage-clamp simulations with the voltage step protocol similar to that in experimental studies (Honjo et al., 1996; Monfredi et al., 2017). To instantly attain steady-state activation and inactivation gating, we set respective gating variables *fL* and *dL* in the model to their steady-state values calculated at the holding potential of -45 mV. Thus, our basal state conductance 0.464 nS/pA in the model generated the maximum peak I_{CaL} current of 11.17 pA/pF shown by upper edge of the magenta band in Fig. 7 A that crosses the range of the experimentally measured I_{CaL} densities approximately in the middle. Please note that the graph in Fig. 7 A has a dual *y* axis scale, for I_{CaL} and g_{CaL} respectively, bridging experimental and simulated data.

Then we performed a wide range sensitivity analysis for g_{CaL} from its basal value of 0.464 nS/pF (100%) down to 0.2552 nS/pF (55%) that remained within the range of realistic I_{CaL} values (magenta band in Fig. 7 A). The analysis revealed a wide margin of g_{CaL} values (shown by red shade in Fig. 7 B) where the AP firing is impossible with square lattice distributions of CRUs (red circles), but possible with uniformly random CRU positions. All simulated traces of 16.5 s

duration are shown in Fig. A2 and an example of the result is shown in Fig. 7 C for g_{CaL} of 0.3248 nS/pF.

This analysis revealed another important aspect of SAN function with different CRU distributions: the model with the square lattice CRU distribution was capable of generating AP firing with relatively long CL of 536 ms on average (before it failed), whereas in uniformly random CRU model could reach only 438 ms. Thus, SAN cells can (in theory) harness their CRU distribution to safely reach low rates.

Subthreshold signaling

A newly discovered paradigm of pacemaker cell function is the ability of some SAN cells to reversibly switch to dormant (non-firing) state. It was found in isolated cells (Kim et al., 2018; Tsutsui et al., 2018; Tsutsui et al., 2021) and in SAN tissue (Bychkov et al., 2020; Fenske et al., 2020). Furthermore, non-firing cells in SAN tissue can generate subthreshold signals that may be important signaling events for generation of synchronized cardiac impulses (Bychkov et al., 2020). Thus, we hypothesized that CRU distribution is important not only for AP firing, but also for generation of subthreshold signals in dormant cells. One important factor in cell dormancy is a lower density of I_{CaL} (Tsutsui et al., 2021). Using the results of our sensitivity analysis, we chose a low g_{CaL} of 0.2552 nS/pF, at which AP firing is impossible in both uniformly random and square lattice models and compared subthreshold V_m signals in the non-firing cells in each case (Fig. 8 A). We found that subthreshold V_m oscillations in case of uniformly random distribution are much more powerful and occurred at a faster frequency than those in the square lattice model (Fig. 8 A inset, Movies 6 and 7) as evident from the overlapped power spectra of both V_m signals computed for the time period after AP failure (Fig. 8 B).

343

344 **Order in CRU position increases chronotropic reserve in fight-or-flight reflex**

345 Normal pacemaker cell function is not only robust, but also flexible, i.e. able to increase the AP
346 firing rate under stress (fight-or-flight reflex) or decrease it at rest. We tested if CRU distribution
347 plays a role in the flexibility of SAN cell function by examining responses of our model to βAR
348 stimulation. Our simulations showed that all five CRU settings from square lattice to uniform
349 random exhibit fight-or-flight reflex. The CL notably decreased in the presence of βAR
350 stimulation (red bars vs. blue bars in Fig. 9 A). All intervalograms are shown in Fig. A3, and
351 examples of βAR stimulation effect in extreme cases of CRU distributions are shown in Fig. 9 B.
352 The presence of disorder substantially decreased the stimulation effect, that is the CL shortening
353 decreased as disorder in CRU positions increased (both absolute and relative changes are given
354 in Table 1). Furthermore, the absolute decrease in the CL was linearly related (R^2=0.9931) to the
355 basal CL before βAR stimulation (Fig. 9 C) that is in accord with a recent experimental report
356 (Kim et al., 2021).

357 To get further insights into the effect of spatial disorder on βAR stimulation, we
358 simulated and compared the dynamics of N_{CRU} and I_{NCX} during a representative cycle for square
359 lattice and uniform models (Fig. 10). We found that in both cases the βAR stimulation effect,
360 linked to earlier and stronger recruitment of CRUs, translated to respective earlier and stronger
361 activation of I_{NCX}. However, this effect (i.e. the shift to earlier CRU recruitment) was stronger in
362 square lattice setting, indicating the presence of a larger "reserve" CRU pool ready to be
363 activated and synchronized via βAR stimulation.

364

365

Interplay of $Ca_v1.3$ and CRU distribution

Thus far, we reported our results about functional importance of CRU distribution with I_{CaL} approximated as a whole-cell I_{CaL} current generated by cardiac-specific isoform $Ca_v1.2$ (i.e. percentage of $Ca_v1.3$ was set to 0). In this section we report the results of our investigation of possible importance of $Ca_v1.3$ with respect to its interplay with CRU distribution. Because the contribution of $Ca_v1.3$ to the whole cell I_{CaL} is presently unknown in rabbit SAN cells, we performed a full-scale parameter sensitivity analysis by varying contribution of $Ca_v1.3$ from 0 to 100% with an interval of 10%. Our simulations with Cav1.3 in I_{CaL} revealed the following:

1) Substitution of $Ca_v1.3$ for $Ca_v1.2$ in the whole cell I_{CaL} substantially shortened CL for both square lattice and uniformly random distributions of CRUs (Fig. 11 A). However, the total CL shortening with full substitution of $Ca_v1.2$ by $Ca_v1.3$ (i.e. 0% vs. 100%) was smaller for the uniformly random CRUs, i.e. 25.9% vs. 39.8% for square lattice CRUs (blue arrow vs. orange arrow in Fig. 11 A).

2) At any specific percentage of $Ca_v1.3$, the average CL was always notably shorter for the uniformly random CRU distribution. Thus the CRU randomness caused an additional CL reduction on the top of CL reduction due to $Ca_v1.3$. This additional effect was substantially reduced as contribution of Cav1.3 increased. For example, with 0% of $Ca_v1.3$ in I_{CaL}, the CL shortening caused by CRU randomness was 31%, but only 15% with 100% of $Ca_v1.3$ in I_{CaL} (green arrow vs. aqua arrow in Fig.11 A).

3) Mechanisms of CL reduction by $Ca_v1.3$ isoform and their interplay with effects of CRU randomness are shown in Fig. A4 and Fig. A5. The mechanisms are consistent with the concept of ignition (Lyashkov et al., 2018) that includes interactions of I_{CaL}, I_{NCX}, and CRUs (LCRs). For both square lattice and uniformly random distributions of CRUs, $Ca_v1.3$ substantially accelerated

389 the timing and the rate of CRU recruitment that, in turn, accelerated I_{NCX} and diastolic
390 depolarization. During diastolic depolarization, $Ca_v1.3$ (vs. $Ca_v1.2$) not only causes stronger and
391 earlier recruitment of CRUs to fire, but also generates a larger inward current due to its lower
392 activation voltage of around -55 mV (vs. -40 mV).
393 4) $Ca_v1.3$ increases robustness of pacemaker function: inclusion of only 20% of $Ca_v1.3$ into I_{CaL}
394 was sufficient to revive spontaneous AP firing in the SAN cell model with decreased g_{CaL} and
395 square lattice distribution of CRUs (Fig. A6) which was similar to the effect of CRU randomness
396 described above (Fig. 7D).
397 5) We also tested whether the CRU randomness has any effect on βAR stimulation in the model
398 with $Ca_v1.3$. This was tested in one model scenario with 50% of $Ca_v1.3$ in I_{CaL}. A similar
399 substantial contribution (~60%) has been demonstrated in mouse SAN cells (Christel et al.,
400 2012) and we kept it substantial in this test in the absence of literature data for rabbit. Our
401 simulations showed that while the average CL was substantially longer in the case of square
402 lattice vs. uniformly random distribution of CRUs (318.4 ms vs. 260.8 ms, Fig. 11 B) in basal
403 state firing, the CL converged to about the same level (247.8 ms vs. 236.6 ms Fig. 11 C) in the
404 presence of βAR stimulation, clearly showing a stronger overall effect in case of the square
405 lattice CRU distribution (22.2% vs. 9.3% of CL reduction), i.e. qualitatively similar to our result
406 with the I_{CaL} model with 100% $Ca_v1.2$ (Fig. 9).
407
408 **Importance of L-type channel coupling to CRUs**
409 Our previous results with local Ca control models (Maltsev et al., 2011) (Maltsev et al., 2013;
410 Stern et al., 2014) (Maltsev et al., 2017b), the ignition theory of pacemaking (Lyashkov et al.,
411 2018), and the results of the present study indicate the crucial importance of local, intimate

interactions among CRUs, NCX, and LCCs, suggesting that clustering LCCs with RyRs can be important not only for normal excitation-contraction coupling in cardiac muscle cells, but also for cardiac pacemaking. Next, we performed a series of simulations to test this idea using a modification of our model, in which we artificially uncoupled $Ca_v1.2$ currents from CRUs. In these simulations $Ca_v1.2$ currents were uniformly distributed over the cell membrane, while Cav1.3 currents remained coupled with CRUs. Our sensitivity analysis (similar to shown in Fig.11 A) revealed strong regulation of CL duration by both CRU randomness and $Ca_v1.3$ (Fig. A7). However, the robustness of AP firing in these cell models was substantially decreased. Indeed, while normal automaticity was present for the entire range of $\%Ca_v1.3$ in the fully coupled channel models, the partially uncoupled models failed to generate spontaneous APs with $\%Ca_v1.3$ being below 20% with random CRU distribution and below 30% with square lattice distribution (Fig. A7).

Discussion

Results summary:

The focus of the present study was to investigate if disorder in CRU positions under cell membrane has any notable effect on pacemaker SAN function. We used an upgraded numerical SAN cell model featuring a Ca clock at the level of the local CRU network, coupled to the cell membrane electrophysiology equations. As the extent of disorder in the CRU positions increased, SAN function was assessed via its spontaneous AP firing rate or CL. Spatial disorder increased both the firing rate and robustness of pacemaker function in the basal state. The disorder decreased the CRU nearest neighbor distances and facilitated Ca release propagation via CICR. This leads to an earlier and stronger LCR signal that increased AP firing rate and also

initiated AP firing in cells that could not fire APs with fully ordered square lattice positioning of CRU. The magnitude of the effect on the firing rate was substantial, quantitatively similar to that known for βAR stimulation. However, the boost of robustness bears a cost in the flexibility of pacemaker function. The range of AP firing rate modulation by βAR stimulation substantially narrowed as disorder and its attendant robustness increase. This happens because the disorder-facilitated release synchronization utilizes a majority of CRUs in the basal state and leaves a smaller fraction (i.e. a smaller "reserve") of CRUs to be recruited in AP ignition during βAR stimulation.

Upgraded CRU-based model of SAN cell

An important result of the present study was a major upgrade of our previous CRU-based model of rabbit SAN cell (Maltsev et al., 2011; Maltsev et al., 2013) (Fig.1, see Appendix for more details). Timing for CRU activation was previously defined phenomenologically via a fixed refractory period followed by a Poisson process, whereas termination was set simply to a mean value of spark duration. Both the refractory period and spark duration were taken directly from experimental measurements. The new model includes Ca release activation and termination mechanisms linked SR Ca load as shown in experimental and theoretical studies (Zima et al., 2008; Maltsev and Lakatta, 2009; Imtiaz et al., 2010; Vinogradova et al., 2010; Zima et al., 2010; Laver et al., 2013; Stern et al., 2013; Maltsev et al., 2017a; Veron et al., 2021). These model enhancements are of crucial importance for this and future studies. Firstly, the new model reflects recent progress in our understanding of RyR function. Secondly, it describes mechanistically the coupling of the Ca clock to the membrane clock at the scale of the local CRU network. This is an important niche in the variety of numerical SAN cell models developed thus

458 far. As described in details in Methods section and Appendix, its sub-micron scale (e.g. (Nivala
459 et al., 2012) in ventricular myocytes) is positioned between simple common pool models (e.g.
460 (Kurata et al., 2002; Maltsev and Lakatta, 2009; Severi et al., 2012)) and extremely complex
461 RyR-based models (Stern et al., 2014; Maltsev et al., 2017b).

462 The models at each level of signal integration are important for understanding the "big
463 picture", i.e. how the phenomenon of heartbeat emerges, bridging the gap between scales
464 (Clancy and Santana, 2020; Weiss and Qu, 2020) in the spirit of multiscale modeling (Qu et al.,
465 2011). The CRU-based modeling of SAN cells has become especially helpful for future research
466 with respect to recent discoveries of importance of local Ca signaling for SAN tissue function
467 (Bychkov et al., 2020). It was shown that Ca signals are markedly heterogeneous in space,
468 amplitude, frequency, and phase among cells comprising an HCN4+/CX43- cell meshwork of
469 SAN, and synchronized APs emerge from heterogeneous subcellular subthreshold Ca signals
470 (modelled here, see Fig. 8)). Cell heterogeneity and biological noise are key determinants of
471 robust cardiac pacemaking (Guarina et al., 2022; Maltsev et al., 2022).

472 While a series of insightful multicellular models of SAN tissue have been developed (see
473 for example (Oren and Clancy, 2010; Inada et al., 2014; Gratz et al., 2018; Li et al., 2018)), local
474 Ca signaling has not been numerically studied at the tissue level yet. Our new CRU-based model
475 has relatively low computational cost and it generates LCRs observed experimentally both in
476 isolated cell and in intact SAN and, thus, it can be used as a functional unit in future multi-
477 cellular modeling to investigate the role of local Ca signaling at the level of SAN tissue at the
478 frontier of heart pacemaker research (Clancy and Santana, 2020; Weiss and Qu, 2020). One
479 second of simulation of our model requires about 12 min of computation time via one thread of
480 Intel® Xeon® W-2145 CPU @3.7GHz. Modern video cards can run several thousands of

processing units. For example, TITAN RTX features 4608 CUDA cores running at 1.77 GHz. If a single CUDA core can be programmed to run the present single cell model, then running thousands of such models in parallel would simulate a respective tissue model comprised of these many-cell models in reasonable time, like for the single cell model presented here. New theoretical insights into SAN tissue function can be, in fact, achieved in tissue models comprised of as low as 49 cells (7x7 grid) (Gratz et al., 2018). Our recent investigation of GPU-based model of SAN tissue included 625 cells (25x25 grid) (Maltsev et al., 2022).

Mechanisms of the CRU spatial disorder effect

Empty spaces and clusters are an intrinsic feature of random spatial distributions known as Poisson clumping. Such emerging CRU clumps are clearly seen by eye in our examples of 2D representations of CRU networks in Fig. 2 (left panels), and the clustering effect is quantitatively manifested by a broader distribution of nearest-neighbor distances with notably shorter averages (right panels). The disorder in CRU positions creates shortcuts, making it easier for Ca to reach a neighbor via CICR propagation and thus promoting CRU recruitment and synchronization. Once the Ca release becomes more synchronized, LCR sizes increase, the amplitude of LCR net diastolic signal also increases, and, very importantly, the timing of net LCR signal simultaneously shortens, as we previously demonstrated (Maltsev et al., 2011). Further effect of LCRs on AP firing rate is executed via NCX and I_{CaL} to accelerate diastolic depolarization (Figs 4, 5, and 10) as postulated in the coupled-clock theory (Maltsev and Lakatta, 2009; Lakatta et al., 2010) and more recent ignition theory (Lyashkov et al., 2018), in line with previous numerical studies in a CRU-based SAN cell model (Maltsev et al., 2013) and RyR-based model (Stern et al., 2014).

The Ca release synchronization mechanism via local CRU recruitment is impacted by many factors including for example I_{spark} , i.e. Ca release flux of a single CRU which we studied previously (Maltsev et al., 2011). It is determined by SR Ca refilling kinetics, driven by PKA-dependent phosphorylation of Ca cycling proteins (Vinogradova et al., 2006; Lakatta et al., 2010). Mechanistically speaking, Ca clock ticks during diastole when SR refills to a certain threshold level so that Ca current via a single RyR channel becomes big enough to recruit its neighboring RyRs within CRU to generate a spark (Zima et al., 2010; Veron et al., 2021) and then I_{spark} becomes large enough to generate an LCR, i.e. a series of propagating sparks that depends on the local CRU distribution. Thus, the recruitment phase becomes delayed if the nearest-neighbor distances are larger (such as in square lattice arrangement) and require a larger SR Ca loading commensurate with larger I_{spark} to begin with. And vice versa, the recruitment starts earlier in the cycle if some of nearest-neighbor distances are shorter (such as in uniformly random arrangement).

With larger nearest-neighbor distances in the square lattice setting, many CRUs never fire during diastole in basal state beating, but become recruited during βAR stimulation (Fig. 10). For example, in basal state on average about 44% of CRUs fired at -35 mV (i.e. the end of diastolic depolarization) in the uniformly random model, but only 29% in the lattice model; however, during βAR stimulation about 53% of CRUs fired in either case, i.e. CRUs became equally well recruited independent of the model. Thus, the slower recruitment and the non-recruited CRUs in the basal firing represent chronotropic reserve mechanisms that are utilized during βAR stimulation. The reserve is obviously limited by the number of CRUs, and if more CRUs are recruited to fire in each diastole in basal state, then the number of CRUs in reserve shrinks (and vice versa); that is why βAR stimulation effect is much smaller in the uniformly random model

vs. lattice model. This result is evidence of possible functional importance of the chronotropic reserve linked to CRU recruitment: We have previously demonstrated that CRU recruitment stabilizes diastolic I_{NCX} amplitude that explained, for example, a paradoxical effect of partial knockout of NCX in mice to reduce chronotropic reserve with no effect on the basal rate (Maltsev et al., 2013).

Possible importance for normal function, pathological conditions, and aging

Thus far CRU distribution in SAN cells has not been systematically studied. However available data indicate that locations of CRUs in SAN cells do not form a perfect grid, but exhibit a notable degree of randomness (Lyashkov et al., 2007; Stern et al., 2014). Different SAN cells may have different CRU arrangement: central SAN cells have a substantial degree of disorder in their RyR cluster positions, whereas peripheral cells feature striations and more organized RyR clustering (Rigg et al., 2000; Musa et al., 2002). Our result may indicate that the central cells are capable of robustly generating high frequency signals, but unlikely to have a substantial CRU recruitment reserve to utilize during βAR stimulation (they may still have other mechanisms to increase their rate). On the contrary, the cells with more organized RyR clustering (wherever they are) may have a larger CRU recruitment reserve. Thus, the difference in spatial geometry of the CRU network in different parts of the SAN and, hence, the associated difference in βAR stimulation may contribute to the leading pacemaker site shifts during βAR stimulation (Brennan et al., 2020).

The real CRU distribution is neither uniformly random, nor perfectly spaced. By adjusting the CRU positioning, SAN cells can reach a balance of robustness and flexibility. This balance is required (and dictated) for each cell by its specific location and functional role within

550 the cellular network of SAN tissue. This could be important for regulation of βAR stimulation
551 response among individual cells within SAN tissue for its optimal integrated chronotropic
552 response (Brennan et al., 2020; Yuan et al., 2020; Kim et al., 2021). Here we show that the CL
553 decrease during βAR response depends linearly on the CL in the basal state. This finding is line
554 with recent experimental results that βAR stimulation synchronizes a broad spectrum of AP
555 firing rates in SAN cells toward a higher population average (Kim et al., 2021).

556 Another possible importance of the disorder-facilitated AP firing could be regulation of
557 cell dormancy, a recently discovered phenomenon manifested by the absence of automaticity of
558 SAN cells that can be acquired via βAR stimulation (Kim et al., 2018; Tsutsui et al., 2018;
559 Tsutsui et al., 2021). One important factor of cell dormancy is a lower density of I_{CaL} (Tsutsui et
560 al., 2021). Here we show that by rearranging its CRU positions, a SAN cell with a low I_{CaL}
561 density can switch its functional state between being dormant or AP firing, as illustrated in Fig.
562 7. Nonfiring cells have also been recently found in intact, fully functional SA node (Bychkov et
563 al., 2020; Fenske et al., 2020); their numbers substantially varied in different chronotropic states
564 of the SAN (Fenske et al., 2020). A proposed new pacemaker mechanism involves synchronized
565 cardiac impulses emerging from heterogeneous local Ca signals within and among cells of
566 pacemaker tissue, including subthreshold signals in non-firing cells (Bychkov et al., 2020). Here
567 we show that subthreshold V_m oscillations in case of uniformly random distribution are much
568 more powerful and occurred at a faster frequency vs. those in the square lattice model (Fig. 8).
569 Thus, the spatial CRU distribution can regulate the capacity of cells to generate synchrony of
570 impulses via subthreshold signaling.

571 Another interesting result of our sensitivity analysis is that the model with the perfect
572 square lattice CRU locations (before it failed) was capable of generating AP firing with much

longer CL (i.e. at a low rate of excitations), whereas in uniformly random scenario the model failed at a shorter CL (i.e. cannot reach lower rates) (Fig. 7 B, C). Thus, pacemaker cells can harness this mechanism linked to CRU distribution to reach lower rates in addition to other known bradycardic mechanisms such as shift in voltage activation of I_f (DiFrancesco and Tromba, 1988), $I_{K,Ach}$, and protein dephosphorylation (decreasing clock coupling) (Lyashkov et al., 2009). By having more regular spacing, SAN cells can generate APs at slower rates, without any additional specific Ca- or voltage-dependent mechanisms, which may be more threshold sensitive.

Pathological conditions and aging are usually associated with disorder in molecular positions, interactions, and functions. We demonstrate that excessive disorder in CRU positions within SAN cells decreases fight-or-flight response while shrinking the range of lower AP rates (Figs 7 B and 9), and hence can explain, in part, the limited range of heart rates associated with age and in disease. On the other hand, the mechanism of disorder-facilitated Ca release propagation can act together with increased sympathetic tone to compensate the age-intrinsic heart rate range decline with age (Tsutsui et al., 2016). With respect to atrial and ventricular cells, excessive disorder in CRU positions (in cardiac disease) is expected to facilitate Ca release propagation, i.e. waves formation, increasing the risk of life-threatening arrhythmia (Ter Keurs and Boyden, 2007).

A broader interpretation: living systems harness disorder to function

While noise is a broad term that is usually associated with undesirable disturbances or fluctuations, many biological systems harness disorder to function. Randomness creates opportunities to exceed a threshold that is above the mean, analogous to the way a quantum

particle can tunnel across a barrier while a classical deterministic particle cannot. It can improve signal transmission or detection, e.g. via stochastic resonance (McDonnell and Abbott, 2009). Random parameter heterogeneity among oscillators can consistently rescue the system from losing synchrony (Zhang et al., 2021). Randomness is critical for cardiac muscle cell function. The local control theory developed by Michael Stern in 1992 (Stern, 1992) predicted the Ca sparks (found later experimentally (Cheng et al., 1993)) and explained smooth regulation of excitation-contraction coupling in cardiac muscle via statistics of success and failure of a CRU to generate a spark when LCCs open. We have recently shown that statistical physics approach is also helpful to understand spontaneous Ca spark activation and termination (via Ising formalism (Maltsev et al., 2017a; Maltsev et al., 2019; Veron et al., 2021)). In the present study we show that disorder could be also important for cardiac pacemaker function: disorder in CRU locations determines statistics of success and failures for a firing CRU to recruit to fire its neighboring CRU, observed as propagating LCRs that are critical for SAN cell function (Lakatta et al., 2010). Thus, disorder in CRU positions facilitates functional order in terms of LCR emergence via self-organization by means of positive feedback provided by CICR, culminating in higher AP firing rates, whereas order in CRU positions is associated with individual stochastic sparks, i.e. functional disorder for a major part of the diastolic depolarization duration, culminating in lower AP firing rates. A broader interpretation of our results is that disorder in a network featuring diffusion-reaction interactions can facilitate excitation propagation, that may be applicable to RyR arrangement within a CRU to generate a spark (down-scale) or cell-to-cell interactions in SAN tissue to generate cardiac impulse (up-scale).

Importance of $Ca_v1.2$ and $Ca_v1.3$ isoforms

618 According to a modern ignition theory (Lyashkov et al., 2018), the diastolic depolarization is
619 realized by positive feed-back mechanisms among CRUs (i.e. LCRs), I_{NCX}, and I_{CaL} via their
620 intertwined Ca and voltage dependencies. Ca currents play a key role in generating LCRs during
621 diastolic depolarization via CICR (Huser et al., 2000; Bogdanov et al., 2001; Chen et al., 2009;
622 Torrente et al., 2016). Therefore, in addition to I_{CaL} density, I_{CaL} voltage dependence (especially
623 within the range of diastolic depolarization) must be important. Studies in mice demonstrated
624 specific importance of the $Ca_v1.3$ LCC isoform with a lower voltage activation threshold (vs.
625 cardiac isoform $Ca_v1.2$) for pacemaker function (Mesirca et al., 2015). An indication of $Ca_v1.3$
626 general importance (rather than just specific to mouse) is that the loss of $Ca_v1.3$ function is
627 associated with a human channelopathy linked to bradycardia (Baig et al., 2011). Because
628 specific contribution of $Ca_v1.3$ in rabbit SAN cells is presently unknown and $Ca_v1.3$ expression
629 shows a substantial cell-to-cell variability (recently shown in mouse SAN cells via
630 immunolabeling technique (Louradour et al., 2022)), we performed a full-scale sensitivity
631 analysis varying Cav1.3 percentage from 0 to 100%.
632 Our simulations show that inclusion of $Ca_v1.3$ in I_{CaL} can provide a stronger and earlier
633 recruitment of CRUs to fire during diastolic depolarization (Fig. A4 and Fig. A5) supporting and
634 providing further insights to previous studies which proposed that Cav1.3 regulates RyR-
635 dependent Ca release during SA node pacemaker activity (Christel et al., 2012; Torrente et al.,
636 2016; Louradour et al., 2022). We also found interesting interplay between $Ca_v1.3$ and CRU
637 randomness (Fig. 11 A, see details in Results). Their effects are complementary. CRU
638 randomness generates additional CL shortening on top of the $Ca_v1.3$ effect (Figure 11 A, green
639 arrow), and $Ca_v1.3$ can also generate an additional CL shortening on the top CRU randomness
640 (Figure 11 A, blue arrow). On the other hand, total CL shortenings are less than the formal sum

641 of the effects, because both factors compete for CRU recruitment and accelerate AP firing via the
642 same ignition process. Thus, each factor decreases the CL modulatory range of the other: the
643 presence of randomness in CRU locations decreases the effect of Cav1.3, and vice versa,
644 expression of Cav1.3 decreases the effect of the CRU randomness.

645 Increasing relative contribution of $Ca_v1.3$ boosts robustness of pacemaker function. For
646 example, only 20% of $Ca_v1.3$ in I_{CaL} can revive normal automaticity in a dormant cell with weak
647 CICR among CRUs located in a square grid (Fig. A6). Finally, while our simulations
648 demonstrated that strong expression of Cav1.3 (and concomitant high basal rate) decreases the
649 effect of βAR stimulation (compare Fig. 11 B, C, with Fig. 9 B), SAN cells with higher basal
650 rates showed smaller responses to βAR stimulation also in experimental studies (Kim et al.,
651 2021). On the other hand, the inhibitory effect of CRU randomness on βAR stimulation is
652 preserved in cells with high expression of $Ca_v1.3$. For example, our model with 50% of $Ca_v1.3$ in
653 I_{CaL} exhibited a much smaller effect of βAR stimulation in case of unfirmly random CRU
654 distribution vs. square lattice distribution (9.3% vs. 22.2% of CL reduction).

655 Our simulations also showed that cell models with artificially uncoupled Cav1.2 currents
656 from CRUs exhibited a larger modulatory range of Cav1.3 but less robust peacemaking (Fig.
657 A7), pointing to functional importance of local crosstalk of CRUs with both Cav1.2 and Cav1.3
658 channels, despite Cav1.2 having a higher activation voltage threshold. Thus, clustering LCCs
659 with RyRs can be of general importance, not only for normal excitation-contraction coupling in
660 cardiac muscle, but also for cardiac pacemaking. Uncoupling LCC from RyR in pathological
661 conditions and aging can deteriorate cardiac pacemaker function.

662

663 ***Limitations and future studies***

In our previous study we showed that a CRU network lacking release propagation can acquire release propagation capability by introducing a subset of smaller "bridging" CRUs that create propagation shortcuts and allow sparks to jump from one firing CRU to its neighbor (Stern et al., 2014). In the present study we show that bridging of CRU network is not required to achieve release propagation: the intrinsic disorder in CRU positions can naturally create the bridges and propagation shortcuts without additional bridging CRUs. On the other hand, our study is of a reductionist type focused on the disorder contribution, whereas the realistic CRU distribution in SAN cells has more complex, hierarchical structure that includes CRUs of various sizes (Stern et al., 2014). Thus, future studies will clarify the role of disorder in the more realistic settings with different CRU sizes and more precise CRU locations within the cell measured by super resolution microscopy in 3D (pilot studies (Maltsev et al., 2016; Greiser et al., 2020)) rather than by confocal microscopy in tangential sections (Stern et al., 2014). Furthermore, RyR distribution is dynamic (Asghari et al., 2020) and spacing between CRUs becomes shortened in failing hearts (Chen-Izu et al., 2007). Future studies on the cellular and molecular mechanisms regulating CRU distribution dynamics within cardiac cells will clarify how CRU order/disorder contributes to cell physiological and pathological function. While our numerical simulations show clearly a notable effect of disorder in CRU positions on Ca release synchronization and spontaneous AP firing, the theoretical mechanisms of this synchronization merit further studies. Based on our numerical study one can envision that synchronization is happening as a critical phenomenon, with the criticality depending on model parameters, including spatial randomness of the CRUs. Possible approaches to study such systems with criticalities include a percolation phase transition or Ising formalism, similar to what has been recently suggested for RyR interactions via CICR within CRUs (Maltsev et al., 2017a; Maltsev et al., 2019). While we tested possible functional effects of

687 $Ca_v1.3$, the exact contribution of $Ca_v1.3$ into total I_{CaL} and biophysical properties of $Ca_v1.3$
688 current in rabbit SAN cells are presently unknown and require further elucidation.

689 ***Conclusions***

690 The rate of Ca release propagation is an important feature of both normal and abnormal Ca
691 release signals in cardiac cells. Using numerical modeling here we show that disorder in CRU
692 locations increases the synchronization of Ca release in SA node pacemaker cells. This impacts
693 on their pacemaker function via NCX current accelerating diastolic depolarization. While the
694 disorder increases the rate and robustness of spontaneous AP firing, it simultaneously decreases
695 βAR stimulation effect and the low range of lower rates. Our simulations also showed that
696 $Ca_v1.3$ strongly recruits CRUs to fire during diastolic depolarization, thereby increasing AP
697 firing rate and complementing effects of CRU distribution. Thus, order/disorder in CRU
698 locations together with $Ca_v1.3$ expression regulates CRU recruitment and synchronization to fire
699 during diastolic depolarization and could be harnessed by pacemaker cells to regulate their
700 function. Excessive CRU disorder and/or overexpression of $Ca_v1.3$ boost pacemaker function,
701 but can limit heart rate range that may contribute to heart rate range decline with age and in
702 disease.

703 **Acknowledgments**

704 This research was supported in part by the Intramural Research Program of the National
705 Institutes of Health, National Institute on Aging. A.V.M. acknowledges the support of the Royal
706 Society University Research Fellowship UF160569.

707 **Disclosures:** None

708

APPENDIX

Detailed methods

1. General description of the model

In the present study we performed a major update of our previous CRU-based numerical model of a central rabbit SAN cell (Maltsev et al., 2011; Maltsev et al., 2013). The model formulations for cell membrane currents are adopted from 2009 Maltsev-Lakatta model (Maltsev and Lakatta, 2009) that, in turn, stems from 2002 Kurata et al. (Kurata et al., 2002). The LCR in the model is approximated at the scale of an individual CRU that represents a cluster of Ca release channels (ryanodine receptors, RyR) embedded in theJSR, i.e. a Ca store located in close proximity to cell surface membrane, with only 20 nm of separation via a dyadic space. Each JSR is diffusely linked to the network of FSR that uptakes Ca from cytosol via SERCA pumping. Individual release channels are not modelled here, but we translate recent findings of RyR studies to the CRU level to introduce respective spark activation and termination mechanisms. All CRUs are identical and located in an equally-spaced square grid under the cell membrane. The model allows each CRU position to vary around its original square lattice position to generate a variety of intermediate distributions with various degrees of disorder from perfect square lattice to uniformly random. The specific aims of the present study were to update the model and to investigate how the disorder in CRU positions influences SAN cell function.

2. Cell geometry, compartments, voxels and membrane patches

We model a small SAN cell shaped as a cylinder of 53.28 μm in length and 6.876 μm in diameter. The cell membrane electrical capacitance of 19.8 pF is similar to that of 20 pF in Zhang et al. model (Zhang et al., 2000) of a central SAN cell. Details of local Ca dynamics under

the cell membrane are simulated on a sub-micron resolution (120 nm) square grid that divides the cell membrane and the submembrane space (dubbed subspace) into respective membrane patches and subspace voxels. Locations within the grid are defined by coordinates in the respective plane of the cell surface cylinder: along the cylinder (*x* axis) and around the cell cross-section (*y* axis). Our cell partitioning and respective voxel sizes to reproduce LCRs observed experimentally are schematically illustrated in the main text Fig. 1. To avoid special considerations at the cell borders, the ends of the cylinder are connected (yielding a torus). Our cell compartments and voxel structure are essentially similar to that in Stern et al. model (Stern et al., 2014) that approximates Ca dynamics in 3 dimensions at the single RyR scale. However, we limited the cell partition to only three nested layers of voxels of substantially different scales reflecting respective essential Ca cycling components and processes happening at these scales (described below).

2.1. Submembrane voxels

The first, most detailed level of approximation of local Ca dynamics is via 79920 voxels (444 in *x* and 180 in *y*) of very small size 120x120x20 nm under the entire cell membrane including the dyadic space (or cleft space) separating CRUs and the cell membrane. This thin layer of voxels describes local Ca release from individual CRUs, CRU-to-CRU interactions via Ca diffusion and CRU interactions with cell membrane (including I_{CaL}, I_{NCX}, I_{CaT}, and I_{bCa}). Ca currents were computed for each membrane patch (120x120 nm) to generate local Ca fluxes contributing to local Ca dynamics.

2.2. JSR level voxels (dubbed “ring” voxels)

The next approximation level of Ca dynamics is a deeper layer of voxels that have a larger size of 360x360x800 nm ($\Delta x \Delta y \Delta r$) that includes the scale of JSR depth (60 nm). Each ring voxel has its cytoplasmic part and FSR part and some ring voxels are diffusively connected to JSRs (main text Fig. 1). While it appears that the geometric scale of ring voxel is of an order of magnitude larger than the JSR size, the actual FSR volume within each ring voxel is comparable with the JSR volume (described below in details). Thus, this level of voxels describes the local dynamics of Ca transfer from FSR to JSR as well as enhanced local Ca pumping and diffusion fluxes due to close proximity to Ca release and Ca influx in its neighboring submembrane voxels.

2.3. The core

In contrast to Stern model (Stern et al., 2014), the rest of the cell in our model does not have further geometric partitioning and it is lumped to one compartment “the core”, where local Ca dynamics is less important. The core also has its cytosolic and FSR parts (as in ring voxels). Thus, it describes the bulk Ca uptake from cytosol to FSR and further accumulation, diffusion, and redistribution of the pumped and released Ca within the cell interior.

2.4. JSR

We place JSRs inside the respective ring voxels just below their outer side facing the cell membrane (main text Fig. 1). JSR volume (~7.8 attoliter) is comparable with the volume of a ring voxel (~91 attoliter) and the same volume cannot be occupied twice by different cell compartments. Therefore, volumes of the ring voxels are kept the same by their extending into the core by the exact volume that the JSR occupies at their outer side. Thus, the actual core

778 volume was calculated as the volume of the cylinder core decreased by the volume of all JSR
779 volumes. We simulated different degree of disorder of JSR positions by a random number
780 generator within a Gauss distribution along *x* and *y* (centered at the square lattice vertices) with a
781 given SD that was the same for *x* and *y* directions. The model scenario with uniformly random
782 positioning of CRU centers was also generated by a random number generator but with equal
783 probability to occur in any submembrane voxel. JSR overlaps are excluded, i.e. any two JSRs
784 cannot occupy the same cell volume.
785
786 **3. Ca CYCLING**
787 **3.1. Free SR (FSR)**
788 As mentioned above, each ring voxel and the core is further partitioned into cytosol and FSR
789 fractions. We modelled FSR as homogeneously distributed network within the cytosol. The
790 cytosol fraction was set to 0.46 and FSR fraction to 0.035 (Stern et al., 2014). The remainder
791 presumably contains myofilaments, mitochondria, nucleus, and other organelles. In turn, each
792 FSR portion has capability to pump Ca locally from the respective cytosol portion of the same
793 voxel, simulating local SERCA function. Because the submembrane voxels are extremely thin,
794 only 20 nm depth, their contribution to Ca pumping and intra-SR diffusion are negligible and not
795 modelled.
796
797 **3.2. SR Ca pump**
798 The SERCA pump is present uniformly throughout the cell, transferring Ca from the cytosolic to
799 the FSR compartment of each voxel (of ring and core) with Ca uptake rate given by the
800 reversible Ca pump formulation adopted from Shannon et al. (Shannon et al., 2004)

$$j_{up} = P_{up} \frac{V_{\max} \cdot \left(\frac{Ca_{cyt}}{K_{mf}} \right)^H - V_{\max} \cdot \left(\frac{Ca_{FSR}}{K_{mr}} \right)^H}{1 + \left(\frac{Ca_{cyt}}{K_{mf}} \right)^H + \left(\frac{Ca_{FSR}}{K_{mr}} \right)^H} \quad (1)$$

where P_{up} = 0.014 mM/ms, K_{mf} = 0.000246 mM, K_{mr} = 1.7 mM, and H = 1.787.

3.3. Ca diffusion within and among cell compartments

Ca diffusion fluxes between voxels within and among cell compartments are approximated by the first Fick's law:

$$J = - D \cdot \Delta[Ca]/\Delta x$$

where D is a diffusion coefficient, and $\Delta[Ca]/\Delta x$ is Ca concentration gradients, i.e. $\Delta[Ca]$ is the concentration difference and Δx is the distance between the voxel centers.

The respective rate of change of [Ca] is defined as

$$\mathrm{dCa/dt} = J \cdot s / v$$

where s is the diffusion area sharing by voxels and v is the receiving volume. Thus,

$$dCa/dt = - D \cdot (\Delta[Ca]/\Delta x) \cdot s/v$$

For any two diffusively interacting voxels with volumes v_1 and v_2, Ca dynamics is described by a set of differential equations:

$$dCa_1/dt = (Ca_2 - Ca_1)/\tau_1$$

$$dCa_2/dt = (Ca_1 - Ca_2)/\tau_2$$

where Ca_1 and Ca_2 are Ca concentrations in the respective voxels and

$$\tau_1 = v_1 \cdot \Delta x / (D \cdot s)$$

$$\tau_2 = v_2 \cdot \Delta x / (D \cdot s)$$

822 τ_1 (or τ_2, symmetrically) is the respective time constant of Ca_1 change in time in a special case if
823 the other compartment with volume v_2 is substantially larger than v_1 (i.e. $v_2 >> v_1$) and therefore
824 Ca_2 remains approximately constant. In general case, the set is analytically solved to the
825 respective exponential decays:

826 $$Ca_1(t) = (Ca_1(0) - C_\infty) \cdot exp(-t/\tau) + C_\infty$$

827 $$Ca_2(t) = (Ca_2(0) - C_\infty) \cdot exp(-t/\tau) + C_\infty$$

828

829 where $C_\infty = (Ca_1(0) \cdot v1 + Ca_2(0) \cdot v_2)/(v_1 + v_2)$ is equilibrium concentration (t = ∞) in both
830 voxels defined by the matter conservation principle and $\tau = \tau_1 \cdot \tau_2/(\tau_1 + \tau_2)$ is the common time
831 constant of the exponential decay of the system to reach the equilibrium. The respective Ca
832 change from its initial value in voxel v_1 over time is given as follows

833 $$\Delta Ca_1(t) = (C_\infty - Ca_1(0)) \cdot (1 - exp(-t/\tau))$$

834 Then, by substituting C_∞ we get:

835 $$\Delta Ca_1(\Delta t) = (v2/(v1+v2)) \cdot (Ca_2(0) - Ca_1(0)) \cdot (1 - exp(-\Delta t/\tau))$$

836 $$\Delta Ca_2(\Delta t) = -(v1/(v1+v2)) \cdot (Ca_2(0) - Ca_1(0)) \cdot (1 - exp(-\Delta t/\tau)) = -\Delta Ca_1(t) \cdot v_1/v_2$$

837 These formulations were used in all our computations of [Ca] changes for all neighboring voxels
838 within and among cell compartments for the model integration for each time update Δt (during
839 time tick or several time ticks for slower processes). In our computer algorithm we calculated the
840 fractional Ca change (*FCC*) before the model run and used it simply as a scaling factor to
841 determine actual [Ca] change from the difference in [Ca] between any two diffusely interacting
842 voxels at the beginning of each integration step (from $t=0$ to $t=\Delta t$). Thus,

843 $$FCC = (v2/(v1+v2)) \cdot (1 - exp(-\Delta t/\tau)) \quad \text{(calculated before model run)}$$

844 $$\Delta Ca_1(\Delta t) = FCC \cdot (Ca_2(0) - Ca_1(0)) \quad \text{(calculated during model run)}$$

$$\Delta Ca_2(\Delta t) = -\Delta Ca_1(t) \cdot v_1/v_2 \qquad \text{(calculated during model run)}$$

In the case of identical voxels, i.e. within subspace and within ring (i.e. when $v_1 = v_2$ and $\tau_1 = \tau_2$) the formulations are simplified to:

$$FCC = 0.5 \cdot (1-exp(-2 \cdot \Delta t/\tau_1))$$

Note 1: If $\Delta t/\tau_1 << 1$ then *FCC* can be approximated (e.g. via respective Taylor series) as

$$FCC = \Delta t/\tau_1 = \Delta t \cdot D \cdot s/(v_1 \cdot \Delta x)$$

Further, if v_1 can be described as $v_1 = s \cdot \Delta x$, e.g. for diffusion along the cell length (axis *x* in our model) *FCC* can be further simplified to

$$FCC = \Delta t \cdot D/\Delta x^2$$

However, because *FCC* is calculated only once before the model run and does not carry any additional computational burden during actual simulations of Ca dynamics, we always used here the full approximation for the diffusion, i.e. more precise exponential decay, rather than a linear change over Δt. An advantage of this approach is that the model features more stable behavior in case we want to vary cell geometry, cell compartments, voxel sizes, or integration time (Δt).

Note 2: We have only a fraction of cell volume occupied with cytosol (or FSR). However, the same fraction will be for *v* and *s* in τ formulations and it cancels. The volume ratios $v_2/(v_1+v_2)$ and v_1/v_2 remain also unchanged because the fraction factor also cancels. Thus, all above formulations with formal geometric volumes are also valid for fractional volumes, assuming that the fraction of cytosol (or FSR) is evenly distributed within the volume.

3.5. Junctional SR (JSR) and Ca diffusion between JSR and FSR

The JSRs are located in close proximity to the cell membrane separated only by the layer of submembrane voxels of 20 nm depth, representing the dyadic space. Thus, each CRU releases Ca (described below) into its neighboring subspace voxels (occupying the dyadic space). Each CRU is refilled with Ca locally from FSR network via a fixed diffusional resistance. In previous common pool models (Kurata et al., 2002; Maltsev and Lakatta, 2009) diffusion between JSR and FSR was described by a simple exponential transfer process with a fixed time constant (τ_{tr} =40 ms). Here we want to have a similar Ca transfer rate for each JSR, but locally. The τ_{tr} value in common pool models is for the whole cell FSR volume that is substantially larger than JSR volume. Here, in the local model, each JSR is linked diffusively to FSR. Depending on its position, JSR can be connected to one ring voxel, 2 voxels, or 4 voxels. To get the respective share of the Ca flux, we split and distribute the Ca diffusion flow into 9 elementary surface areas (120 nm x 120 nm) of the JSR (360x360 nm), each of which is connected to the respective ring voxel and transfer its Ca share with $\tau = 9 \cdot 40\ ms \cdot v_{FSR}/(v_{FSR} + v_{JSR}) = 104.58$ ms. Note: Because the FSR fraction of 0.035 within cell volume is rather small, each relatively large ring voxel of 360x360x800 nm (~91 attoliter) contains only a small FSR volume $v_{FSR} = 3.186$ attoliter. This is comparable (and even smaller) than the JSR volume in the model $v_{JSR} = 7.776$ attoliter.

3.6. Spark activation mechanism

Each CRU can be either in open or closed state. The capability of a given CRU to open, i.e. to generate a Ca spark, is controlled by its JSR Ca loading. Experimental and theoretical studies showed that sparks cannot be generated with SR Ca loading less than a certain critical level of

about 300 μm (Zima et al., 2010; Veron et al., 2021). This critical level Ca_{jSR} is implemented in our mechanism of spark activation by prohibiting CRU firing while SR Ca loading remains below 300 μM (*CaSRfire*). When JSR is refilled with Ca above the *CaSRfire* level, it can open. The switch from close state to open state is probabilistic. The probability density for a given closed CRU to open is described by a power function of Ca concentration (*Ca*) in the dyadic space. The probability for the CRU to open during a short time interval *TimeTick* is given by

$$p = ProbConst \cdot (Ca/Ca_{sens})^{ProbPower} \cdot TimeTick \qquad (2)$$

where Ca_{sens} = 0.15 μM sensitivity of CRU to Ca, *ProbConst* =0.00027 ms^{-1} is open probability rate at $Ca = Ca_{sens}$, and *ProbPower* = 3 defines the cooperativity of CRU activation by cytosolic Ca. Each time tick our computer algorithm tries to activate a closed CRU by generating a random number within (0,1). If this number less than *p*, then the CRU opens. The Ca current amplitude, I_{spark}, is defined by spark activation kinetics *a(t)*, RyR unitary current ($I_{RyR,1mM}$, the current via a single RyR at 1 mM of Ca gradient), the number of RyRs residing in the JSR (N_{RyR}), and concentration difference between inside and outside JSR:

$$I_{spark} = a(t) \cdot I_{RyR,1mM} \cdot N_{RyR} \cdot (Ca - Ca_{JSR}) \quad (3)$$

N_{RyR} is defined based on the surface area of JSR assuming a crystal-like structure for RyR positions separated by 30 nm. Thus, for our JSR *xy* area of 360 x 360 nm, we obtain 12 x 12 RyRs, i.e. N_{RyR} =144. $I_{RyR,1mM}$ is to set 0.35 pA (Stern et al., 2014). Spark activation is described as a single exponential time-dependent process to tune spark rise time to about 5 ms (Fig. A1) close to that reported in the literature (from 4 to 8 ms).

$$a(t) = 1 - exp(-t/\tau_{CRUactivation}) \qquad (4)$$

913 It is important to note that our new model spark initiation does not reflect an intrinsic time-
914 dependent refractory process; rather we implement here the idea that spark can occur only when
915 SR gets refilled to a critical level that the current amplitude of individual RyR can initiate
916 regenerative CICR among neighboring RyRs (Zima et al., 2010; Stern et al., 2013; Veron et al.,
917 2021) . Thus, the implementation of the new spark activation mechanism controlled by SR Ca
918 refilling represents a major advance of our model, because the spark activation timing is now
919 predicted by the model. Of note, our previous CRU-based SAN cell models (Maltsev et al.,
920 2011; Maltsev et al., 2013) implemented SR Ca refiling contribution phenomenologically via a
921 fixed parameter, the restitution time that was directly taken from experimental measurements.
922
923 **3.7. Spark termination mechanism**
924 We also introduced a new spark termination mechanism that is based on the current knowledge
925 in this research area (Laver et al., 2013; Stern et al., 2013; Maltsev et al., 2017a), i.e. a Ca spark
926 is generated via CICR among individual RyRs within a CRU and it sharply terminates due to
927 induction decay (Laver et al., 2013) or a phase transition (similar to that known in Ising
928 model)(Maltsev et al., 2017a) when RyR current $I_{RyR}(t)$ becomes too small (due to JSR Ca
929 depletion) to further support the CICR. The specific value of the critical current $I_{spark\_termination}$ is
930 defined by the RyR interactions and beyond the capability of our CRU-based model. But the
931 time when CICR wanes to the critical point is reflected by the amplitude of $I_{spark}(t)$ being
932 comparable with $I_{RyR}(t)$ at a given JSR load, so that only one or a very few RyRs remain open at
933 the termination time point when spark decays. Based on this logic, we tested a wide range of
934 $I_{spark\_termination}$ to generate sparks of various durations and found that spark termination is well
935 described with $I_{spark\_termination}$ set to a 0.175 pA. In our previous numerical model simulations and

Ising theory of spark (Maltsev et al., 2017a) spark termination happens when SR level depletes to a critical level of about 0.1 to 0.15 mM (for RyR clusters from 9x9 to13x13). Unitary RyR current I_{RyR} becomes very small at these SR levels, namely within the range of 0.035 pA to 0.0525 pA, respectively, assuming I_{RyR} at 1mM of SR Ca to be $I_{RyR,1mM}$ = 0.35 pA (as in (Stern et al., 2013)). Thus, our chosen critical spark amplitude of 0.175 pA is reasonable for spark termination time point, reflecting only 2 or 3 remaining open RyR channels (of 144 total in our SAN cell model). As the SR continues to be further depleted of Ca, these few open channels cannot support any longer CICR within the CRU, and spark undergoes a sharp termination phase transition that is also in line with our numerical simulations of spark dynamics (Figs 1 and 3 in (Maltsev et al., 2017a)). It is important to note that the spark termination mechanism does not include any intrinsic time-dependent inactivation, but simply reflects the drop of local Ca gradient over the JSR to the critical point that cannot sustain CICR among RyRs within the CRU (Laver et al., 2013; Stern et al., 2013; Maltsev et al., 2017a)).

3.8. Ca buffering

Cytosolic Ca is buffered by calmodulin (0.045 mM) throughout the cell: submembrane voxels, ring voxels, and the core. Each JSR features Ca buffering with calsequestrin (30 mM).

3.9. Summary of equations of local Ca dynamics

***In a submembrane voxel**:*

$$\frac{\partial Ca_{cyt,sub}}{\partial t} = D_{cyt}\nabla^2 Ca_{cyt,sub} - j_{cyt\_sub\_to\_ring} + (I_{spark}/N_{voxels\_in\_dyad} - i_{Ca})/(2\cdot F\cdot v_{cyt,sub}) - j_{CM} \quad (5)$$

I_{spark} in voxels outside dyadic space is absent. Each CRU releases Ca (given by I_{spark}) into its dyadic space. I_{spark} is evenly distributed among submembrane voxels of the dyadic space ($N_{voxels\_in\_dyad} = 9$). I_{spark} is given in Equation 3 and it is positive, i.e. increasing [Ca] in the submembrane voxel. i_{Ca} is the sum of local Ca transmembrane currents (described in details below in Electrophysiology section) via the membrane patch facing this submembrane voxel:

$$i_{Ca} = i_{CaL} + i_{CaT} + i_{bCa} - 2 \cdot i_{NCX}$$

I_{CaL} is included in this equation only for submembrane voxels facing a CRU (I_{CaL} is injected into the 9 subspace voxels of the respective dyadic space) . The local Ca currents i_{CaL}, i_{CaT}, i_{bCa} have inward direction and (by convention) are defined as negative. Therefore, the minus sign before i_{Ca} in Equation 5 ensures positive change in [Ca] in the submembrane voxel by respective Ca influx. During diastole local i_{NCX} also flows inwardly, but NCX exchanges 1 Ca ion to 3 Na ions. Hence, the inward i_{NCX} generates a Ca efflux. That is why it has a different sign.

In a voxel of ring layer:

$$\frac{\partial Ca_{cyt,ring}}{\partial t} = D_{cyt}\nabla^2 Ca_{cyt,ring} - j_{up,ring}\frac{v_{\mathrm{FSR,ring}}}{v_{\mathrm{cyt,ring}}} + \sum j_{cyt\_sub\_ring}\ \frac{v_{cyt.sub}}{v_{cyt,ring}} - j_{cyt\_ring\_to\_core} - j_{CM} \quad (6)$$

$\sum j_{cyt\_sub\_ring}$ is the sum of diffusion fluxes from neighboring smaller submembrane voxels

$$\frac{\partial Ca_{FSR,ring}}{\partial t} = D_{FSR}\nabla^2 Ca_{FSR,ring} + j_{up,ring} - j_{FSR\_ring\_to\_JSR} - j_{FSR\_ring\_to\_core} \quad (7)$$

The SERCA uptake flux j_{up} is given by Equation 1.

In a given JSR:

$$\frac{\partial Ca_{JSR}}{\partial t} = \sum j_{FSR\_ring\_to\_JSR}\frac{v_{ring,cyt}}{v_{JSR}} - I_{spark}/(2 \cdot F \cdot v_{JSR}) - j_{CQ} \quad (8)$$

where I_{spark} is given by Equation 3.

$\sum j_{FSR\_ring\_to\_JSR}$ is the sum of diffusion fluxes between JSR and respective FSR parts of the neighboring ring voxels. j_{CQ} is Ca flux of Ca buffering by calsequestrin:

$$j_{CQ} = CQ_{tot} \cdot \partial f_{CQ} / \partial t \qquad (9)$$

$$df_{CQ}/dt = k_{fCQ} \cdot Ca_{jSR} \cdot (1 - f_{CQ}) - k_{bCQ} \cdot f_{CQ}(t) \qquad (10)$$

In the core:

$$\frac{\partial Ca_{cyt,core}}{\partial t} = \sum j_{cyt\_ring\_to\_core} \frac{v_{cyt,ring}}{v_{cyt,core}} - j_{up,core} \frac{v_{\mathrm{FSR,core}}}{v_{\mathrm{cyt,core}}} - j_{CM} \qquad (11)$$

$$\frac{\partial Ca_{FSR,core}}{\partial t} = \sum j_{FSR\_ring\_to\_core} \frac{v_{FSR,ring}}{v_{FSR,core}} + j_{up,core} \qquad (12)$$

where $\sum j_{cyt\_ring\_to\_core}$ and $\sum j_{FSR\_ring\_to\_core}$ are the respective sums of diffusion fluxes in cytosol and FSR of all ring voxels.

In any cytoplasmic voxel (subspace, ring, and the core):

j_{CM} is Ca flux of Ca buffering by calmodulin:

$$j_{CM} = CM_{tot} \cdot \partial f_{CM} / \partial t \qquad (13)$$

$$\partial f_{CM} / \partial t = k_{fCM} \cdot Ca_{cyt} \cdot (1 - f_{CMs}) - k_{bCM} \cdot f_{CM}(x,y,t) \qquad (14)$$

4. ELECTROPHYSIOLOGY

Electrophysiological formulations for cell membrane currents are adapted from (Maltsev and Lakatta, 2009). Major changes of the model include introduction of local Ca currents and modulation of local currents by local Ca. To introduce local currents and local modulation by Ca, the cell membrane is partitioned into small patches, with each patch facing its respective subspace voxel. We also omitted sustained inward current I_{st} and background Na current I_{bNa} because thus far the molecular identities for these currents have not been found and these currents are likely produced by NCX or other currents

(Lakatta et al., 2010). We adopted I_{NCX} density and Ca-dependent I_{CaL} inactivation for more realistic modulation by much higher local Ca concentrations under the cell membrane predicted by our local Ca control models in the present study (Fig. A1) and previous models (Maltsev et al., 2011; Maltsev et al., 2013; Stern et al., 2014; Maltsev et al., 2017b) reaching >10 μM vs. common pool models (Kurata et al., 2002; Maltsev and Lakatta, 2009) predicting [Ca] in subspace only in sub-μM range in a bulk "subspace" compartment during diastole and 1-2 μM during Ca transient peak.

4.1 Fixed ion concentrations, mM

$Ca_o = 2$: Extracellular Ca concentration.

$K_o = 5.4$: Extracellular K concentration.

$K_i = 140$: Intracellular K concentration.

$Na_o = 140$: Extracellular Na concentration.

$Na_i = 10$: Intracellular Na concentration.

4.2. The Nernst equation and electric potentials, mV

$E_{Na} = E_T \cdot \ln(Na_o/Na_i)$: Equilibrium potential for Na

$E_K = E_T \cdot ln(K_o/K_i)$: Equilibrium potential for K

$E_{Ks} = E_T \cdot ln[(K_o + 0.12 \cdot Na_o)/(K_i + 0.12 \cdot Na_i)]$: Reversal potential of I_{Ks}

Where E_T is "*RT/F*" factor = 26.72655 mV at 37˚C,

$E_{CaL} = 45$: Apparent reversal potential of I_{CaL}

$E_{CaT} = 45$: Apparent reversal potential of I_{CaT}

4.3. Membrane potential, V_m

Net membrane current determines time derivative of the membrane potential.

$$dV_m/dt = -(I_{CaL} + I_{CaT} + I_{Kr} + I_{Ks} + I_{to} + I_{sus} + I_f + I_{NaK} + I_{bCa} + I_{NCX})/C_m$$

4.4. Formulation of cell membrane ion currents

Kinetics of ion currents are described by gating variables (described below) in respective differential equations

$$dy_i/dt = (y_{i,\infty} - y)/\tau_{yi}$$

$$(y_i = d_L,\ f_L,\ f_{Ca},\ d_T,\ f_T,\ p_{aF},\ p_{aS},\ p_{i\_},\ n,\ q,\ r,\ y)$$

τ_{yi}: time constant for a gating variable y_i.

α_{yi} and β_{yi}: opening and closing rates for channel gating.

$y_{i,\infty}$: steady-state curve for a gating variable y_i.

L-type Ca current *(I_{CaL})*

The whole cell I_{CaL} is calculated as a sum of local currents $i_{CaL,i}$ in each dyadic space.

$$I_{CaL} = \sum_{i \in CRU} i_{CaL,i}$$

This reflects reports that LCCs are colocalized with RyRs (Christel et al., 2012). Thus, the whole cell maximum I_{CaL} conductance (g_{CaL}) is distributed locally and equally among dyadic spaces:

$$g_{CaL,i} = g_{CaL}/N_{CRU}$$

The respective local $i_{CaL,i}$ in each CRU is calculated based on formulations of Kurata et al. (Kurata et al., 2002) and subsequent modifications in our common pool models (Maltsev and Lakatta, 2009, 2010, 2013), but now its Ca-dependent inactivation is determined by local subspace [Ca] ($Ca_{sub,i}$):

$$i_{CaL,i} = C_m \cdot g_{CaL,i} \cdot (V_m - E_{CaL}) \cdot d_L \cdot f_L \cdot f_{Ca,i}$$

$$d_{L,\infty} = 1/\{1 + exp[-(V_m - V_{d1/2})/6]\}$$

$$f_{L,\infty} = 1/\{1 + exp[(V_m + 35)/7.3]\}$$

$$\alpha_{dL} = -0.02839 \cdot (V_m + 35)/\{exp[-(V_m + 35)/2.5] - 1\} - 0.0849 \cdot V_m / [exp(-V_m/4.8) - 1]$$

$$\beta_{dL} = 0.01143 \cdot (V_m - 5)/\{exp[(V_m - 5)/2.5] - 1\}$$

$$\tau_{dL} = 1/(\alpha_{dL} + \beta_{dL})$$

$$\tau_{fL} = k\_tau\_fL \cdot (257.1 \cdot exp\{-[(V_m + 32.5)/13.9]^2\} + 44.3)$$

$$f_{Ca,\infty} = K_{mfCa} / (K_{mfCa} + Ca_{sub,i})$$

$$\tau_{fCa} = f_{Ca,\infty} / \alpha_{fCa}$$

Ca-dependent I_{CaL} inactivation is described by parameters K_{mfCa} and α_{fCa}. With K_{mfCa} of 0.35 μM in previous common pool models, our local Ca model of SAN cell did not work (not enough I_{CaL} was available to generate normal APs), because I_{CaL} inactivation was too sensitive to Ca and a major part of I_{CaL} was inactivated in diastole by diastolic LCRs whose amplitudes reach tens and hundreds of μM. Thus, we adopt Ca-dependent inactivation of I_{CaL} for more realistic modulation by much higher local Ca concentrations by setting K_{mfCa} to 30 μM.

We set the midpoint of I_{CaL} activation $V_{d1/2}$ to -6.6 mV as in SAN cell models of Wilders et al. (Wilders et al., 1991) and Dokos et al. (Dokos et al., 1996). This value of $V_{d1/2}$ is relatively high with respect to other SAN cell models and therefore was considered in our study to simulate I_{CaL} generated by $Ca_v1.2$, the cardiac isoform of LCC. It was used in all our simulations, except the two last Results sections where we studied effects of inclusion of $Ca_v1.3$ into I_{CaL} . Both isoforms $Ca_v1.2$ and $Ca_v1.3$, are colocalized with RyRs (Christel et al., 2012), but $Ca_v1.3$ has a lower (more hyperpolarized) voltage activation threshold. Therefore we simulated I_{CaL} generated by $Ca_v1.3$ using the same formulations above, but $V_{d1/2}$ was set to -13.5 mV. The resultant $V_{d1/2}$ shift increased $d_{L,\infty}$ of $Ca_v1.3$ within the range of diastolic depolarization by a factor of ~3, generating a much larger current and stronger recruitment

of CRUs to fire during diastolic depolarization. We performed a full-scale sensitivity analysis varying percentage of $Ca_v1.3$ in g_{CaL} from 0 to 100%, with total conductance g_{CaL} of $Ca_v1.2$ and $Ca_v1.3$ remaining constant ($gCa_v1.2 + gCa_v1.3 = g_{CaL}$ = 0.464 nS/pF = const).

T-type Ca current *(I_{CaT})*

It is based on formulations of Demir et al.(Demir et al., 1994) and modified by Kurata et al.(Kurata et al., 2002).

$$I_{CaT} = C_m \cdot g_{CaT,max} \cdot (V_m - E_{CaT}) \cdot d_T \cdot f_T$$

$$d_{T,\infty} = 1/\{1 + exp[-(V_m + 26.3)/6.0]\}$$

$$f_{T,\infty} = 1/\{1 + exp[(V_m + 61.7)/5.6]\}$$

$$\tau_{dT} = 1/\{1.068 \cdot exp[(V_m + 26.3)/30] + 1.068 \cdot exp[-(V_m + 26.3)/30]\}$$

$$\tau_{fT} = 1/\{0.0153 \cdot exp[-(V_m + 61.7)/83.3] + 0.015 \cdot exp[(V_m + 61.7)/15.38]\}$$

The whole cell I_{CaT} was evenly distributed over cell membrane patches to generate respective homogeneous Ca influx. In each submembrane *i-th* voxel $I_{CaT,i} = I_{CaT}/N_{voxels}$

Rapidly activating delayed rectifier K^+ current (I_{Kr})

It is based on formulations of Zhang et al. (Zhang et al., 2000), further modified by Kurata et al. (Kurata et al., 2002).

$$I_{Kr} = C_m \cdot g_{Kr,max} \cdot (V_m - E_K) \cdot (0.6 \cdot p_{aF} + 0.4 \cdot p_{aS}) \cdot p_i$$

$$p_{a,\infty} = 1/\{1 + exp[-(V_m + 23.2)/10.6]\}$$

$$p_{i,\infty} = 1/\{1 + exp[(V_m + 28.6)/17.1]\}$$

$$\tau_{paF} = k\_tau\_IKr \cdot 0.84655354/[0.0372 \cdot exp(V_m/15.9) + 0.00096 \cdot exp(-V_m/22.5)]$$

$$\tau_{paS} = k\_tau\_IKr \cdot 0.84655354/[0.0042 \cdot exp(V_m/17.0) + 0.00015 \cdot exp(-V_m/21.6)]$$

$$\tau_{pi} = 1/[0.1 \cdot exp(-V_m/54.645) + 0.656 \cdot exp(V_m/106.157)]$$

Slowly activating delayed rectifier K^+ current (I_{Ks})

It is based on formulations of Zhang et al. (Zhang et al., 2000).

$$I_{Ks} = C_m \cdot g_{Ks,max} \cdot (V_m - E_{Ks}) \cdot n^2$$

$$\alpha_n = 0.014/\{1 + exp[-(V_m - 40)/9]\}$$

$$\beta_n = 0.001 \cdot exp(-V_m/45)$$

$$n_\infty = \alpha_n/(\alpha_n + \beta_n)$$

$$\tau_n = 1/(\alpha_n + \beta_n)$$

4-aminopyridine-sensitive currents ($I_{4AP} = I_{to} + I_{sus}$)

It is based on formulations of Zhang et al. (Zhang et al., 2000).

$$I_{to} = C_m \cdot g_{to,max} \cdot (V_m - E_K) \cdot q \cdot r$$

$$I_{sus} = C_m \cdot g_{sus,max} \cdot (V_m - E_K) \cdot r$$

$$q_\infty = 1/\{1 + exp[(V_m + 49)/13]\}$$

$$r_\infty = 1/\{1 + exp[-(V_m - 19.3)/15]\}$$

$$\tau_q = 39.102/\{0.57 \cdot exp[-0.08 \cdot (V_m + 44)] + 0.065 \cdot exp[0.1 \cdot (V_m + 45.93)]\} + 6.06$$

$$\tau_r = 14.40516/\{1.037 \cdot exp[0.09 \cdot (V_m + 30.61)] + 0.369 \cdot exp[-0.12 \cdot (V_m + 23.84)]\} + 2.75352$$

Hyperpolarization-activated, "funny" current (I_f)

It is based on formulations of Wilders et al.(Wilders et al., 1991) and Kurata et al.(Kurata et al., 2002).

$$I_f = I_{fNa} + I_{fK}$$

$$y_\infty = 1/\{1 + exp[(V_m - V_{If,1/2})/13.5]\}$$

$$\tau_y = 0.7166529/\{exp[-(V_m + 386.9)/45.302] + exp[(V_m - 73.08)/19.231]\}$$

$$I_{fNa} = C_m \cdot 0.3833 \cdot g_{If,max} \cdot (V_m - E_{Na}) \cdot y^2$$

$$I_{fK} = C_m \cdot 0.6167 \cdot g_{If,max} \cdot (V_m - E_K) \cdot y^2$$

Na^+-K^+ pump current (I_{NaK})

It is based on formulations of Kurata et al.(Kurata et al., 2002), which were in turn based on the experimental work of Sakai et al.(Sakai et al., 1996) for rabbit SAN cell.

$$I_{NaK} = C_m \cdot I_{NaK,max} \cdot \{1+(K_{mKp}/K_o)^{1.2}\}^{-1} \cdot \{1+(K_{mNap}/Na_i)^{1.3}\}^{-1} \cdot \{1+exp[-(V_m - E_{Na}+120)/30]\}^{-1}$$

Ca- background current (I_{bCa})

$$I_{bCa} = C_m \cdot g_{bCa} \cdot (V_m - E_{CaL})$$

The whole cell I_{bCa} was evenly distributed over cell membrane to generate respective homogeneous Ca influx. In each submembrane *i-th* voxel $I_{bCa,i} = I_{bCa}/N_{voxels}$

Na-Ca exchanger current (I_{NCX})

It is based on original formulations from Dokos et al. (Dokos et al., 1996). I_{NCX} is modulated by local Ca and therefore the whole cell I_{NCX} was calculated as a sum of local currents $I_{NCX,i}$ in respective membrane patches facing each submembrane voxel. Thus,

$$I_{NCX} = \sum_{i=1}^{Nvoxels} I_{NCX,i}$$

For membrane voltage V_m in each *i*-th membrane patch with subspace $Ca_{sub,i}$, the respective local NCX current ($I_{NCX,i}$) was calculated as follows:

$$I_{NCX,i} = C_m \cdot k_{NCX} \cdot (k_{21} \cdot x_2 - k_{12} \cdot x_1) / (x_1 + x_2 + x_3 + x_4)$$

$$d_o = 1+(Ca_o/K_{co})\cdot\{1+\exp(Q_{co}\cdot V_m/E_T)\}+(Na_o/K_{1no})\cdot\{1+(Na_o/K_{2no})\cdot(1+Na_o/K_{3no})\}$$

$$k_{43} = Na_i/(K_{3ni} + Na_i)$$

$$k_{41} = \exp[-Q_n\cdot V_m/(2E_T)]$$

$$k_{34} = Na_o/(K_{3no}+Na_o)$$

$$k_{21} = (Ca_o/K_{co})\cdot\exp(Q_{co}\cdot V_m/E_T)/d_o$$

$$k_{23} = (Na_o/K_{1no})\cdot(Na_o/K_{2no})\cdot(1+Na_o/K_{3no})\cdot \exp[-Q_n\cdot V_m/(2E_T)]/d_o$$

$$k_{32} = \exp[Q_n\cdot V_m/(2E_T)]$$

$$x_1 = k_{34} \cdot k_{41} \cdot (k_{23} + k_{21}) + k_{21} \cdot k_{32} \cdot (k_{43} + k_{41})$$

$$d_i = 1+(Ca_{sub,i}/K_{ci})\cdot\{1+\exp(-Q_{ci}\cdot V_m/E_T)+Na_i/K_{cni}\}+(Na_i/K_{1ni})\cdot\{1+(Na_i/K_{2ni})\cdot(1+Na_i/K_{3ni})\}$$

$$k_{12} = (Ca_{sub,i}/K_{ci})\cdot\exp(-Q_{ci}\cdot V_m/E_T)/d_i$$

$$k_{14} = (Na_i/K_{1ni})\cdot(Na_i/K_{2ni})\cdot(1 +Na_i/K_{3ni})\cdot \exp[Q_n\cdot V_m/(2E_T)]/d_i$$

$$x_2 = k_{43}\cdot k_{32} \cdot(k_{14} + k_{12}) + k_{41}\cdot k_{12} \cdot k_{34} + k_{32})$$

$$x_3 = k_{43} \cdot k_{14} \cdot (k_{23} + k_{21}) + k_{12} \cdot k_{23}\cdot(k_{43} + k_{41})$$

$$x_4 = k_{34} \cdot k_{23} \cdot (k_{14} + k_{12}) + k_{21} \cdot k_{14}\cdot(k_{34}+ k_{32})$$

5. Initial values

Initial values for electrophysiology were as follows:

-57.96393469	V_m	Membrane potential, mV
0.000584546	d_L	I_{CaL} voltage-dependent activation
0.86238125	f_L	I_{CaL} voltage-dependent inactivation
0.71139592	f_{Ca}	I_{CaL} Ca-dependent inactivation (local)
0.144755091	p_{aF}	I_{Kr} fast activation

0.453100577	p_{aS}	I_{Kr} slow activation
0.849409822	$p_{i\_}$	I_{Kr} inactivation
0.026460041	n	I_{Ks} activation
0.113643187	y	I_f activation
0.005043934	d_T	I_{CaT} activation
0.420757825	f_T	I_{CaT} inactivation
0.694241314	q	I_{to} inactivation
0.005581317	r	I_{to} and I_{sus} activation

Initial values for Ca dynamics were as follows:

200 nM	[Ca] in cytosol
1 mM	[Ca] in FSR
0.8 mM	Ca concentration in JSR
0.0787	Fractional occupancy of calmodulin by Ca in cytoplasm
0.6	Fractional occupancy of calsequestrin by Ca in JSR

All CRUs are set in the closed state

6. Summary of model parameters

Fixed ion concentrations

Ca_o=2 mM: Extracellular [Ca]

K_o=5.4 mM: Extracellular [K]

Na_o=140 mM: Extracellular [Na]

K_i=140 mM: Intracellular [K]

Na_i=10 mM: Intracellular [Na]

Membrane currents

E_{CaL} = 45 mV: Apparent reversal potential of I_{CaL}

g_{CaL} = 0.464 nS/pF: Conductance of I_{CaL}

K_{mfCa} = 0.03 mM: Dissociation constant of Ca -dependent I_{CaL} inactivation

$beta_{fCa}$ = 60 $mM^{-1} \cdot ms^{-1}$: Ca association rate constant for I_{CaL}.

$alfa_{fCa}$ = 0.021 ms^{-1}: Ca dissociation rate constant for I_{CaL}

k_tau_fL = 0.5: Scaling factor for *tau_fL* used to tune the model

E_{CaT} = 45: Apparent reversal potential of I_{CaT}, mV

g_{CaT} = 0.1832 nS/pF: Conductance of I_{CaT}

g_{If} = 0.105 nS/pF: Conductance of I_f

$V_{If,1/2}$ = -64: half activation voltage of I_f, mV

g_{Kr} = 0.05679781 nS/pF: Conductance of delayed rectifier K current rapid component

k_ tau_IKr = 0.3: scaling factor for *tau_paF* and *tau_paS* used to tune the model

g_{Ks} = 0.0259 nS/pF: Conductance of delayed rectifier K current slow component

g_{to} = 0.252 nS/pF: Conductance of 4-aminopyridine sensitive transient K^+ current

g_{sus} = 0.02 nS/pF: Conductance of 4-aminopyridine sensitive sustained K^+ current

I_{NaKmax} = 1.44 pA/pF: Maximum Na^+/K^+ pump current

K_{mKp} = 1.4 mM: Half-maximal K_o for I_{NaK}.

K_{mNap} = 14 mM: Half-maximal Na_i for I_{NaK}.

g_{bCa} = 0.003 nS/pF: Conductance of background Ca current,

k_{NCX} = 48.75 pA/pF: Maximumal amplitude of I_{NCX}

Dissociation constants for NCX

K_{1ni} = 395.3 mM: intracellular Na binding to first site on NCX

K_{2ni} = 2.289 mM: intracellular Na binding to second site on NCX

K_{3ni} = 26.44 mM: intracellular Na binding to third site on NCX

K_{1no} = 1628 mM: extracellular Na binding to first site on NCX

K_{2no} = 561.4 mM: extracellular Na binding to second site on NCX

K_{3no} = 4.663 mM: extracellular Na binding to third site on NCX

K_{ci} = 0.0207 mM: intracellular Ca binding to NCX transporter

K_{co} = 3.663 mM: extracellular Ca binding to NCX transporter

K_{cni} = 26.44 mM: intracellular Na and Ca simultaneous binding to NCX

NCX fractional charge movement

Q_{ci}= 0.1369: intracellular Ca occlusion reaction of NCX

Q_{co}=0: extracellular Ca occlusion reaction of NCX

Q_{n}= 0.4315: Na occlusion reactions of NCX

Ca buffering

k_{bCM} = 0.542 ms^{-1}: Ca dissociation constant for calmodulin

k_{fCM} = 227.7 $mM^{-1} \cdot ms^{-1}$: Ca association constant for calmodulin

k_{bCQ} = 0.445 ms^{-1}: Ca dissociation constant for calsequestrin

k_{fCQ} = 0.534 $mM^{-1} \cdot ms^{-1}$: Ca association constant for calsequestrin

CQ_{tot} = 30 mM: Total calsequestrin concentration

CM_{tot} = 0.045 mM: Total calmodulin concentration

SR Ca ATPase function

K_{mf} = 0.000246 mM: the cytosolic side K_d of SR Ca pump

K_{mr} = 1.7 mM: the lumenal side K_d of SR Ca pump

H = 1.787: cooperativity of SR Ca pump

P_{up} = 0.014 mM/ms: Maximal rate of Ca uptake by SR Ca pump

CRU (Ca release and JSR)

CRU_Casens = 0.00015 mM: sensitivity of Ca release to Casub

CRU_ProbConst = 0.00027 ms^{-1}: CRU open probability rate at Casub=CRU_Casens

CRU_ProbPower = 3: Cooperativity of CRU activation by Casub

CaJSR_spark_activation = 0.3 mM: critical JSR Ca loading to generate a spark (CRU can open)

Ispark_Termination = 0.175 pA: critical minimum I_{spark} triggering spark termination (CRU closes)

Ispark_activation_tau_ms = 80 ms: Time constant of spark activation (a)

Iryr_at_1mM_CaJSR = 0.35 pA: unitary RyR current at 1 mM delta Ca

RyR_to_RyR_distance_um = 0.03 μm: RyR crystal grid size in JSR

JSR_depth_um = 0.06 μm: JSR depth

JSR_Xsize_um = 0.36 μm: JSR size in x

JSR_Ysize_um = 0.36 μm: JSR size in y

JSR_to_JSR_X_um = 1.44 μm: JSR crystal grid size in x

JSR_to_JSR_Y_um = 1.44 μm: JSR crystal grid size in y

Cell geometry, compartments, and voxels

L_{cell} = 53.28 μm: Cell length

r_{cell} = 3.437747 μm: Cell radius

C_m = 19.80142 pF: membrane electrical capacitance of our cell model with 0.0172059397937 pF/μm^2 specific membrane capacitance calculated from 2002 Kurata et al. model (Kurata et al., 2002) for its 32 pF cylinder cell of 70 μm length and 4 μm radius.

0.12 μm: the grid size

0.12 μm: Submembrane voxel size in *x*

0.12 μm: Submembrane voxel size in *y*

0.02 μm: Submembrane voxel size depth

0.36 μm: Ring voxel size in *x*

0.36 μm: Ring voxel size in *y*

0.8 μm: Ring voxel depth

0.46: Fractional volume of cytosol

0.035: Fractional volume of FSR

Ca diffusion

Dcyt = 0.35 μm^2/ms: Diffusion coefficient of free Ca in cytosol

D_{FSR} = 0.06 μm^2/ms: Diffusion coefficient of free Ca in FSR

7. g_{CaL} sensitivity analysis

For square lattice and uniform random distributions of CRUs we performed sensitivity analysis for g_{CaL} from its basal value of 0.464 nS/pF (100%) down to 0.2552 nS/pF (55%) shown by

magenta band in the main text Fig. 7 A with a step of 0.0232 pA/pF (5%). The original data of this analysis in the form of V_m time series are given Fig. A2 for each CRU distribution.

8. Simulations of βAR stimulation effect

Effect of βAR stimulation was modelled essentially as we previously reported (Maltsev and Lakatta, 2010) by increasing I_{CaL}, I_{Kr}, I_f, and Ca uptake rate by FSR via SERCA pumping. Specifically whole cell maximum I_{CaL} conductance g_{CaL} was increased by a factor of 1.75 from 0.464 to 0.812 nS/pF; whole cell maximum I_{Kr} conductance g_{Kr} was increased by a factor of 1.5 from 0.05679781 to 0.085196715 nS/pF; the midpoint of I_f activation curve was shifted to more depolarized potential by 7.8 mV from -64 mV to -56.2 mV; and the maximum Ca uptake rate P_{up} was increased by a factor of 2 from 14 mM/s to 28 mM/s. The original data in the form of intervalograms are given Fig. A3 for each CRU distribution in basal state and in during βAR stimulation

9. **Model Integration**

The model code was written in Delphi Language (Delphi 10.4) and was computed with a fixed time tick of 0.0075 ms on a workstation running Windows 10 with Intel® Xeon® W-2145 CPU @3.7GHz processor. The basic model code of the model is provided as a single Delphi file (SANC.dpr) that can be freely used as a new mainframe to further investigate SAN function with respect to local Ca changes and Ca channel isoforms $Ca_v1.2$ and $Ca_v1.3$ interacting locally with RyRs.

References

Asghari, P., D.R. Scriven, M. Ng, P. Panwar, K.C. Chou, F. van Petegem, and E.D. Moore. 2020. Cardiac ryanodine receptor distribution is dynamic and changed by auxiliary proteins and post-translational modification. *Elife*. 9:

Baig, S.M., A. Koschak, A. Lieb, M. Gebhart, C. Dafinger, G. Nurnberg, A. Ali, I. Ahmad, M.J. Sinnegger-Brauns, N. Brandt, J. Engel, M.E. Mangoni, M. Farooq, H.U. Khan, P. Nurnberg, J. Striessnig, and H.J. Bolz. 2011. Loss of Ca(v)1.3 (CACNA1D) function in a human channelopathy with bradycardia and congenital deafness. *Nat Neurosci*. 14:77-84.

Bogdanov, K.Y., T.M. Vinogradova, and E.G. Lakatta. 2001. Sinoatrial nodal cell ryanodine receptor and Na^{+}-Ca^{2+} exchanger: molecular partners in pacemaker regulation. *Circ Res*. 88:1254-1258.

Brennan, J.A., Q. Chen, A. Gams, J. Dyavanapalli, D. Mendelowitz, W. Peng, and I.R. Efimov. 2020. Evidence of Superior and Inferior Sinoatrial Nodes in the Mammalian Heart. *JACC Clin Electrophysiol*. 6:1827-1840.

Bychkov, R., M. Juhaszova, K. Tsutsui, C. Coletta, M.D. Stern, V.A. Maltsev, and E.G. Lakatta. 2020. Synchronized cardiac impulses emerge from multi-scale, heterogeneous local calcium signals within and among cells of heart pacemaker tissue. *JACC Clin Electrophysiol*. 6:907-931.

Chen-Izu, Y., C.W. Ward, W. Stark, Jr., T. Banyasz, M.P. Sumandea, C.W. Balke, L.T. Izu, and X.H. Wehrens. 2007. Phosphorylation of RyR2 and shortening of RyR2 cluster spacing in spontaneously hypertensive rat with heart failure. *Am J Physiol Heart Circ Physiol*. 293:H2409-2417.

1321 Chen, B., Y. Wu, P.J. Mohler, M.E. Anderson, and L.S. Song. 2009. Local control of Ca^{2+}-
1322 induced Ca^{2+} release in mouse sinoatrial node cells. *J Mol Cell Cardiol*. 47:706-715.
1323 Cheng, H., W.J. Lederer, and M.B. Cannell. 1993. Calcium sparks: elementary events underlying
1324 excitation-contraction coupling in heart muscle. *Science*. 262:740-744.
1325 Christel, C.J., N. Cardona, P. Mesirca, S. Herrmann, F. Hofmann, J. Striessnig, A. Ludwig, M.E.
1326 Mangoni, and A. Lee. 2012. Distinct localization and modulation of Cav1.2 and Cav1.3
1327 L-type Ca2+ channels in mouse sinoatrial node. *J Physiol*. 590:6327-6342.
1328 Clancy, C.E., and L.F. Santana. 2020. Evolving Discovery of the Origin of the Heartbeat: A New
1329 Perspective on Sinus Rhythm. *JACC Clin Electrophysiol*. 6:932-934.
1330 Demir, S.S., J.W. Clark, C.R. Murphey, and W.R. Giles. 1994. A mathematical model of a rabbit
1331 sinoatrial node cell. *Am J Physiol*. 266:C832-852.
1332 DiFrancesco, D., and C. Tromba. 1988. Inhibition of the hyperpolarization-activated current (if)
1333 induced by acetylcholine in rabbit sino-atrial node myocytes. *J Physiol*. 405:477-491.
1334 Dokos, S., B. Celler, and N. Lovell. 1996. Ion currents underlying sinoatrial node pacemaker
1335 activity: a new single cell mathematical model. *J Theor Biol*. 181:245-272.
1336 Fenske, S., K. Hennis, R.D. Rotzer, V.F. Brox, E. Becirovic, A. Scharr, C. Gruner, T. Ziegler, V.
1337 Mehlfeld, J. Brennan, I.R. Efimov, A.G. Pauza, M. Moser, C.T. Wotjak, C. Kupatt, R.
1338 Gonner, R. Zhang, H. Zhang, X. Zong, M. Biel, and C. Wahl-Schott. 2020. cAMP-
1339 dependent regulation of HCN4 controls the tonic entrainment process in sinoatrial node
1340 pacemaker cells. *Nat Commun*. 11:5555.
1341 Gratz, D., B. Onal, A. Dalic, and T.J. Hund. 2018. Synchronization of pacemaking in the
1342 sinoatrial node: a mathematical modeling study. *Front Physics*. 6:id.63.

Greiser, M., H.C. Joca, and W.J. Lederer. 2020. Pacemaker organization at the nanoscale: imaging of ryanodine receptors as clusters in single sinoatrial nodal cells. *Biophys J.* 116:380A.

Guarina, L., A.N. Moghbel, M.S. Pourhosseinzadeh, R.H. Cudmore, D. Sato, C.E. Clancy, and L.F. Santana. 2022. Biological noise is a key determinant of the reproducibility and adaptability of cardiac pacemaking and EC coupling. *J Gen Physiol*. 154:

Himeno, Y., N. Sarai, S. Matsuoka, and A. Noma. 2008. Ionic mechanisms underlying the positive chronotropy induced by beta1-adrenergic stimulation in guinea pig sinoatrial node cells: a simulation study. *J Physiol Sci*. 58:53-65.

Honjo, H., M.R. Boyett, I. Kodama, and J. Toyama. 1996. Correlation between electrical activity and the size of rabbit sino-atrial node cells. *J Physiol*. 496 (Pt 3):795-808.

Huser, J., L.A. Blatter, and S.L. Lipsius. 2000. Intracellular Ca^{2+} release contributes to automaticity in cat atrial pacemaker cells. *J Physiol*. 524 Pt 2:415-422.

Imtiaz, M.S., P.Y. von der Weid, D.R. Laver, and D.F. van Helden. 2010. SR Ca^{2+} store refill--a key factor in cardiac pacemaking. *J Mol Cell Cardiol*. 49:412-426.

Inada, S., H. Zhang, J.O. Tellez, N. Shibata, K. Nakazawa, K. Kamiya, I. Kodama, K. Mitsui, H. Dobrzynski, M.R. Boyett, and H. Honjo. 2014. Importance of gradients in membrane properties and electrical coupling in sinoatrial node pacing. *PLoS One*. 9:e94565.

Kim, M.S., A.V. Maltsev, O. Monfredi, L.A. Maltseva, A. Wirth, M.C. Florio, K. Tsutsui, D.R. Riordon, S.P. Parsons, S. Tagirova, B.D. Ziman, M.D. Stern, E.G. Lakatta, and V.A. Maltsev. 2018. Heterogeneity of calcium clock functions in dormant, dysrhythmically and rhythmically firing single pacemaker cells isolated from SA node. *Cell Calcium*. 74:168-179.

Kim, M.S., O. Monfredi, L.A. Maltseva, E.G. Lakatta, and V.A. Maltsev. 2021. beta-Adrenergic Stimulation Synchronizes a Broad Spectrum of Action Potential Firing Rates of Cardiac Pacemaker Cells toward a Higher Population Average. *Cells*. 10:

Kurata, Y., I. Hisatome, S. Imanishi, and T. Shibamoto. 2002. Dynamical description of sinoatrial node pacemaking: improved mathematical model for primary pacemaker cell. *Am J Physiol*. 283:H2074-2101.

Kurata, Y., I. Hisatome, and T. Shibamoto. 2012. Roles of Sarcoplasmic Reticulum Ca^{2+} Cycling and Na^{+}/Ca^{2+} Exchanger in Sinoatrial Node Pacemaking: insights from bifurcation analysis of mathematical models. *Am J Physiol Heart Circ Physiol*. 302:H2285-H2300.

Lakatta, E.G., V.A. Maltsev, and T.M. Vinogradova. 2010. A coupled SYSTEM of intracellular Ca^{2+} clocks and surface membrane voltage clocks controls the timekeeping mechanism of the heart's pacemaker. *Circ Res*. 106:659-673.

Laver, D.R., C.H. Kong, M.S. Imtiaz, and M.B. Cannell. 2013. Termination of calcium-induced calcium release by induction decay: an emergent property of stochastic channel gating and molecular scale architecture. *J Mol Cell Cardiol*. 54:98-100.

Li, K., Z. Chu, and X. Huang. 2018. Annihilation of the pacemaking activity in the sinoatrial node cell and tissue *AIP Advances*. 8:125319.

Louradour, J., O. Bortolotti, E. Torre, I. Bidaud, N. Lamb, A. Fernandez, J.Y. Le Guennec, M.E. Mangoni, and P. Mesirca. 2022. L-Type Cav1.3 Calcium Channels Are Required for Beta-Adrenergic Triggered Automaticity in Dormant Mouse Sinoatrial Pacemaker Cells. *Cells*. 11:

Lyashkov, A.E., J. Behar, E.G. Lakatta, Y. Yaniv, and V.A. Maltsev. 2018. Positive Feedback Mechanisms among Local Ca Releases, NCX, and ICaL Ignite Pacemaker Action Potentials. *Biophys J*. 114:1176-1189.

Lyashkov, A.E., M. Juhaszova, H. Dobrzynski, T.M. Vinogradova, V.A. Maltsev, O. Juhasz, H.A. Spurgeon, S.J. Sollott, and E.G. Lakatta. 2007. Calcium cycling protein density and functional importance to automaticity of isolated sinoatrial nodal cells are independent of cell size. *Circ Res*. 100:1723-1731

Lyashkov, A.E., T.M. Vinogradova, I. Zahanich, Y. Li, A. Younes, H.B. Nuss, H.A. Spurgeon, V.A. Maltsev, and E.G. Lakatta. 2009. Cholinergic receptor signaling modulates spontaneous firing of sinoatrial nodal cells via integrated effects on PKA-dependent Ca^{2+} cycling and I_{KACh}. *Am J Physiol Heart Circ Physiol*. 297:H949-H959.

Maltsev, A.V., V.A. Maltsev, M. Mikheev, L.A. Maltseva, S.G. Sirenko, E.G. Lakatta, and M.D. Stern. 2011. Synchronization of stochastic Ca^{2+} release units creates a rhythmic Ca^{2+} clock in cardiac pacemaker cells. *Biophys J*. 100:271-283.

Maltsev, A.V., V.A. Maltsev, and M.D. Stern. 2017a. Clusters of calcium release channels harness the Ising phase transition to confine their elementary intracellular signals. *Proc Natl Acad Sci U S A*. 114:7525–7530.

Maltsev, A.V., V.A. Maltsev, and M.D. Stern. 2017b. Stabilization of diastolic calcium signal via calcium pump regulation of complex local calcium releases and transient decay in a computational model of cardiac pacemaker cell with individual release channels. *PLoS Comput Biol*. 13:e1005675.

Maltsev, A.V., M.D. Stern, E.G. Lakatta, and V.A. Maltsev. 2022. Functional heterogeneity of cell populations increases robustness of pacemaker function in a numerical model of the sinoatrial node tissue. *Front Physiol*. 13:845634.

Maltsev, A.V., M.D. Stern, and V.A. Maltsev. 2019. Mechanisms of Calcium Leak from Cardiac Sarcoplasmic Reticulum Revealed by Statistical Mechanics. *Biophys J*. 116:2212-2223.

Maltsev, A.V., Y. Yaniv, M.D. Stern, E.G. Lakatta, and V.A. Maltsev. 2013. RyR-NCX-SERCA local crosstalk ensures pacemaker cell function at rest and during the fight-or-flight reflex. *Circ Res*. 113:e94-e100.

Maltsev, V.A., and E.G. Lakatta. 2009. Synergism of coupled subsarcolemmal Ca^{2+} clocks and sarcolemmal voltage clocks confers robust and flexible pacemaker function in a novel pacemaker cell model. *Am J Physiol Heart Circ Physiol*. 296:H594-H615.

Maltsev, V.A., and E.G. Lakatta. 2010. A novel quantitative explanation for autonomic modulation of cardiac pacemaker cell automaticity via a dynamic system of sarcolemmal and intracellular proteins. *Am J Physiol Heart Circ Physiol*. 298:H2010-H2023.

Maltsev, V.A., and E.G. Lakatta. 2013. Numerical models based on a minimal set of sarcolemmal electrogenic proteins and an intracellular Ca clock generate robust, flexible, and energy-efficient cardiac pacemaking. *J Mol Cell Cardiol*. 59:181-195.

Maltsev, V.A., A.V. Maltsev, M. Juhaszova, S. Sirenko, O. Monfredi, H. Shroff, A. York, S.J. Sollott, E.G. Lakatta, and M.D. Stern. 2016. Cardiac pacemaker cell function at a super-resolution scale of SIM: distribution of RyRs, calcium dynamics, and numerical modeling. *Biophys J*. 110:267A (Abstract).

Maltsev, V.A., Y. Yaniv, A.V. Maltsev, M.D. Stern, and E.G. Lakatta. 2014. Modern perspectives on numerical modeling of cardiac pacemaker cell. *J Pharmacol Sci*. 125:6-38.

McDonnell, M.D., and D. Abbott. 2009. What is stochastic resonance? Definitions, misconceptions, debates, and its relevance to biology. *PLoS Comput Biol*. 5:e1000348.

Mesirca, P., A.G. Torrente, and M.E. Mangoni. 2015. Functional role of voltage gated Ca^{2+} channels in heart automaticity. *Front Physiol*. 6:19.

Monfredi, O., K. Tsutsui, B.D. Ziman, M.D. Stern, E.G. Lakatta, and V.A. Maltsev. 2017. Electrophysiological heterogeneity of pacemaker cells in rabbit intercaval region, including SA node: insights from recording multiple ion currents in each cell. *Am J Physiol Heart Circ Physiol*. ajpheart 00253 02016.

Musa, H., M. Lei, H. Honjo, S.A. Jones, H. Dobrzynski, M.K. Lancaster, Y. Takagishi, Z. Henderson, I. Kodama, and M.R. Boyett. 2002. Heterogeneous expression of Ca^{2+} handling proteins in rabbit sinoatrial node. *J Histochem Cytochem*. 50:311-324.

Nivala, M., C.Y. Ko, M. Nivala, J.N. Weiss, and Z. Qu. 2012. Criticality in intracellular calcium signaling in cardiac myocytes. *Biophys J*. 102:2433-2442.

Oren, R.V., and C.E. Clancy. 2010. Determinants of heterogeneity, excitation and conduction in the sinoatrial node: a model study. *PLoS Comput Biol*. 6:e1001041.

Qu, Z., A. Garfinkel, J.N. Weiss, and M. Nivala. 2011. Multi-scale modeling in biology: how to bridge the gaps between scales? *Prog Biophys Mol Biol*. 107:21-31.

Rigg, L., B.M. Heath, Y. Cui, and D.A. Terrar. 2000. Localisation and functional significance of ryanodine receptors during beta-adrenoceptor stimulation in the guinea-pig sino-atrial node. *Cardiovasc Res*. 48:254-264.

Sakai, R., N. Hagiwara, N. Matsuda, H. Kassanuki, and S. Hosoda. 1996. Sodium--potassium pump current in rabbit sino-atrial node cells. *J Physiol*. 490 (Pt 1):51-62.

Severi, S., M. Fantini, L.A. Charawi, and D. DiFrancesco. 2012. An updated computational model of rabbit sinoatrial action potential to investigate the mechanisms of heart rate modulation. *J Physiol*. 590:4483-4499.

Shannon, T.R., F. Wang, J. Puglisi, C. Weber, and D.M. Bers. 2004. A mathematical treatment of integrated Ca dynamics within the ventricular myocyte. *Biophys J*. 87:3351-3371.

Stern, M.D. 1992. Theory of excitation-contraction coupling in cardiac muscle. *Biophys J*. 63:497-517.

Stern, M.D., L.A. Maltseva, M. Juhaszova, S.J. Sollott, E.G. Lakatta, and V.A. Maltsev. 2014. Hierarchical clustering of ryanodine receptors enables emergence of a calcium clock in sinoatrial node cells. *J Gen Physiol*. 143:577-604.

Stern, M.D., G. Pizarro, and E. Rios. 1997. Local control model of excitation-contraction coupling in skeletal muscle. *J Gen Physiol*. 110:415-440.

Stern, M.D., E. Rios, and V.A. Maltsev. 2013. Life and death of a cardiac calcium spark. *J Gen Physiol*. 142:257-274.

Ter Keurs, H.E., and P.A. Boyden. 2007. Calcium and arrhythmogenesis. *Physiol Rev*. 87:457-506.

Torrente, A.G., P. Mesirca, P. Neco, R. Rizzetto, S. Dubel, C. Barrere, M. Sinegger-Brauns, J. Striessnig, S. Richard, J. Nargeot, A.M. Gomez, and M.E. Mangoni. 2016. L-type Cav1.3 channels regulate ryanodine receptor-dependent Ca^{2+} release during sino-atrial node pacemaker activity. *Cardiovasc Res*. 109:451-461.

Tsutsui, K., M.C. Florio, A. Yang, A.N. Wirth, D. Yang, M.S. Kim, B.D. Ziman, R. Bychkov, O.J. Monfredi, V.A. Maltsev, and E.G. Lakatta. 2021. cAMP-Dependent Signaling Restores AP Firing in Dormant SA Node Cells via Enhancement of Surface Membrane Currents and Calcium Coupling. *Front Physiol*. 12:596832.

Tsutsui, K., O. Monfredi, and E.G. Lakatta. 2016. A general theory to explain heart rate and cardiac contractility changes with age. *Physiol Mini Reviews*. 9:9-25.

Tsutsui, K., O. Monfredi, S.G. Sirenko-Tagirova, L.A. Maltseva, R. Bychkov, M.S. Kim, B.D. Ziman, K.V. Tarasov, Y.S. Tarasova, J. Zhang, M. Wang, A.V. Maltsev, J.A. Brennan, I.R. Efimov, M.D. Stern, V.A. Maltsev, and E.G. Lakatta. 2018. A coupled-clock system drives the automaticity of human sinoatrial nodal pacemaker cells. *Sci Signal*. 11:eaap7608.

Veron, G., V.A. Maltsev, M.D. Stern, and A.V. Maltsev. 2021. Elementary intracellular signals are initiated by a transition of release channel system from a metastable state. *Arxiv*. https://arxiv.org/abs/2105.01340 (preprint):

Vinogradova, T.M., K.Y. Bogdanov, and E.G. Lakatta. 2002. beta-Adrenergic stimulation modulates ryanodine receptor Ca^{2+} release during diastolic depolarization to accelerate pacemaker activity in rabbit sinoatrial nodal cells. *Circ Res*. 90:73-79.

Vinogradova, T.M., D.X. Brochet, S. Sirenko, Y. Li, H. Spurgeon, and E.G. Lakatta. 2010. Sarcoplasmic reticulum Ca^{2+} pumping kinetics regulates timing of local Ca^{2+} releases and spontaneous beating rate of rabbit sinoatrial node pacemaker cells. *Circ Res*. 107:767-775.

Vinogradova, T.M., A.E. Lyashkov, W. Zhu, A.M. Ruknudin, S. Sirenko, D. Yang, S. Deo, M. Barlow, S. Johnson, J.L. Caffrey, Y.Y. Zhou, R.P. Xiao, H. Cheng, M.D. Stern, V.A.

Maltsev, and E.G. Lakatta. 2006. High basal protein kinase A-dependent phosphorylation drives rhythmic internal Ca^{2+} store oscillations and spontaneous beating of cardiac pacemaker cells. *Circ Res*. 98:505-514.

Weiss, J.N., and Z. Qu. 2020. The Sinus Node: Still Mysterious After All These Years. *JACC Clin Electrophysiol*. 6:1841-1843.

Wilders, R., H.J. Jongsma, and A.C. van Ginneken. 1991. Pacemaker activity of the rabbit sinoatrial node. A comparison of mathematical models. *Biophys J*. 60:1202-1216.

Yuan, X., L.N. Ratajczyk, F. Alvarado, H.H. Valdivia, A.V. Glukhov, and D. Lang. 2020. Hierarchical Pacemaker Clustering within the Rabbit Sinoatrial Node is Driven by Dynamic Interaction between the Components of the Coupled-Clock System. *Biophys J*. 118:345A (Abstract).

Zhang, H., A.V. Holden, I. Kodama, H. Honjo, M. Lei, T. Varghese, and M.R. Boyett. 2000. Mathematical models of action potentials in the periphery and center of the rabbit sinoatrial node. *Am J Physiol*. 279:H397-421.

Zhang, Y., J.L. Ocampo-Espindola, I.Z. Kiss, and A.E. Motter. 2021. Random heterogeneity outperforms design in network synchronization. *Proc Natl Acad Sci U S A*. 118:

Zhou, P., Y.T. Zhao, Y.B. Guo, S.M. Xu, S.H. Bai, E.G. Lakatta, H. Cheng, X.M. Hao, and S.Q. Wang. 2009. Beta-adrenergic signaling accelerates and synchronizes cardiac ryanodine receptor response to a single L-type Ca^{2+} channel. *Proc Natl Acad Sci U S A*. 106:18028-18033.

Zima, A.V., E. Bovo, D.M. Bers, and L.A. Blatter. 2010. Ca^{2+} spark-dependent and -independent sarcoplasmic reticulum Ca^{2+} leak in normal and failing rabbit ventricular myocytes. *J Physiol*. 588:4743-4757.

Zima, A.V., E. Picht, D.M. Bers, and L.A. Blatter. 2008. Termination of cardiac Ca^{2+} sparks: role of intra-SR [Ca^{2+}], release flux, and intra-SR Ca^{2+} diffusion. *Circ Res*. 103:e105-115.

Figure legends

Figure 1. Schematic illustration of approximation of local Ca dynamics in our updated CRU-based SAN cell model: CRUs are placed under the cell membrane (A). Three layers of voxels approximate intracellular Ca dynamics (shown not in scale): in cross-section (B) and longitudinal section (C). For more details see Appendix.

Figure 2.

Effect of Poisson clumping: Clusterization of CRUs and emergence of voids as disorder in CRU locations increases. Left panels: The cell cylinder surfaces "unwrapping" to squares with examples of distributions of RyR clusters under the cell membrane with varying degree of disorder used in our simulations of SAN cell function. 555 CRUs are distributed in each case. SD values of normal distributions used to perturb CRU locations from their perfect square lattice positions are shown in respective labels above each image. Right panels: Histograms of the respective distributions of nearest neighbor distances with their mean and SD values (in μm).

Figure 3. Disorder in CRU position shortens CL (i.e. increases AP firing rate). A: CL intervalograms for SAN cell models with various degrees of disorder in CRU positions. Inset

shows that CL correlates with the average nearest neighbor distance, that is shortens as disorder increases. B: Respective examples of simulated spontaneous APs.

Figure 4. Perturbing CRU positions around their original square lattice positions increases synchronization and recruitment of CRU to release Ca via locally propagating CICR, resulting in earlier activation of I_{NCX} and shorter AP firing cycle. Shown are representative examples of simulations of V_m (A), # of open CRUs at a given time (B), I_{NCX} (C), and I_{CaL} (D). The traces are synchronized at the MDP to clearly see difference in time course during diastolic depolarization.

Figure 5. Disorder in CRU positions accelerates synchronization of CRU firing and AP ignition process. Shown are representative cycles of AP firing (V_m, blue curves) for 500 ms simulation time beginning from the maximum diastolic polarization (MDP, time=0) for two CRU distributions: Uniformly random (A) and square lattice (B). The ignition process in both cases is characterized by simultaneous activation of CRUs firing (black), I_{NCX} (red), and I_{CaL} (green, truncated), which V_m to the AP activation threshold. However, the activation kinetics are faster in the uniformly random case so its diastolic depolarization is about twice shorter.

Figure 6. Sizes of LCRs increase during diastolic depolarization via propagating CICR as disorder in CRU positions increases from square lattice to uniformly random (from top to bottom). Shown are distributions of local $[Ca]_{sub}$ ([Ca] under cell membrane) at the same membrane potential of -45 mV, i.e. close to the I_{CaL} activation threshold. $[Ca]_{sub}$ is coded by a color scheme shown at the bottom from 0.15 μM to 10 μM; open CRUs are shown by white dots. Closed CRUs in refractory period are shown by blue dots; closed reactivated CRUs (available to

fire) are shown by green dots. JSR Ca level is coded by respective shade (white, blue or green) with a saturation level set at 0.3 mM. See respective Movies 1-5.

Figure 7. Results of sensitivity analysis demonstrating failure of pacemaker function (AP firing ceased) in cell models with square lattice positions of CRUs, but not with uniformly random CRU distribution at lower, albeit physiological, I_{CaL} densities. A: Bridging experimentally measured I_{CaL} densities (green circles) and our model parameter g_{CaL} describing maximum I_{CaL} conductance (magenta). The data points for I_{CaL} experimental data were replotted from (Monfredi et al., 2017). Magenta band shows range of g_{CaL} in our sensitivity analysis. B: Results of sensitivity analyses for cell models with uniformly random CRU distribution (red) and square lattice distribution (blue). Data points are average CLs evaluated between 5 and 16.5 s after simulation onset. Red shade square shows the g_{CaL} margin where square lattice models failed, but uniformly random model continued generating spontaneous APs. C: An example of AP firing failure in a square lattice model, but rhythmic AP firing in uniformly random model when in both cases g_{CaL} reduced to 70% of its basal value. See original simulation data in Fig. A2

Figure 8. New insights for dormant cell signaling. A: Despite both models with uniformly random and square lattice models failed at a very low g_{CaL} of 0.2552 nS/pF, subthreshold V_m oscillations continue in both cases. However, oscillations in uniformly random distribution had much larger amplitude (shown in inset). B: The oscillations were not only much more powerful but occurred at a faster frequency as revealed by the power spectra of both V_m signals computed for time after AP failure (from 0.5 s to 16.5 s).

Figure 9. Disorder in CRU positions shortens the CL, but simultaneously decreases the effect of β-adrenergic receptor stimulation. A: Bar graph of respective AP firing lengths (for numerical data, see Table 1). B: An example of simulations of βAR stimulation effects for extreme cases of CRU distributions: uniformly random (upper panel) vs. square lattice (bottom panel). C: CL changes correlate with basal CL (before βAR stimulation), βAR stimulation synchronizes AP firing towards a common AP firing CL. See original simulation data in Fig. A3

Figure 10. Numerical simulations illustrating the mechanism of a stronger reduction of CL by βAR stimulation (βARs) in square lattice vs. uniform random CRU spatial distribution (V_m, top pannels) . The stronger effect in the lattice case is due to its stronger effect on CRU recruitment (N_{CRU}, middle panels) and its attendant activation of I_{NCX} (bottom panels). Disorder in CRU positions substantially shortens the CL in basal state, but simultaneously decreases the effect of stimulation.

Figure 11. Results of numerical simulations illustrating importance of $Ca_v1.3$ isoform of LCC for AP firing and the effects of randomness in CRU positions. A: The two plots show results of our sensitivity analysis with various contribution of $Ca_v1.3$ into I_{CaL} performed for two different CRU distributions: uniformly random and square lattice. Multicolor arrows show the total effects of randomness (black and green) and $Ca_v1.3$ (blue and orange). Data points are average CLs evaluated between 5 and 16.5 s after simulation onset. B and C: Effect of βAR stimulation in the models with 50% of $Ca_v1.2$ in I_{CaL}. Intervalograms illustrate a much stronger stimulation effect in the cell model with square lattice distribution of CRUs vs. uniformly random distribution of CRUs.

Figure A1. Representative Ca sparks generated by our CRU model at two different initial JSR Ca loading 1 mM (A) and 0.3 mM (B). Left panels: Overlapped time series of [Ca] in dyadic cleft (blue line) and [Ca] in JSR (red line). Right panels: Respective line-scan images of the sparks. The spark at 0.3 mM of JSR Ca loading had a lower amplitude and duration. To better illustrate Ca spread, the color map in line-scan images is saturated at $[Ca]_{cleft}$ = 1 μM. CRU positions for square lattice configuration are shown by blue lines. The spark was generated by CRU3 and the images show that its outskirt could reach neighbouring CRUs (CRU2 and CRU4) at 1 mM JSR Ca loading, but not at 0.3 mM (i.e. at the $[Ca]_{JSR}$ threshold of spark activation). The membrane potential was -60 mV.

Figure A2. SAN cell with uniformly random distribution of CRUs features more robust spontaneous AP firing (right panels) vs. that with a square lattice distribution of CRUs (left panels). Shown are simulated AP traces in our g_{CaL} sensitivity analysis in which g_{CaL} gradually decreased from 100% to 55% of its basal state value of 0.464 nS/pF. Specific g_{CaL} values are shown at the top of each panel. Red shade shows the AP safety margin (functional reserve) that a SAN cell can utilize to increase its robust function via redistribution of its CRU locations to increase the presence of noise (i.e. natural CRU clustering).

Figure A3. Effect of βAR stimulation wanes as disorder in CRU positions increases. Shown are CL intervalograms for simulations of AP firing in basal state (blue plots) and in the presence of βAR stimulation (red plots). Note: βAR stimulation shortens the CLs towards about the same level within a narrow range of 291 ms to 266 ms, i.e. βAR stimulation unifies spontaneous AP

firing towards a higher common rate. All simulations started from the identical initial conditions.

Figure A4. $Ca_v1.3$ accelerates AP firing rate by interacting with CRUs and I_{NCX} in the model with square lattice distribution of CRUs. Increasing percentage of $Ca_v1.3$ in I_{CaL} increases synchronization and recruitment of CRU to release Ca, resulting in earlier activation of I_{NCX} and shorter AP firing cycle. Shown are representative examples of simulations of V_m (A), # of open CRUs at a given time (B), I_{NCX} (C), and I_{CaL} (D). The traces are synchronized at the MDP to clearly see difference in time course during diastolic depolarization.

Figure A5. $Ca_v1.3$ accelerates AP firing rate by interacting with CRUs and I_{NCX} in the model with uniformly random distribution of CRUs. Increasing percentage of Cav1.3 in I_{CaL} increases synchronization and recruitment of CRU to release Ca, resulting in earlier activation of I_{NCX} and shorter AP firing cycle. Shown are representative examples of simulations of V_m (A), # of open CRUs at a given time (B), I_{NCX} (C), and I_{CaL} (D). The traces are synchronized at the MDP to clearly see difference in time course during diastolic depolarization.

Figure A6. $Ca_v1.3$ increases robustness of pacemaker function. Shown is an example of revival of spontaneous AP firing in a dormant cell with uniformly random distribution of CRUs and decreased g_{CaL} (panel A, the same as in Fig. 7D) by a substitution of a small fraction (20%) of $Ca_v1.2$ by $Ca_v1.3$ in I_{CaL} (Panel B).

Figure A7. Importance of LCC coupling to CRUs demonstrated in SAN cell models with uncoupled $Ca_v1.2$ from CRUs (still coupled to $Ca_v1.3$) vs. models in which CRUs were coupled to both $Ca_v1.2$ and $Ca_v1.3$. A and B: Intervalograms of simulated CLs in the partially uncoupled CRU models with uniformly random and square lattice distribution of CRUs, respectively. C: Results of sensitivity analyses with various $Ca_v1.3$ percentage in I_{CaL} for the partially uncoupled models with uniformly random CRU distribution (orange) and square lattice distribution (blue). The results are compared with those of fully coupled models (respective dashed line plots), replotted from Figure 11A. Data points are average CLs evaluated between 5 and 16.5 s after simulation onset. Black arrows show the $\%Ca_v1.3$ margin where the models failed to generate APs.

Table 1. Average values for spontaneous CL in numerical models with different CRU distributions in basal state and in response to βAR stimulation (see respective plots in Fig. 9A). SD provides the deviating from the "square lattice" positions, following Gaussian distribution with standard deviation, SD

1) CRUs placed exactly at the nodes of a square lattice of 1.44 μm size.

2) CRUs slightly deviating from the "square lattice" positions, following Gaussian distribution with standard deviation, SD= 0.25 μm.

3) CRUs moderately deviating from "square lattice" positions, following Gaussian distribution with SD= 0.5 μm.

4) CRUs strongly deviating from the "square lattice" positions, following Gaussian distribution with SD=0.75 μm.

5) Uniformly independently random CRU positions excluding overlap.

CL was measured for the time interval from 5 s to 16.5 s (when simulations ended). All model simulations began with identical initial conditions and the initial 5s period was omitted from the analysis to allow the system to reach a balance (see our original intervalograms in Fig. A3).

Cycle Length	Square lattice	SD=0.25, μm	SD=0.5, μm	SD=0.75, μm	Uniformly random
Basal state, ms	461.3167	410.225	367.36	346.2667	318.1686
βAR stimulation, ms	290.5686	282.0629	267.9727	262.6303	265.9219
Change, ms	170.7481	128.1621	99.38727	83.63636	52.2467
Change, %	37.01321	31.24191	27.05446	24.15374	16.42107

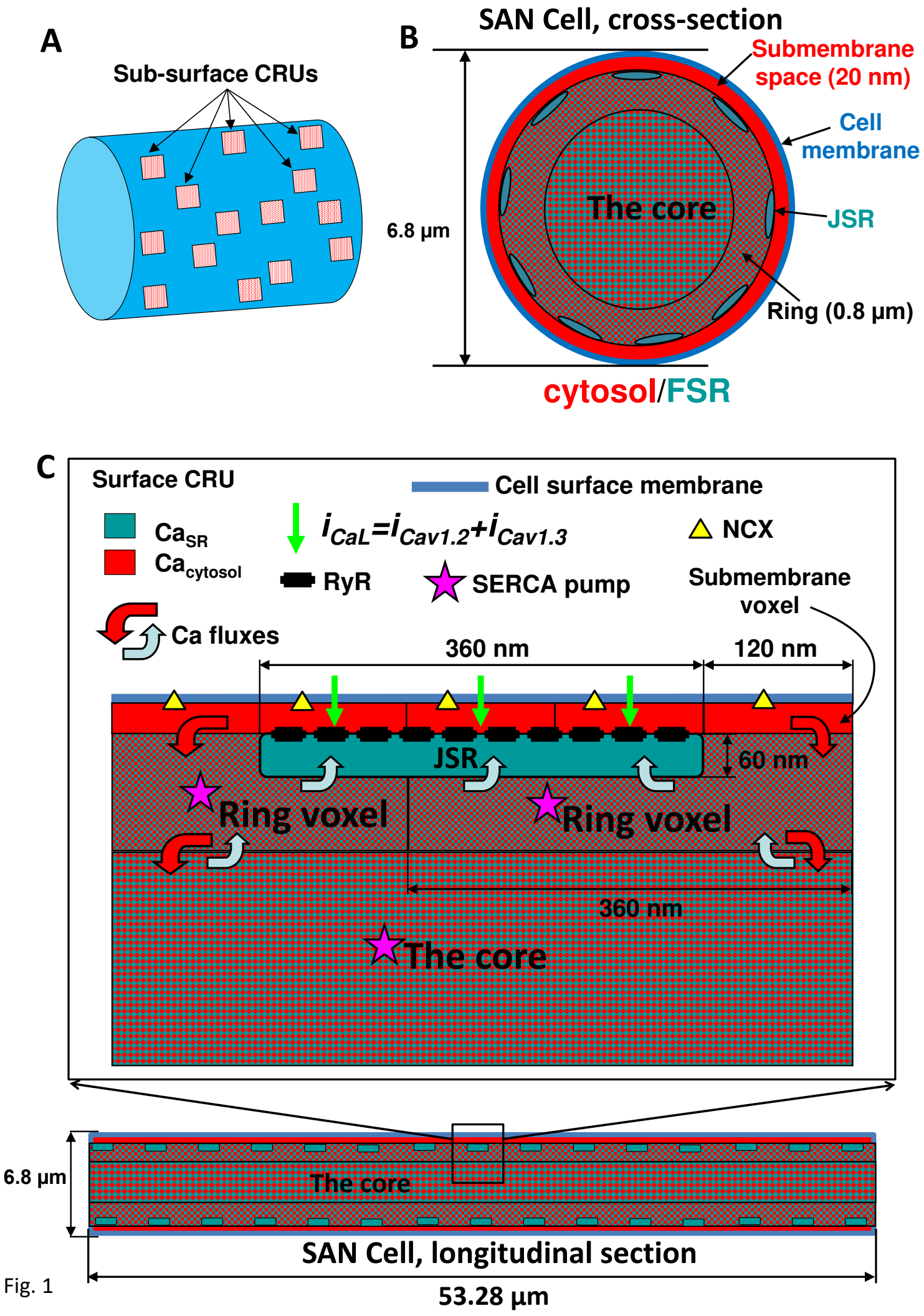
A
Sub-surface CRUs
B
SAN Cell, cross-section
Submembrane space (20 nm)
Cell membrane
The core
JSR
Ring (0.8 μm)
6.8 μm
cytosol/FSR
C
Surface CRU
Cell surface membrane
Ca_{SR}
$Ca_{cytosol}$
$i_{CaL}=i_{Cav1.2}+i_{Cav1.3}$
NCX
RyR
SERCA pump
Submembrane voxel
Ca fluxes
360 nm
120 nm
JSR
60 nm
Ring voxel
Ring voxel
360 nm
The core
6.8 μm
The core
SAN Cell, longitudinal section
53.28 μm

Fig. 1

Square Lattice

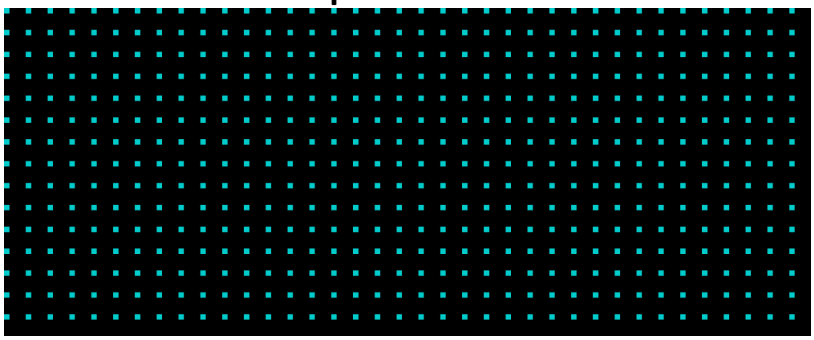

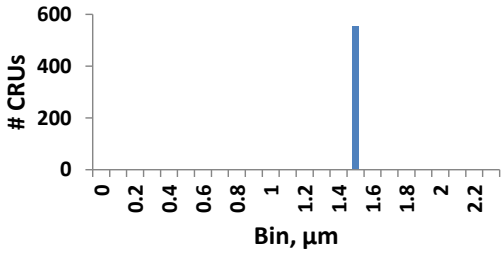

Slightly perturbed Square Lattice, SD=0.25 µm

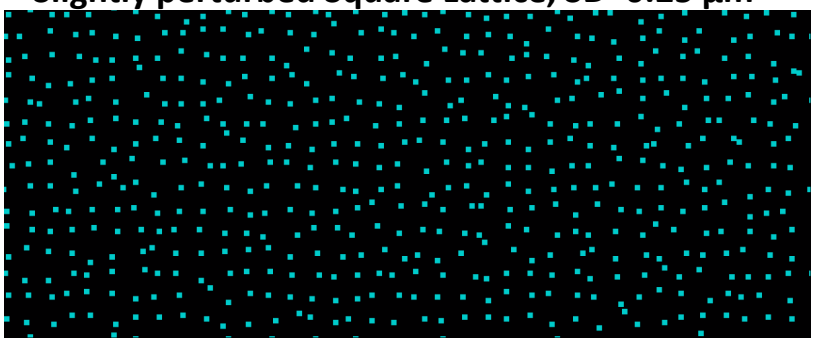

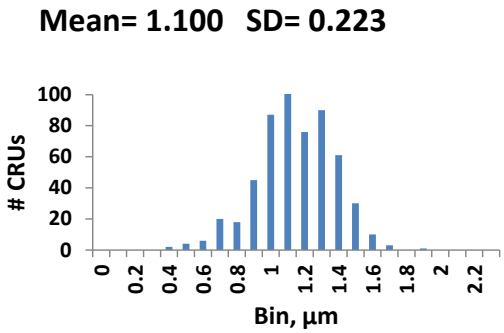

Moderately perturbed Square Lattice, SD=0.5 µm

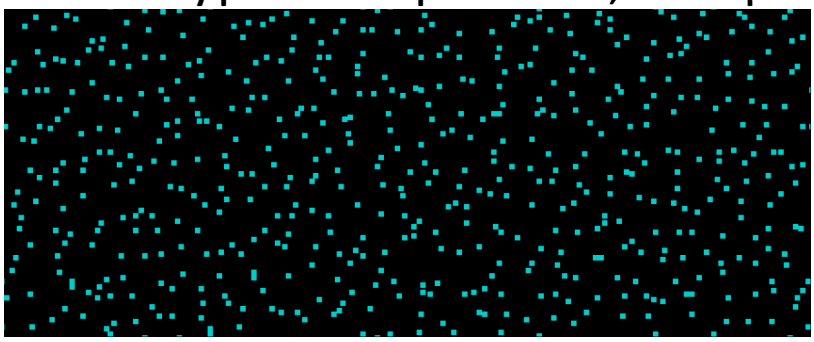

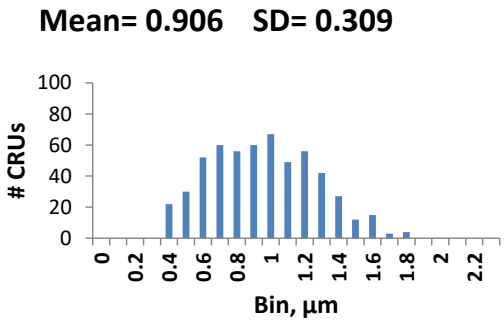

Strongly perturbed Square Lattice, SD=0.75 µm

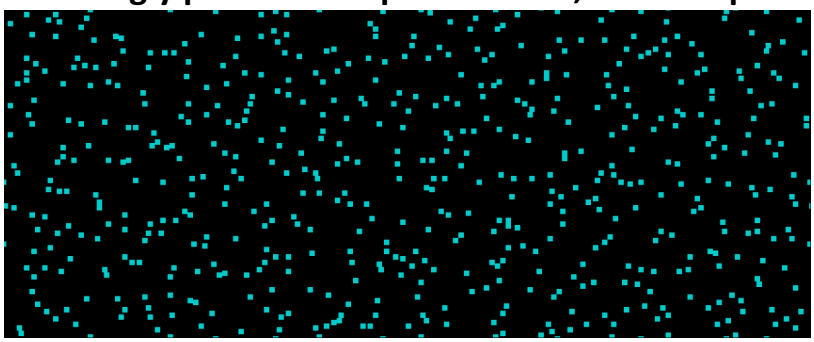

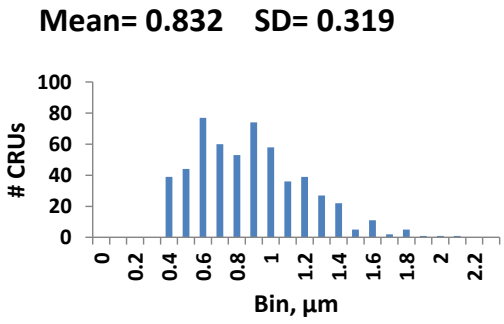

Uniformly Random

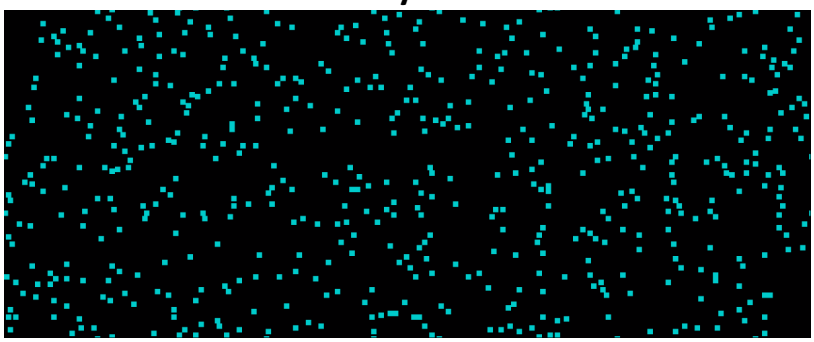

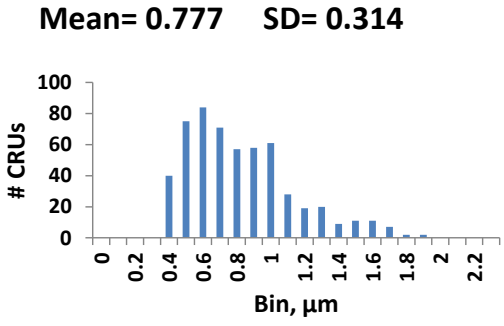

Fig. 2

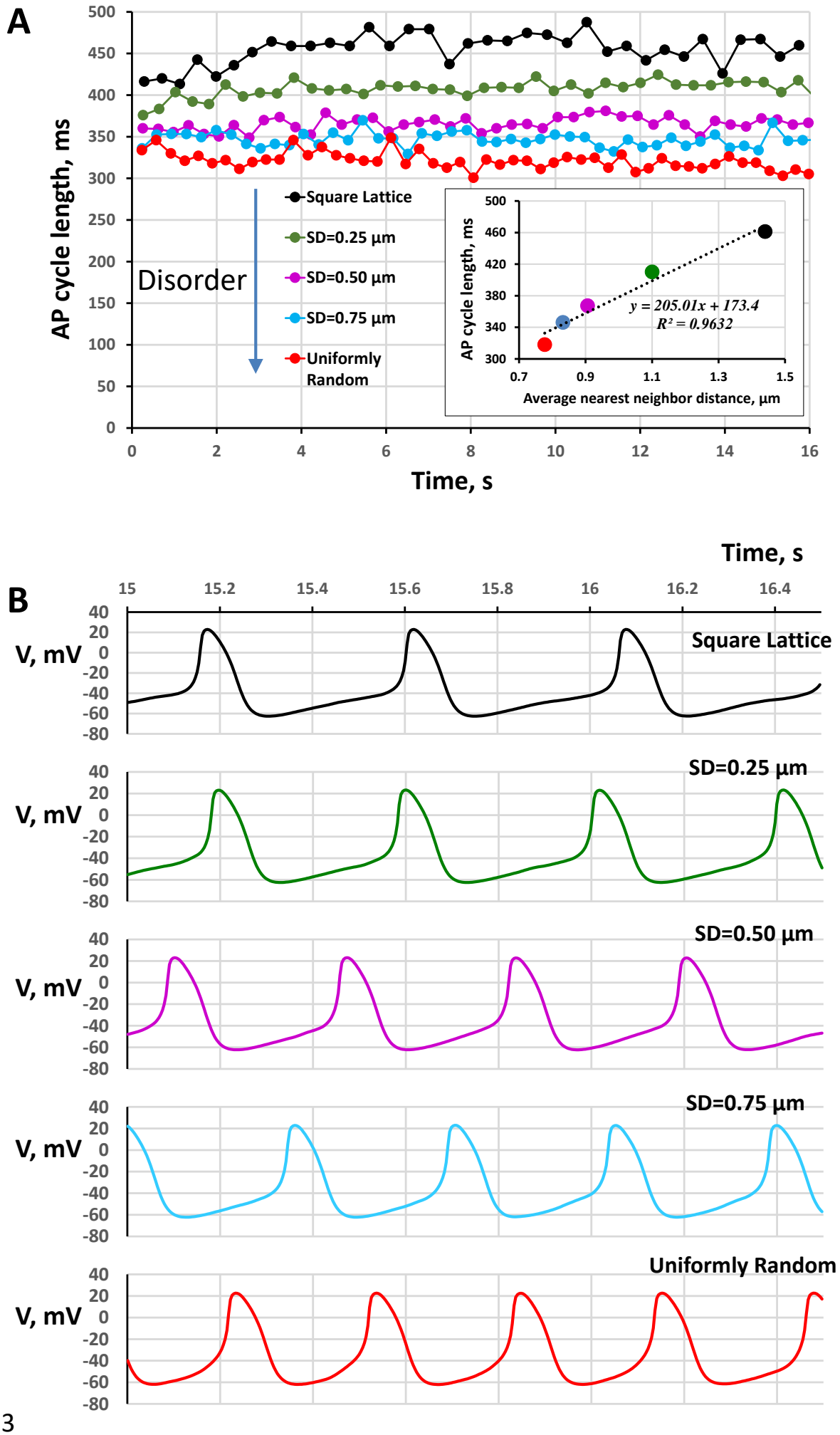
A
AP cycle length, ms
Time, s
Square Lattice
SD=0.25 µm
SD=0.50 µm
SD=0.75 µm
Uniformly Random
Disorder
y = 205.01x + 173.4
R² = 0.9632
Average nearest neighbor distance, µm
B
Time, s
V, mV
Square Lattice
SD=0.25 µm
SD=0.50 µm
SD=0.75 µm
Uniformly Random

Fig. 3

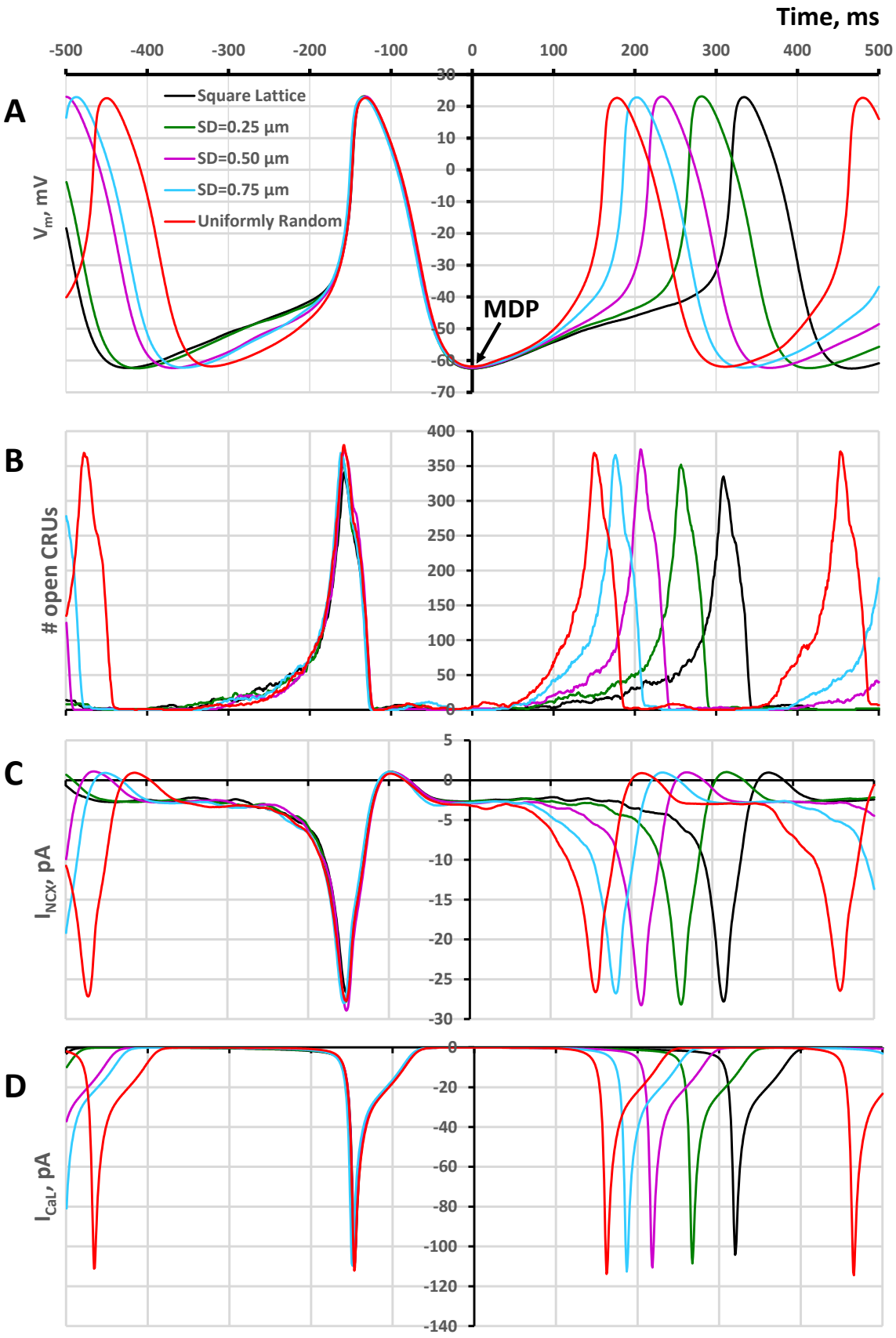
Time, ms
A
B
C
D
Square Lattice
SD=0.25 µm
SD=0.50 µm
SD=0.75 µm
Uniformly Random
MDP
V_m, mV
open CRUs
I_{NCX}, pA
I_{CaL}, pA

Fig. 4

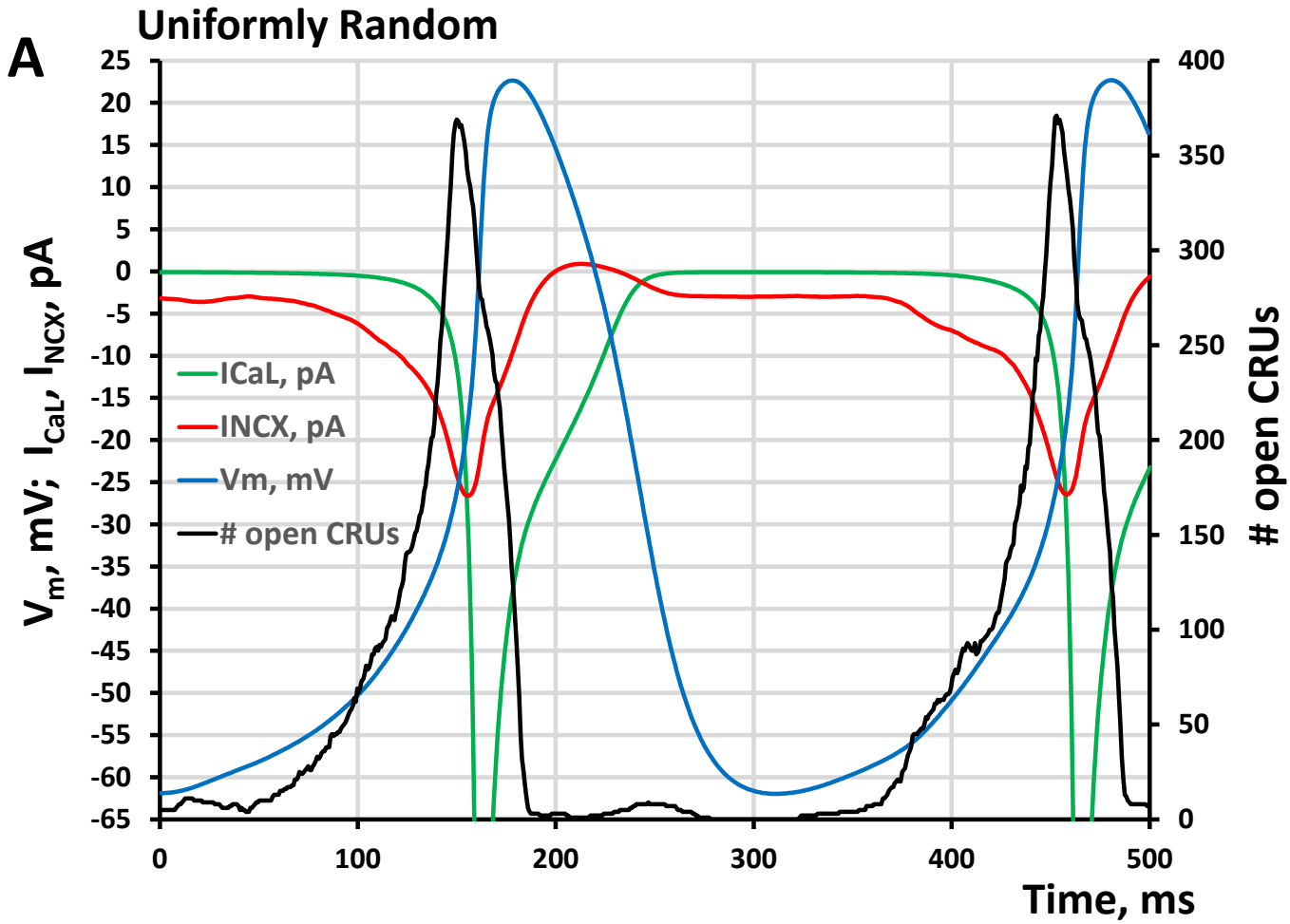
A
Uniformly Random
ICaL, pA
INCX, pA
Vm, mV
open CRUs
Vm, mV; ICaL, INCX, pA
open CRUs
Time, ms

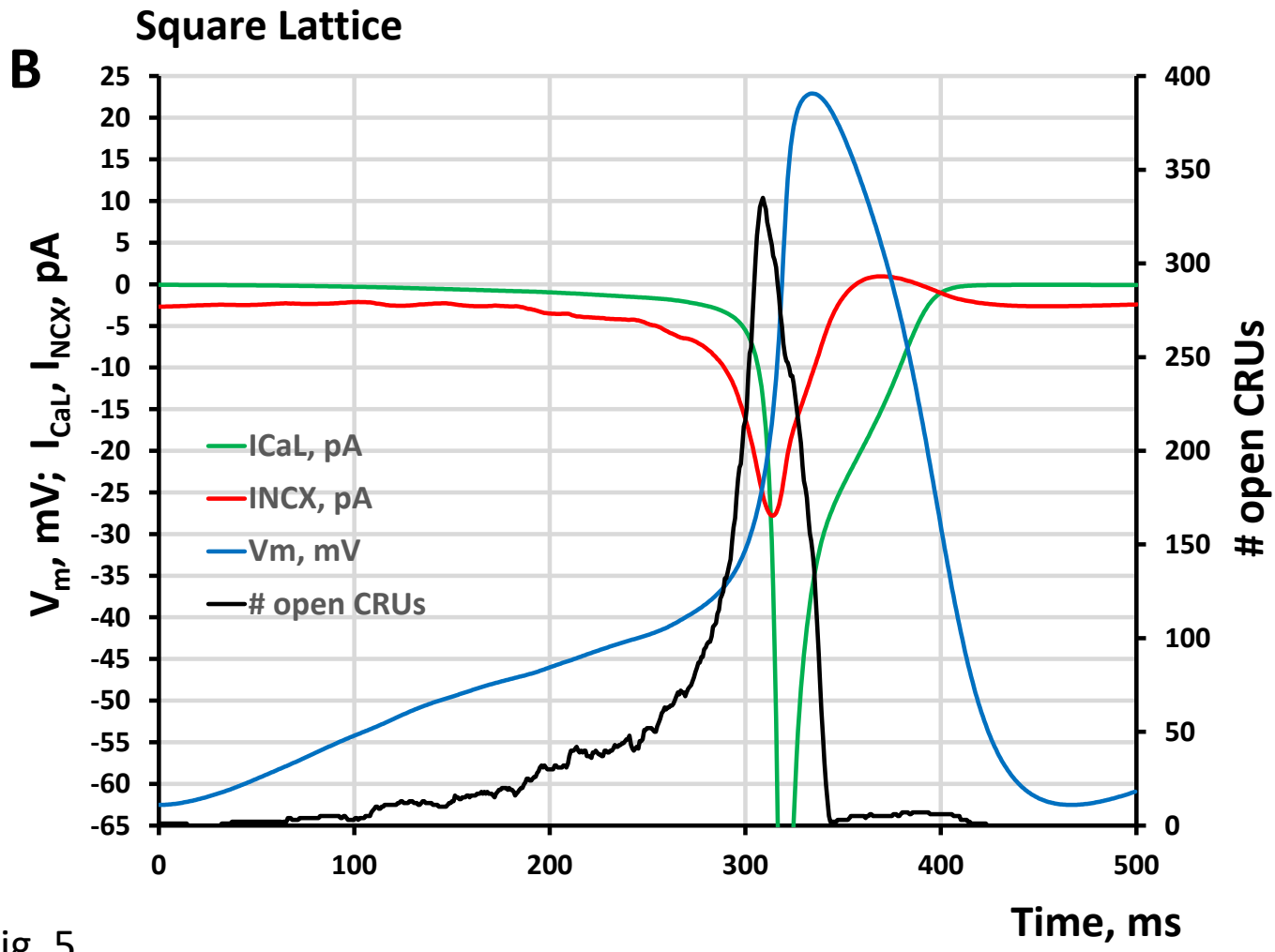
B
Square Lattice
ICaL, pA
INCX, pA
Vm, mV
open CRUs
Vm, mV; ICaL, INCX, pA
open CRUs
Time, ms

Fig. 5

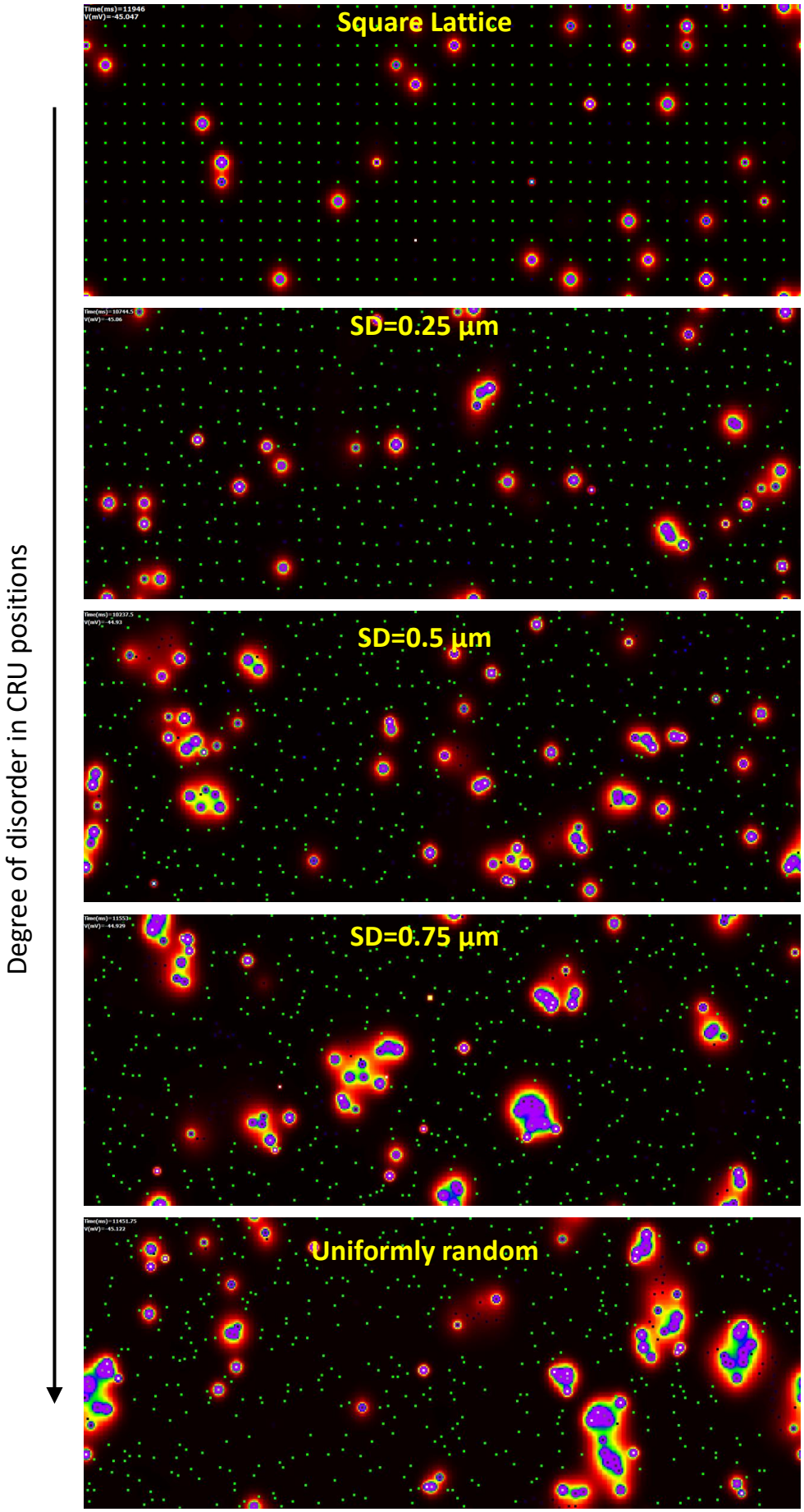
Square Lattice
SD=0.25 µm
SD=0.5 µm
SD=0.75 µm
Uniformly random
Degree of disorder in CRU positions
0.15 µM
[Ca]sub
10 µM
Ready to open CRU
Refractory CRU
Open CRU

Fig. 6

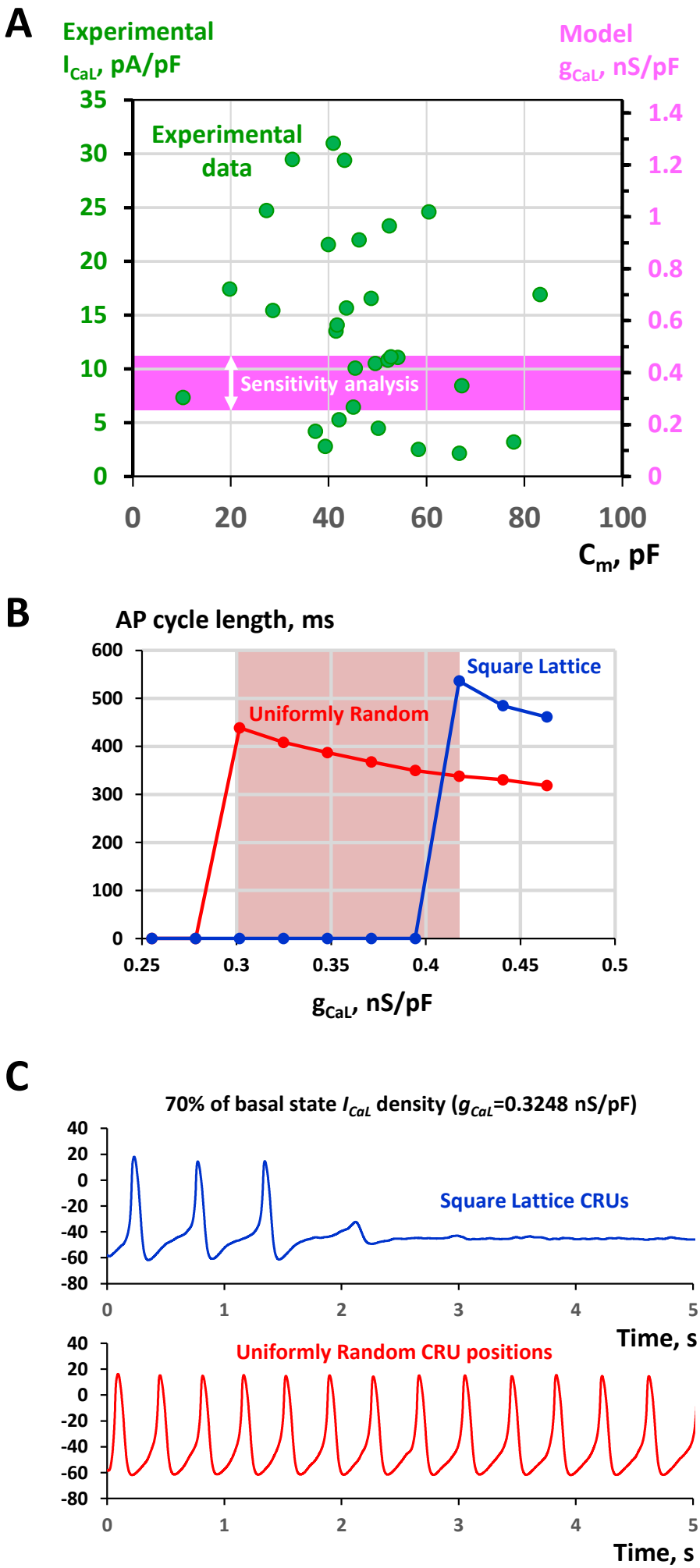
A
Experimental
I_{CaL}, pA/pF
Model
g_{CaL}, nS/pF
Experimental data
Sensitivity analysis
35
30
25
20
15
10
5
0
1.4
1.2
1
0.8
0.6
0.4
0.2
0
0
20
40
60
80
100
C_m, pF
B
AP cycle length, ms
Square Lattice
Uniformly Random
600
500
400
300
200
100
0
0.25
0.3
0.35
0.4
0.45
0.5
g_{CaL}, nS/pF
C
70% of basal state I_{CaL} density (g_{CaL}=0.3248 nS/pF)
Square Lattice CRUs
Uniformly Random CRU positions
40
20
0
-20
-40
-60
-80
0
1
2
3
4
5
Time, s

Fig. 7

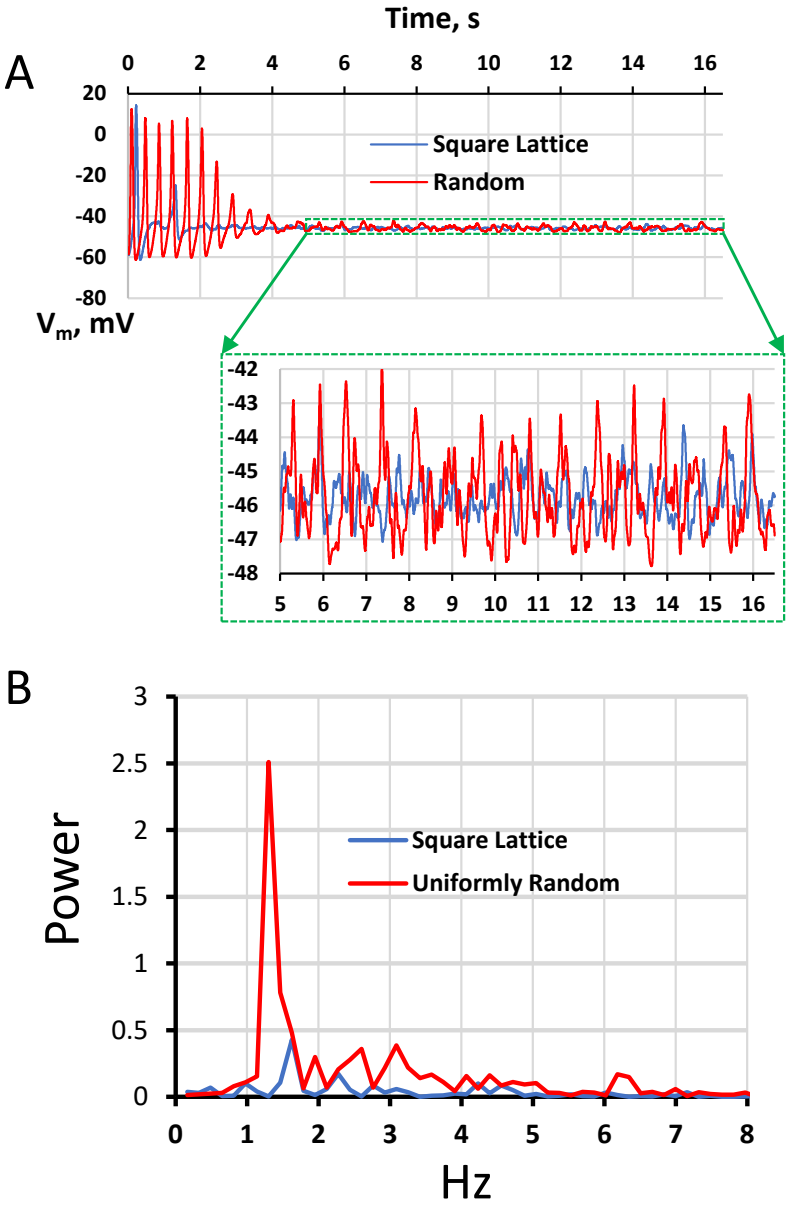
A
Time, s
0
2
4
6
8
10
12
14
16
20
0
-20
-40
-60
-80
V_m, mV
Square Lattice
Random
-42
-43
-44
-45
-46
-47
-48
5
6
7
8
9
10
11
12
13
14
15
16
B
Power
3
2.5
2
1.5
1
0.5
0
Square Lattice
Uniformly Random
0
1
2
3
4
5
6
7
8
Hz

Fig. 8

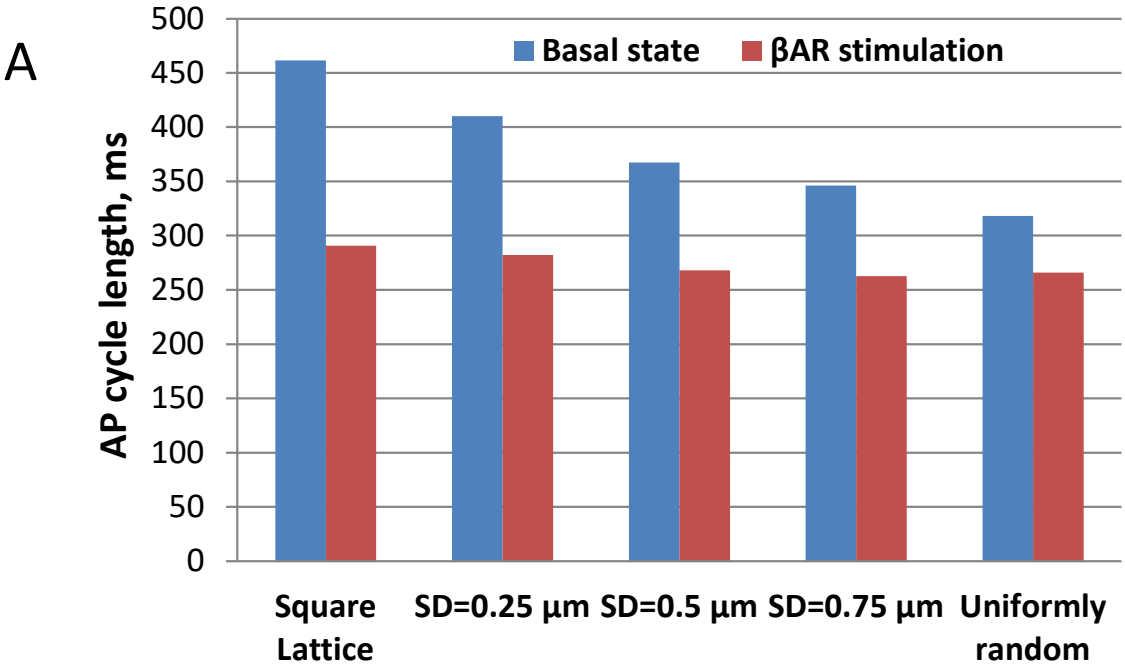
A
Basal state
βAR stimulation
AP cycle length, ms
500
450
400
350
300
250
200
150
100
50
0
Square Lattice
SD=0.25 µm
SD=0.5 µm
SD=0.75 µm
Uniformly random

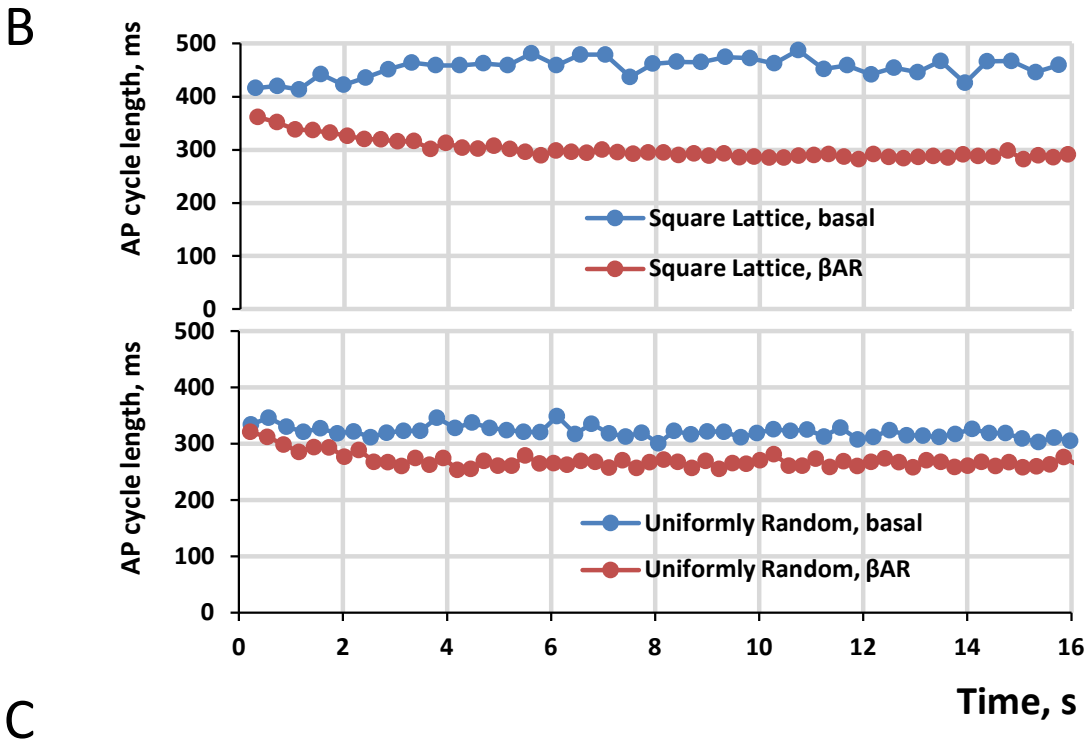
B
AP cycle length, ms
Square Lattice, basal
Square Lattice, βAR
Uniformly Random, basal
Uniformly Random, βAR
0
2
4
6
8
10
12
14
16
Time, s

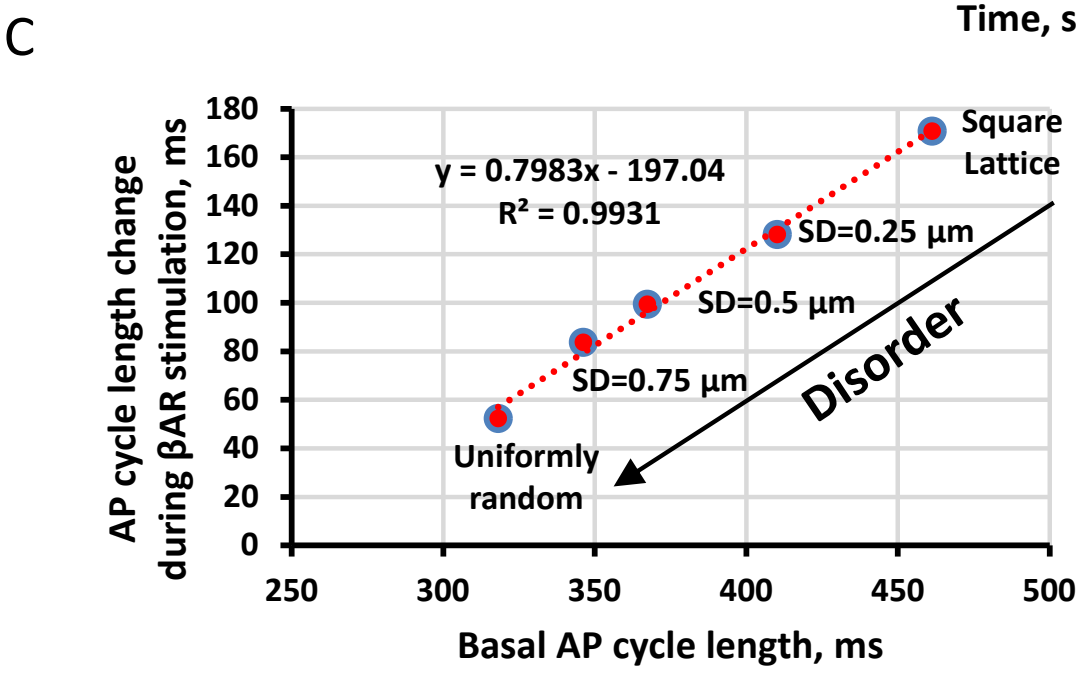
C
AP cycle length change during βAR stimulation, ms
y = 0.7983x - 197.04
R² = 0.9931
Square Lattice
SD=0.25 µm
SD=0.5 µm
SD=0.75 µm
Uniformly random
Disorder
Basal AP cycle length, ms

Fig. 9

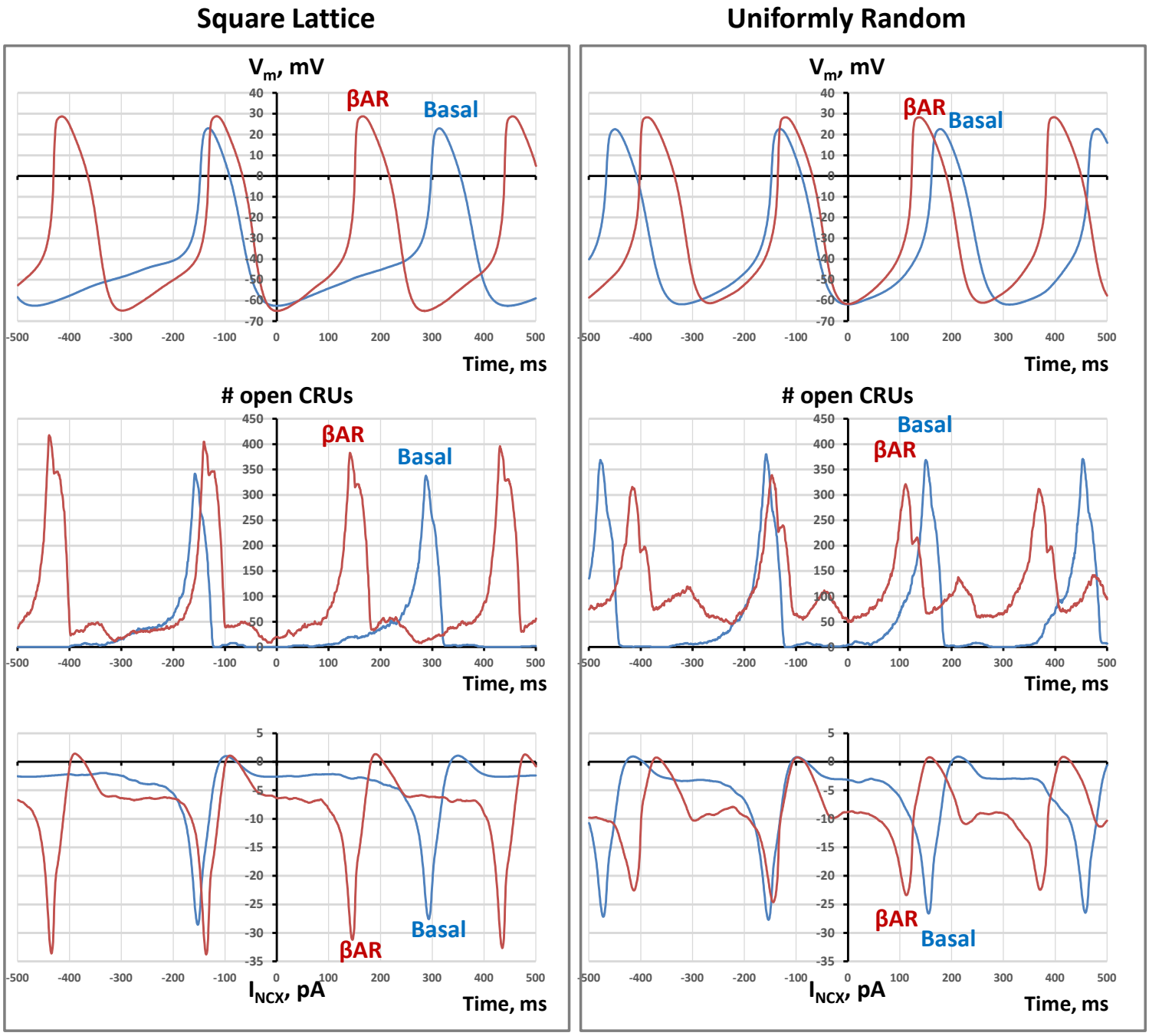
Square Lattice
Uniformly Random
V_m, mV
βAR
Basal
Time, ms
open CRUs
βAR
Basal
Time, ms
I_{NCX}, pA
βAR
Basal
Time, ms

Fig. 10

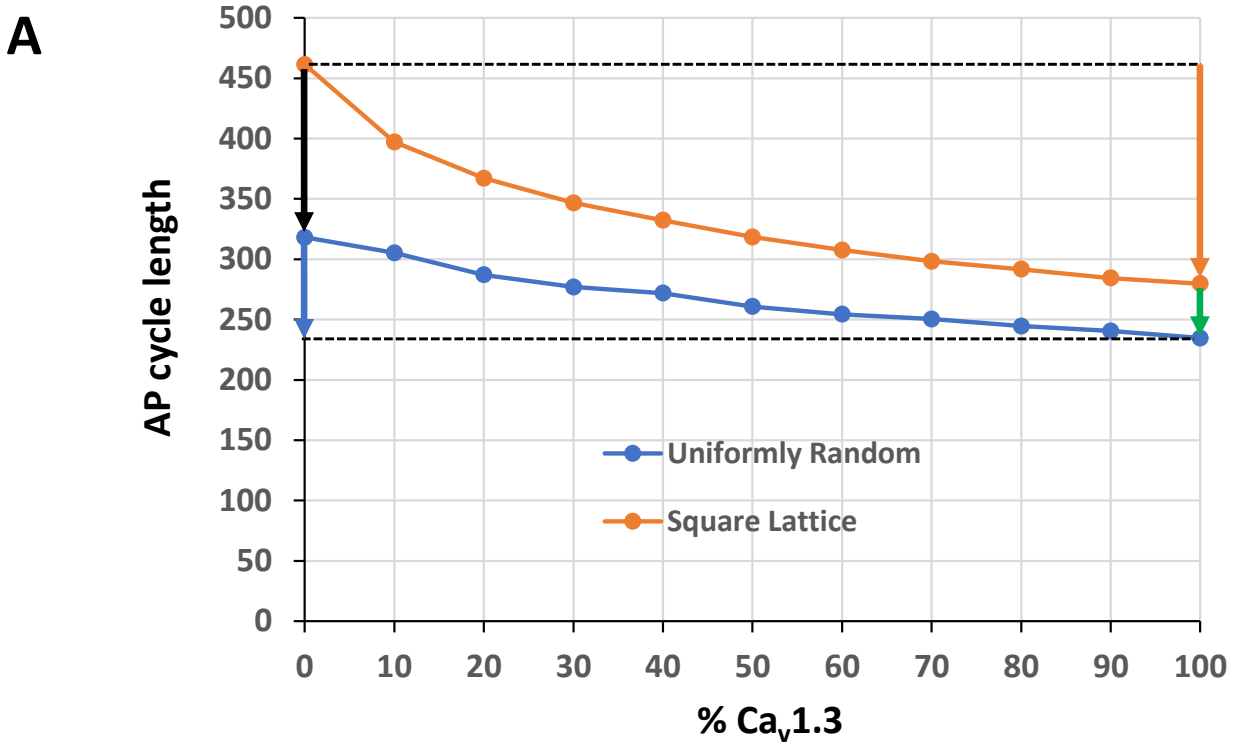
A
AP cycle length
500
450
400
350
300
250
200
150
100
50
0
0
10
20
30
40
50
60
70
80
90
100
% Ca$_v$1.3
Uniformly Random
Square Lattice

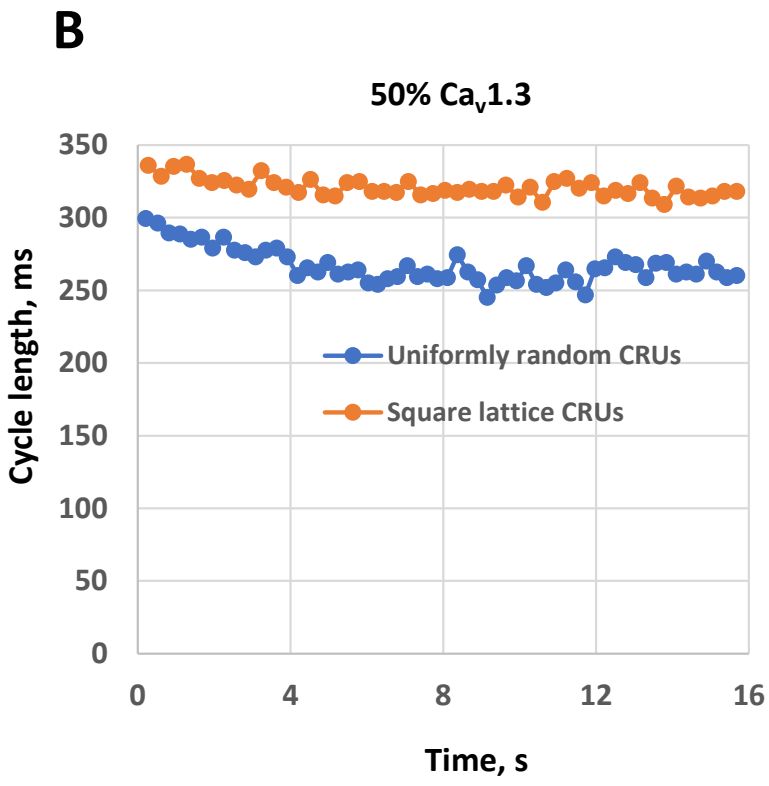
B
50% Ca$_v$1.3
Cycle length, ms
350
300
250
200
150
100
50
0
0
4
8
12
16
Time, s
Uniformly random CRUs
Square lattice CRUs

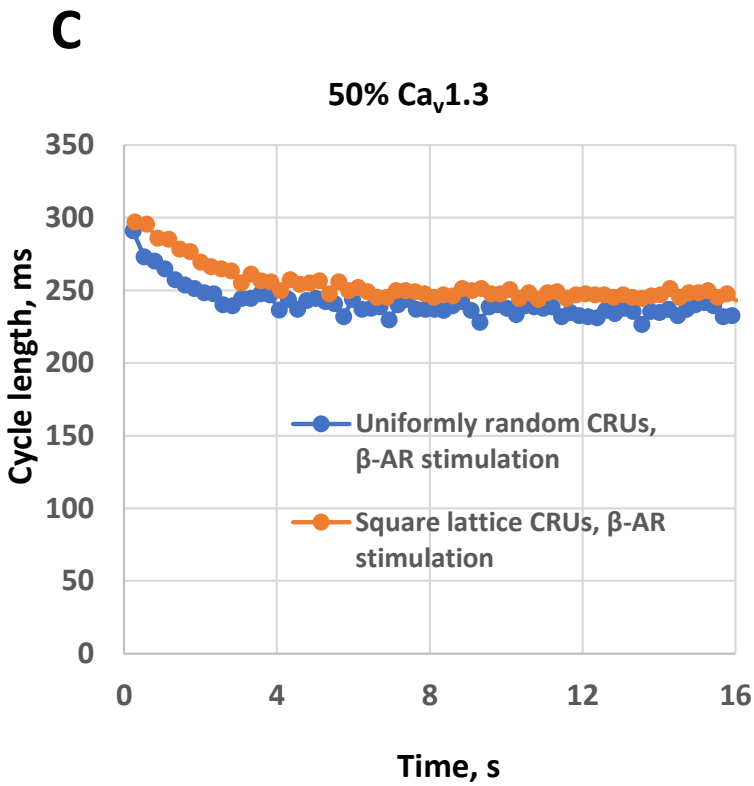
C
50% Ca$_v$1.3
Cycle length, ms
350
300
250
200
150
100
50
0
0
4
8
12
16
Time, s
Uniformly random CRUs, β-AR stimulation
Square lattice CRUs, β-AR stimulation

Fig. 11

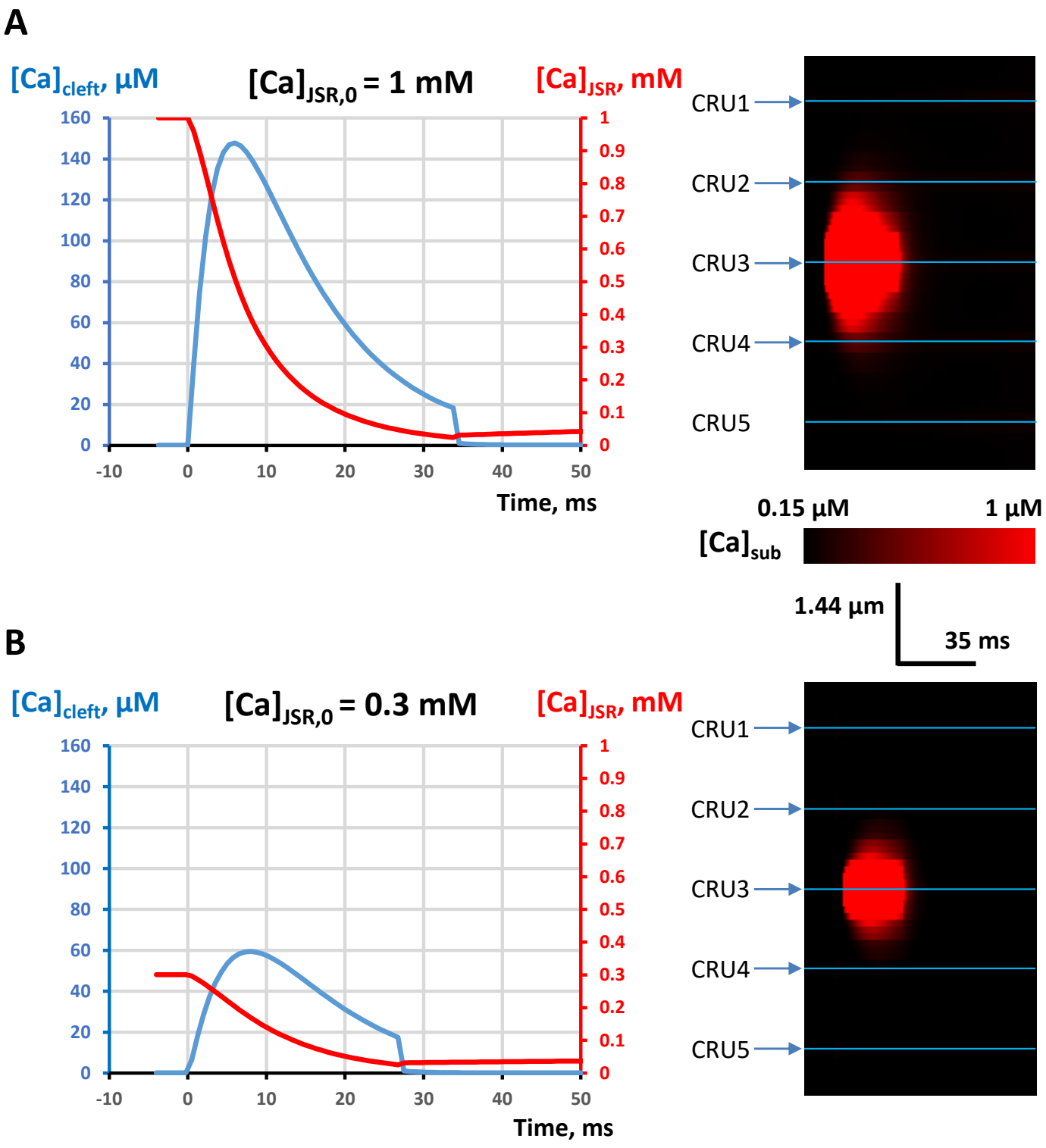
A
[Ca]cleft, µM
[Ca]JSR,0 = 1 mM
[Ca]JSR, mM
160
140
120
100
80
60
40
20
0
1
0.9
0.8
0.7
0.6
0.5
0.4
0.3
0.2
0.1
0
-10
0
10
20
30
40
50
Time, ms
CRU1
CRU2
CRU3
CRU4
CRU5
0.15 µM
1 µM
[Ca]sub
1.44 µm
35 ms
B
[Ca]cleft, µM
[Ca]JSR,0 = 0.3 mM
[Ca]JSR, mM
160
140
120
100
80
60
40
20
0
1
0.9
0.8
0.7
0.6
0.5
0.4
0.3
0.2
0.1
0
-10
0
10
20
30
40
50
Time, ms
CRU1
CRU2
CRU3
CRU4
CRU5

Fig. A1

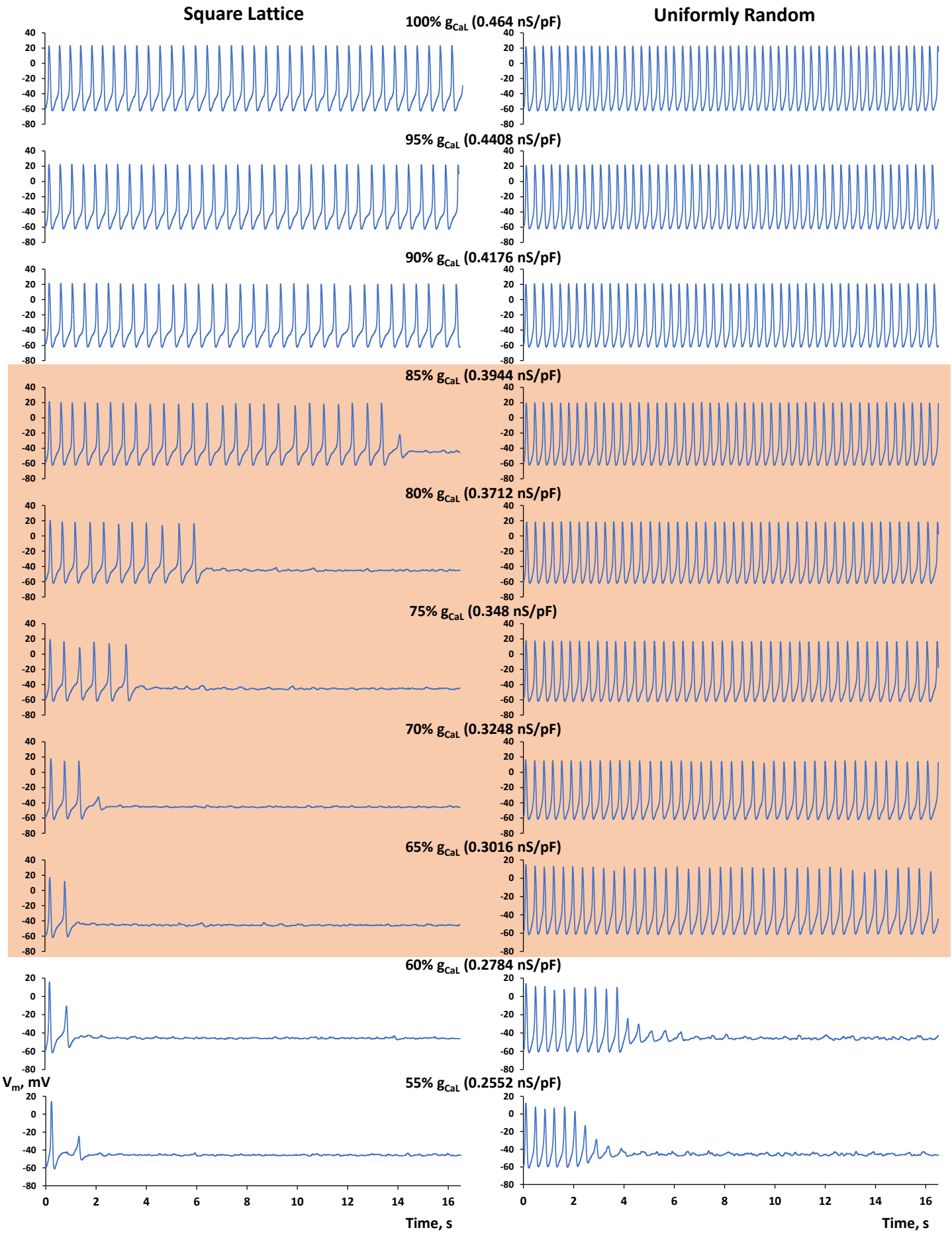
Square Lattice
Uniformly Random
100% g_{CaL} (0.464 nS/pF)
95% g_{CaL} (0.4408 nS/pF)
90% g_{CaL} (0.4176 nS/pF)
85% g_{CaL} (0.3944 nS/pF)
80% g_{CaL} (0.3712 nS/pF)
75% g_{CaL} (0.348 nS/pF)
70% g_{CaL} (0.3248 nS/pF)
65% g_{CaL} (0.3016 nS/pF)
60% g_{CaL} (0.2784 nS/pF)
55% g_{CaL} (0.2552 nS/pF)
V_m, mV
Time, s
Time, s

Fig. A2

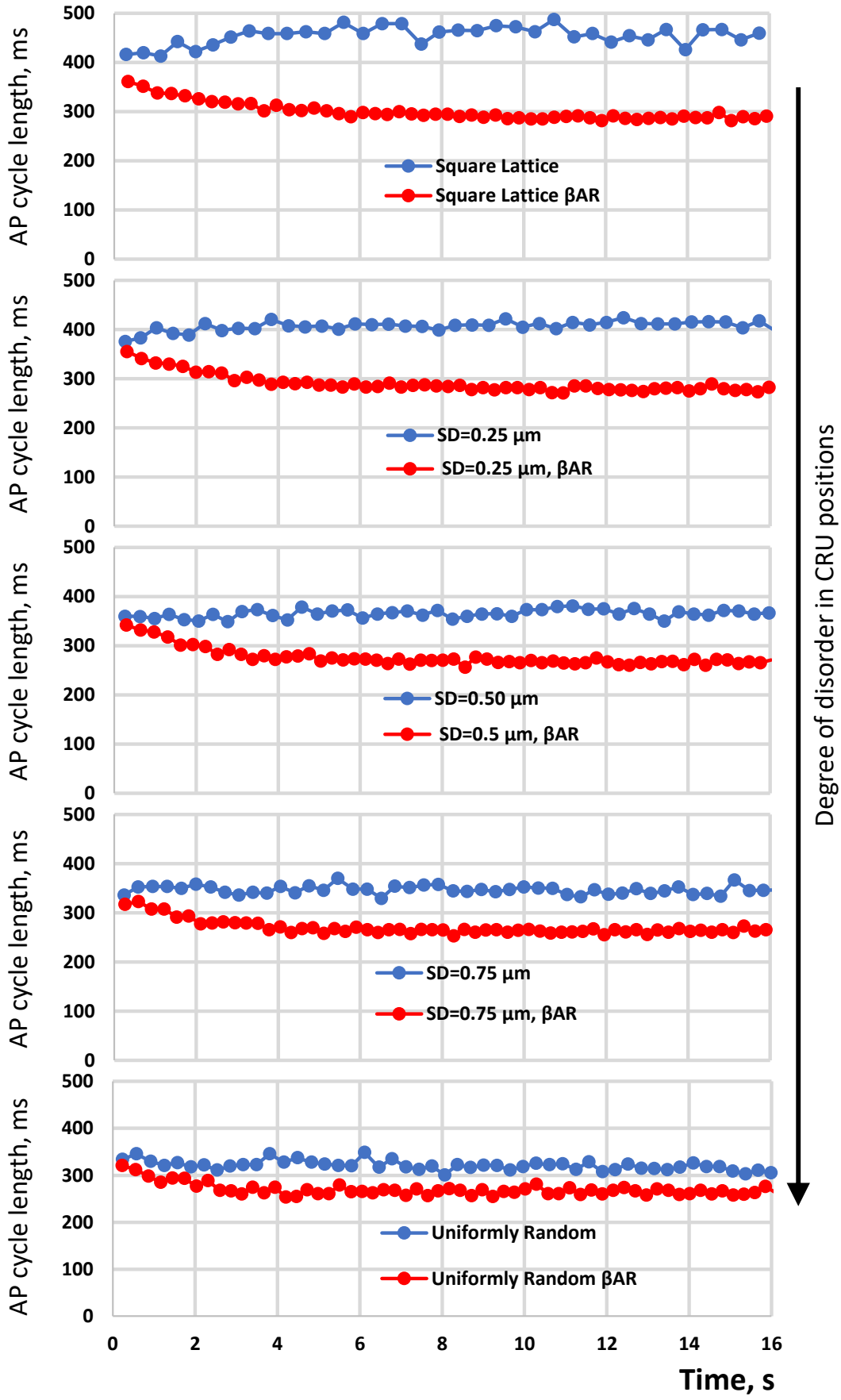
AP cycle length, ms
500
400
300
200
100
0
Square Lattice
Square Lattice βAR
SD=0.25 µm
SD=0.25 µm, βAR
SD=0.50 µm
SD=0.5 µm, βAR
SD=0.75 µm
SD=0.75 µm, βAR
Uniformly Random
Uniformly Random βAR
0
2
4
6
8
10
12
14
16
Time, s
Degree of disorder in CRU positions

Fig. A3

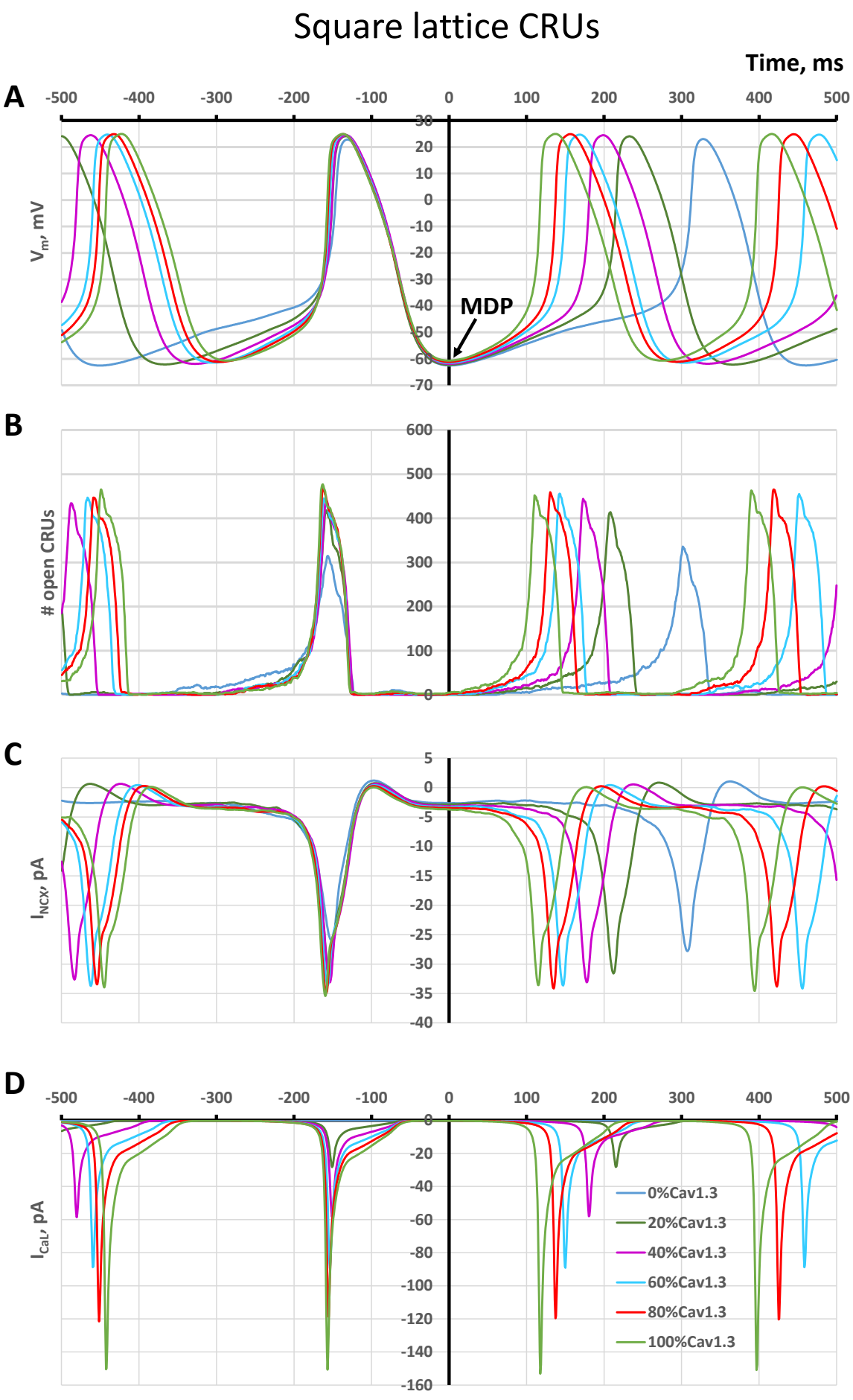
Square lattice CRUs
Time, ms
A
B
C
D
V_m, mV
open CRUs
I_{NCX}, pA
I_{CaL}, pA
MDP
0%Cav1.3
20%Cav1.3
40%Cav1.3
60%Cav1.3
80%Cav1.3
100%Cav1.3

Fig. A4

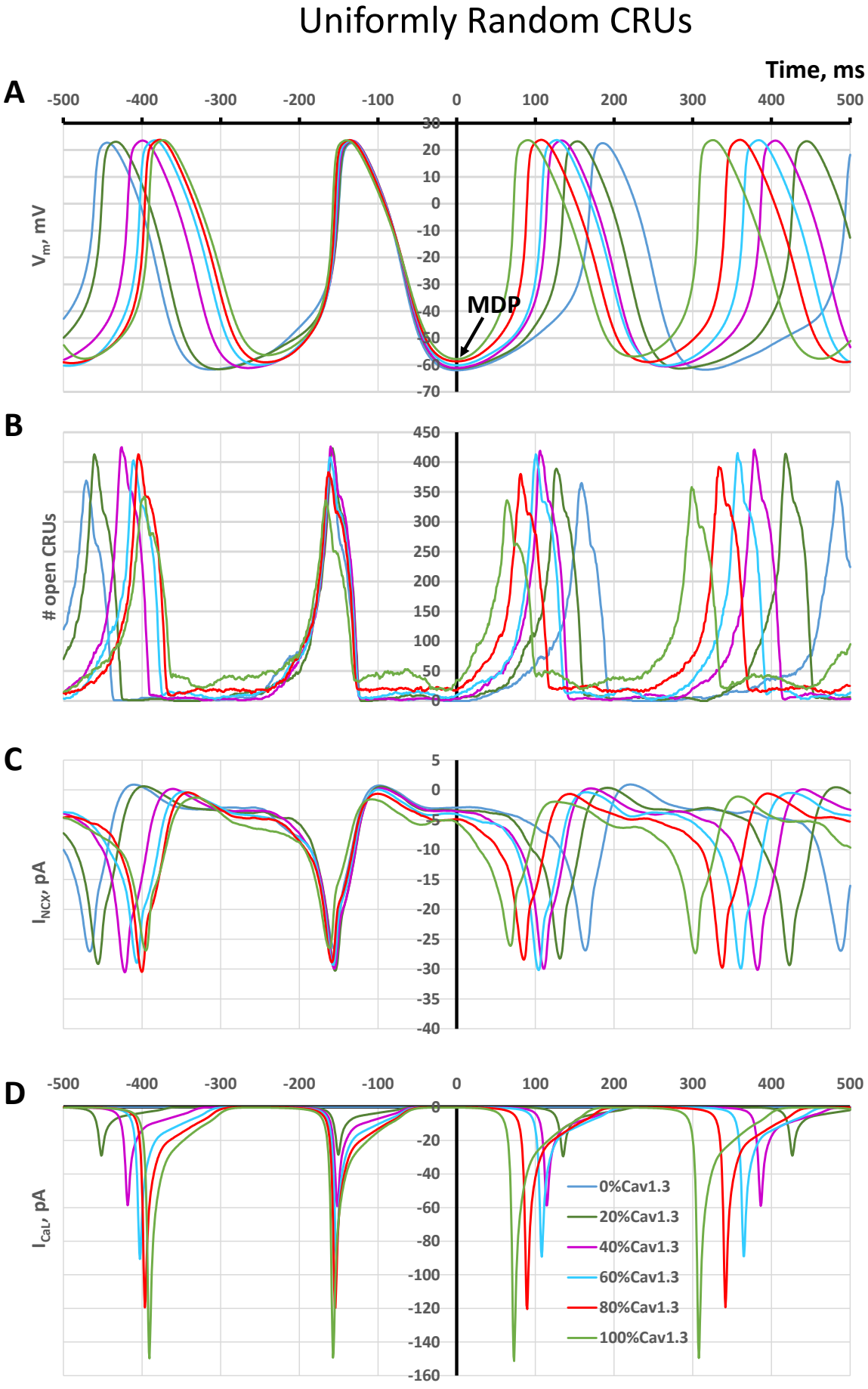
Uniformly Random CRUs
Time, ms
A
B
C
D
MDP
V_m, mV
open CRUs
I_{NCX}, pA
I_{CaL}, pA
0%Cav1.3
20%Cav1.3
40%Cav1.3
60%Cav1.3
80%Cav1.3
100%Cav1.3

Fig. A5

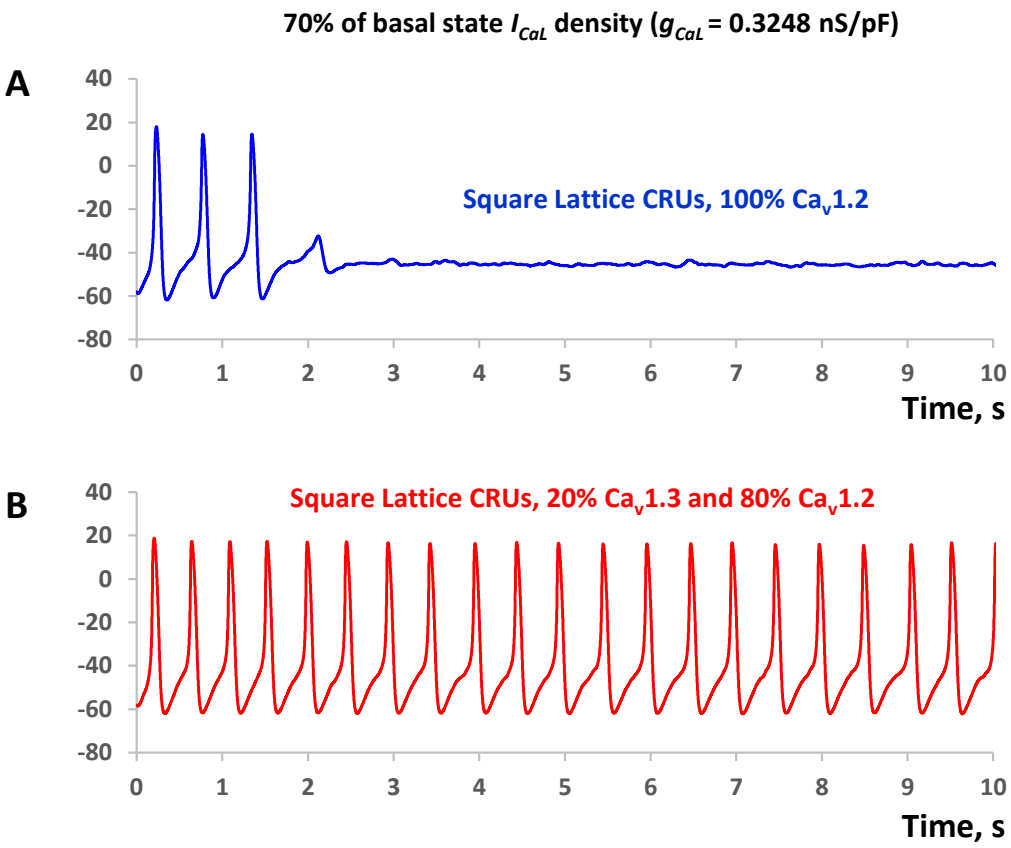
70% of basal state I_{CaL} density (g_{CaL} = 0.3248 nS/pF)
A
Square Lattice CRUs, 100% $Ca_v1.2$
40
20
0
-20
-40
-60
-80
0
1
2
3
4
5
6
7
8
9
10
Time, s
B
Square Lattice CRUs, 20% $Ca_v1.3$ and 80% $Ca_v1.2$
Time, s

Fig. A6

A

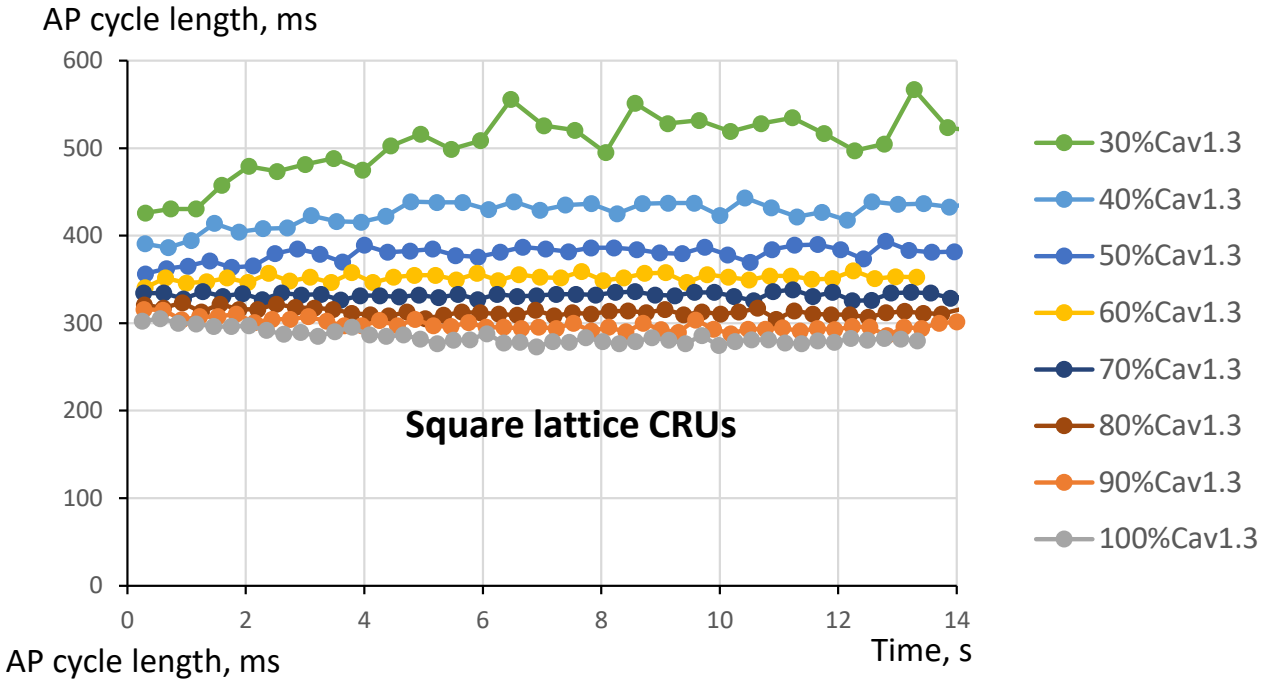
AP cycle length, ms
600
500
400
300
200
100
0
0
2
4
6
8
10
12
14
Time, s
Square lattice CRUs
30%Cav1.3
40%Cav1.3
50%Cav1.3
60%Cav1.3
70%Cav1.3
80%Cav1.3
90%Cav1.3
100%Cav1.3

B

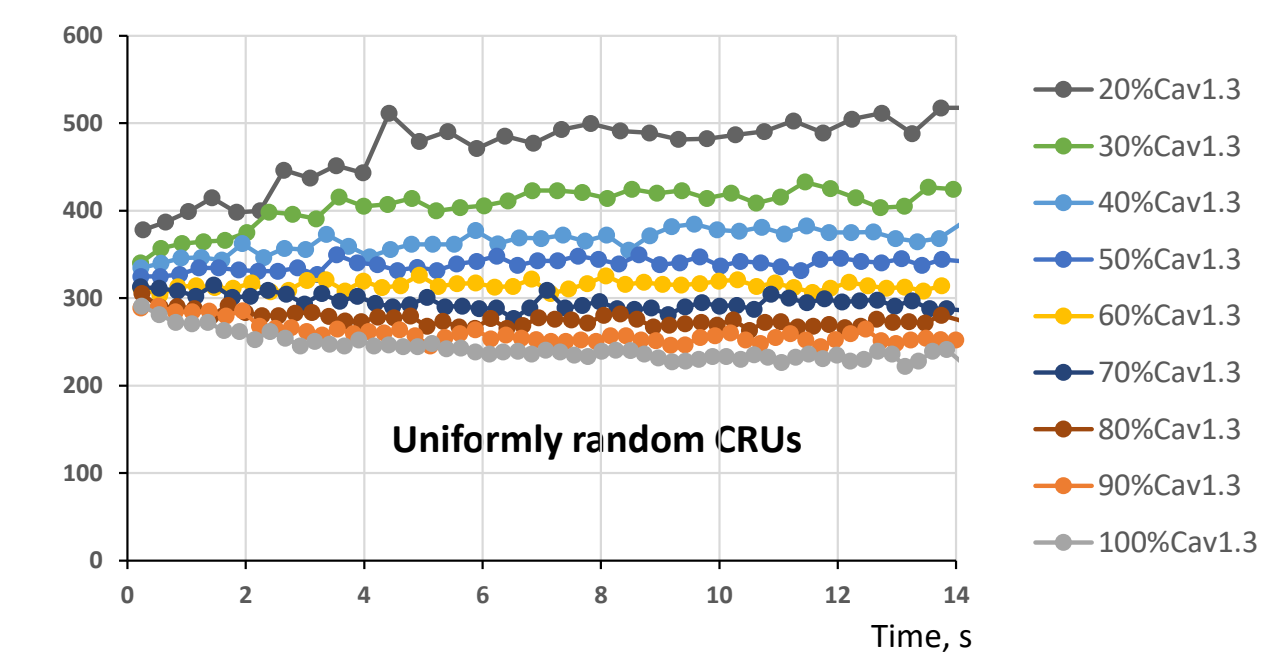
AP cycle length, ms
600
500
400
300
200
100
0
0
2
4
6
8
10
12
14
Time, s
Uniformly random CRUs
20%Cav1.3
30%Cav1.3
40%Cav1.3
50%Cav1.3
60%Cav1.3
70%Cav1.3
80%Cav1.3
90%Cav1.3
100%Cav1.3

C

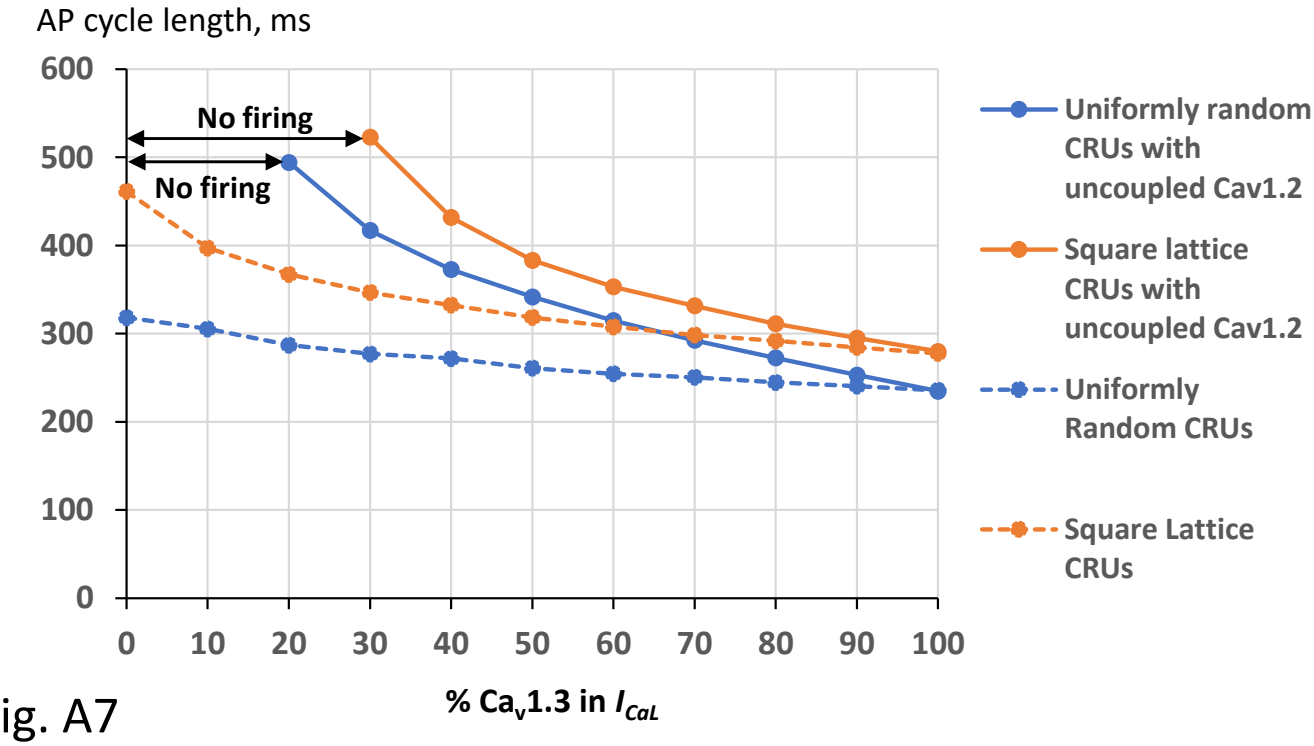
AP cycle length, ms
600
500
400
300
200
100
0
No firing
No firing
0
10
20
30
40
50
60
70
80
90
100
% Ca$_v$1.3 in I_{CaL}
Uniformly random CRUs with uncoupled Cav1.2
Square lattice CRUs with uncoupled Cav1.2
Uniformly Random CRUs
Square Lattice CRUs

Fig. A7

Movie legends:

Movie 1:

Square lattice distribution of CRUs. Simulation of Ca dynamics in submembrane space ($[Ca]_{sub}$) during 1s. Note mainly individual sparks in diastole. $[Ca]_{sub}$ is coded from 0.15 μM (black) to 10 μM (saturation) by a color scheme shown at the bottom of Fig. 6; open CRUs are shown by white dots. Closed CRUs in refractory period are shown by blue dots; closed reactivated CRUs (available to fire) are shown by green dots. JSR Ca level is coded by respective shade (white, blue or green) with a saturation level set at 0.3 mM. Simulation time and membrane potential (V_m) are shown in the top left corner.

Movie 2:

Perturbed square lattice distribution of CRUs with SD=0.25 μm. Sizes of LCRs increase during diastolic depolarization via propagating CICR. See Movie 1 legend for color description and other details.

Movie 3:

Perturbed square lattice distribution of CRUs with SD=0.5 μm. Sizes of LCRs further increase during diastolic depolarization via propagating CICR. See Movie 1 legend for color description and other details.

Movie 4:

Perturbed square lattice distribution of CRUs with SD=0.75 μm. Sizes of LCRs further increase during diastolic depolarization via propagating CICR. See Movie 1 legend for color description and other details.

Movie 5:

Uniformly random distribution of CRUs. Sizes of LCRs further increase during diastolic depolarization via propagating CICR. See Movie 1 legend for color description and other details.

Movie 6:

Stochastic individual sparks generated by a dormant cell model with square lattice distribution of CRUs. The dormancy was achieved by decreasing I_{CaL} conductance $\boldsymbol{g_{CaL}}$ to 0.2552 nS/pF. Simulation time and membrane potential (V_m) are shown in the top left corner. See Movie 1 legend for color description and other details.

Movie 7:

Subthreshold oscillatory LCR signals generated by a dormant cell model with uniformly random distribution of CRUs. The dormancy was achieved by decreasing I_{CaL} conductance $\boldsymbol{g_{CaL}}$ to 0.2552 nS/pF. Simulation time and membrane potential (V_m) are shown in the top left corner. See Movie 1 legend for color description and other details.